

Distribution Agreement

In presenting this thesis or dissertation as a partial fulfillment of the requirements for an advanced degree from Emory University, I hereby grant to Emory University and its agents the non-exclusive license to archive, make accessible, and display my thesis or dissertation in whole or in part in all forms of media, now or hereafter known, including display on the world wide web. I understand that I may select some access restrictions as part of the online submission of this thesis or dissertation. I retain all ownership rights to the copyright of the thesis or dissertation. I also retain the right to use in future works (such as articles or books) all or part of this thesis or dissertation.

Signature:

John S. Mancini

Date

Computational Studies on the Anharmonic Dynamics of Molecular Clusters

By
John S. Mancini
Doctor of Philosophy
Chemistry

Joel M. Bowman, Ph.D.
Advisor

Francesco Evangelista, Ph.D.
Committee Member

Michael C. Heaven, Ph.D.
Committee Member

James T. Kindt, Ph.D.
Committee Member

Accepted:

Lisa A. Tedesco, Ph.D.
Dean of the James T. Laney School of Graduate Studies

Date

Computational Studies on the Anharmonic Dynamics of Molecular Clusters

By

John S. Mancini

B.S., Richmond University, 2011

Advisor: Joel M. Bowman, Ph.D.

An abstract of A dissertation submitted to the Faculty of the James T. Laney
School of Graduate Studies of Emory University in partial fulfillment of the
requirements for the degree of
Doctor of Philosophy
in Chemistry
2015

Abstract

Computational Studies on the Anharmonic Dynamics of Molecular Clusters by John S. Mancini

Molecular nanoclusters present ideal systems to probe the physical forces and dynamics that drive the behavior of larger bulk systems. At the nanocluster limit the first instances of several phenomena can be observed including the breaking of hydrogen and molecular bonds. Advancements in experimental and theoretical techniques have made it possible to explore these phenomena in great detail. The most fruitful of these studies have involved the use of both experimental and theoretical techniques to leverage the strengths of the two approaches.

This dissertation seeks to explore several important phenomena of molecular clusters using new and existing theoretical methodologies. Three specific systems are considered, hydrogen chloride clusters, mixed water and hydrogen chloride clusters and the first cluster where hydrogen chloride autoionization occurs. The focus of these studies remain as close as possible to experimentally observable phenomena with the intention of validating, simulating and expanding on experimental work. Specifically, the properties of interest are those related to the vibrational ground and excited state dynamics of these systems. Studies are performed using full and reduced dimensional potential energy surface alongside advanced quantum mechanical methods including diffusion Monte Carlo, vibrational configuration interaction theory and quasi-classical molecular dynamics.

The insight gained from these studies are great and varied. A new on-the-fly *ab initio* method for studying molecular clusters is validated for $(\text{HCl})_{1-6}$. A landmark study of the dissociation energy and predissociation mechanism of $(\text{HCl})_3$ is reported. The ground states of mixed $(\text{HCl})_n(\text{H}_2\text{O})_m$ are found to be highly delocalized across multiple stationary point configurations. Furthermore, it is identified that the consideration of this delocalization is required in vibrational excited state calculations to achieve agreement with experimental measurements. Finally, the theoretical infrared spectra for the first case of HCl ionization in $(\text{H}_2\text{O})_m$ is reported, $\text{H}^+(\text{H}_2\text{O})_3\text{Cl}^-$. The calculation indicates that the ionized cluster's spectra is much more complex than any previous harmonic predictions, with a large number of the system's infrared active peaks resulting from overtones of lower frequency molecular motions.

Computational Studies on the Anharmonic Dynamics of Molecular Clusters

By

John S. Mancini

B.S., Richmond University, 2011

Advisor: Joel M. Bowman, Ph.D.

A dissertation submitted to the Faculty of the James T. Laney School of Graduate
Studies of Emory University in partial fulfillment of the requirements for the degree

of

Doctor of Philosophy

in Chemistry

2015

Acknowledgements

I am truly thankful to following people for their various contributions to the completion of this work.

- Dr. Joel M. Bowman for the opportunity to grow in every way possible. If not for him this work would not exist.
- Dr. Carol A. Parish at the University of Richmond for preparing me to do the work performed in this dissertation.
- Dr. Francesco Evangelista, Dr. Michael C. Heaven and Dr. James T. Kindt for their time, advice and patient support.
- Dr. Yimin Wang, Dr. Riccardo Conte, Hanchao Liu, Xiaohong Wang, Chen Qu, Dr. Gabor Czako, Dr. Antonio Gustavo Sampaio de Oliveira Filho, Dr. Eugene Kamarchik, Dr. Bastiaan Braams, Dr. Stuart Carter, Susan Browne, Dr. Volodymyr Babin, Dr. Hanna Reisler and Dr. Amit Samanta for their technical and practical insights.
- V. Upadhya, P. Muthu, E. Magnotti, B. Hays, A. Agarwala, Jason and again R. Conte for keeping me moving throughout my day-to-day work in Atlanta.
- My sister, C. Mancini; father, J. T. Mancini; and mother, F. DiSisto for their constant guidance and love.

Contents

1	INTRODUCTION	1
1.1	Molecular Insight	1
1.2	Enhanced Understanding with Theory	2
1.3	Structure of Dissertation	3
2	COMPUTATIONAL AND THEORETICAL METHODS	4
2.1	Overview	4
2.2	Potential Energy Surfaces	5
2.2.1	Introduction	5
2.2.2	Full-Dimensional Fitting	8
2.2.3	Many-Body Approximation	11
2.2.4	Procedure for Generating New Potential Energy Surfaces	13
2.2.5	Reduced-Dimensional Fitting	15
2.3	Vibrational Spectroscopy	17
2.3.1	Introduction	17
2.3.2	Discrete Variable Representation	18
2.3.3	Multimode	19
2.3.4	Diffusion Monte Carlo	22

CONTENTS

2.4	Quasi-Classical Simulation	25
3	(HCl)_n CLUSTERS	29
3.1	Overview	29
3.2	On-the-fly Ab Initio Calculations of Anharmonic Vibrational Frequencies: Local-Monomer Theory and Application to HCl Clusters	30
3.2.1	Context	30
3.2.2	Methods for Performing On-the-Fly Vibrational Calculations	35
3.2.3	On-the-Fly (HCl) ₁₋₆ Vibrational Frequencies	38
3.2.4	Summary and Conclusions	49
3.3	A New Many-Body Potential Energy Surface for HCl Clusters and Its Application to Anharmonic Spectroscopy and Vibration-Vibration Energy Transfer in the HCl Trimer	50
3.3.1	Context	50
3.3.2	(HCl) _n Many-Body Potential Energy Surface	51
3.3.3	Calculations of the HCl Trimer	55
3.3.4	Calculations of Larger HCl Clusters	65
3.3.5	Summary and Conclusions	68
3.4	Experiment and Theory Elucidate the Multichannel Predissociation Dynamics of the HCl Trimer: Breaking Up Is Hard To Do	69
3.4.1	Context	69
3.4.2	Theoretical Methods for the Study of (HCl) ₃ Predissociation	70
3.4.3	Ground State Properties and Dissociation Energies of (HCl) ₂₋₃	74
3.4.4	Rotational and Translation Distributions of (HCl) ₃ Fragments	76
3.4.5	Dissociation Mechanism of (HCl) ₃	79
3.4.6	Summary and Conclusions	80
4	MIXED (HCl)_n AND (H₂O)_m CLUSTERS	82

CONTENTS

4.1	Overview	82
4.2	A New Ab Initio Potential Energy Surface for HCl-H ₂ O, Diffusion Monte Carlo Calculations of D_0 and a Delocalized Zero-point Wavefunction	83
4.2.1	Context	83
4.2.2	Theoretical Methods for the Study the (HCl)(H ₂ O)	86
4.2.3	Ground State Properties of the (HCl)(H ₂ O)	90
4.2.4	Summary and Conclusions	93
4.3	Effects of Zero-Point Delocalization on the Vibrational Frequencies of Mixed HCl and Water Clusters	93
4.3.1	Context	93
4.3.2	Many-Body Potential for (HCl) _n (H ₂ O) _m Clusters	95
4.3.3	Theoretical Methods for the Study the (HCl) _n (H ₂ O) _m	98
4.3.4	Vibrational Ground State Properties of (HCl) _n (H ₂ O) _m	102
4.3.5	Vibrational Excited State Properties of (HCl) _n (H ₂ O) _m	106
4.3.6	Summary and Conclusions	113
5	H₃O⁺(H₂O)₃ Cl⁻ SOLVENT ION PAIR CLUSTER	115
5.1	Overview	115
5.2	Isolating the Spectral Signature of H ₃ O ⁺ in the Smallest Droplet of Dissociated HCl Acid	116
5.2.1	Context	116
5.2.2	Theoretical Methods for the Study of H ₃ O ⁺ (H ₂ O) ₃ Cl ⁻	118
5.2.3	IR Spectrum of H ₃ O ⁺ (H ₂ O) ₃ Cl ⁻	124
5.2.4	Summary and Conclusions	131
	REFERENCES	141

Listing of Figures

3.1	Global minimum geometries of HCl clusters.	34
3.2	Anharmonic stick spectra and relative intensities of the HCl trimer, tetramer, pentamer and hexamer from the current work (a), helium nanodroplets ⁷⁰ (b) and ragout-jet FTIR ⁷⁶ (c). Additional peak positions of note are trimer: 2810 cm^{-1} and tetramer: $2774\text{--}2778\text{ cm}^{-1}$. ⁵⁹ Dimer peak positions from jet-cooled infrared spectroscopy: 2880 cm^{-1} and 2857 cm^{-1} . ⁶⁰	48
3.3	Root-mean-square (RMS) of the three-body potential fitting error as a function of the trimer's three-body energy.	54
3.4	Potential energy surface cuts of the two-, three- and many-body (total) potentials of the trimer. The configuration of the minima in each cut is the ring conformation. Cuts were taken (left) as a function of the monomer–dimer center-of-mass distance along a path which leads to dissociation into a dimer and a monomer and (right) as a function of the Cl–Cl distance as the monomers are uniformly compressed and then separated.	57

LISTING OF FIGURES

3.5	Vibration-vibration energy transfer of the local H-Cl stretch in the HCl trimer, computed using the Hückel-model and classical trajectories. The unexcited stretch refers to either of the two unexcited monomer stretches, as their behavior is identical in both models. Additional details provided in the text.	63
3.6	Vibration-vibration energy transfer of the local H-Cl stretch in the HCl trimer, computed using quasi-classical trajectories. Additional details provided in the text.	65
3.7	Transition state (top) and global minimum (bottom) of the HCl tetramer.	66
3.8	Diffusion Monte Carlo simulation of the HCl dimer (blue) and trimer (red) as a function of imaginary time step.	72
3.9	Isosurface representations of the HCl dimer (left) and trimer (right) ground state wavefunctions.	74
3.10	Comparison of theoretical and available experimental HCl monomer rotational populations.	77
3.11	Comparison of c.m. E_T distributions obtained by detecting HCl fragment (red curve) in $J''=5, 8$ and 10 . Black curves are the corresponding distributions obtained from QCT calculation for Channel I.	77
3.12	Internal energy distribution of dissociated dimer relative to its anharmonic ZPE (black). The inset (red) contains a plot of the percentages of monomers which can possibly dissociate from the dimer with a given J'' , assuming that one monomer dissociates with $J'' = 0$ and zero translational energy.	78
3.13	HCl monomer translational distribution for $J'' = 5$ with the monomer dissociating from an internally “hot” dimer (red) and vibrationally excited trimer via the monomer + dimer channel (green).	79

LISTING OF FIGURES

3.14	Minimum energy path from trimer to open-chain configuration. . . .	80
4.1	Geometry of the global minimum with labeled coordinates.	85
4.2	Energy as a function of the number of points and the respective RMS fitting error for a portion of the fitting data.	87
4.3	Minimum energy potential along the dissociation coordinate of the dimer computed using the new dimer potential energy surface. . . .	88
4.4	Visualization of the HCl-H ₂ O dimer DMC ground state wavefunction from two perspectives.	91
4.5	Relaxed 1-D potential cut along the imaginary frequency mass-scaled normal mode of the transition state. The solution to the 1-D Schrödinger equation for the ZPE and the square of the wavefunction are shown in red.	92
4.6	Root-mean-square (RMS) of the three-body potential fitting errors as a function of the trimers' three-body energies.	97
4.7	Potential energy cuts of three-body and two-body potentials in the (HCl) ₂ (H ₂ O) [HHW] and (HCl)-(H ₂ O) ₂ [HWW].	98
4.8	Planar configurations of indicated HCl and H ₂ O clusters.	102
4.9	An isosurface representations of the vibrational ground state wavefunctions of the indicated mixed HCl and H ₂ O clusters computed using diffusion Monte Carlo simulations. The wavefunction representations are shown relative to the planar configurations.	104
4.10	Isosurface representations of the vibrational ground state wavefunctions of the indicated mixed HCl and H ₂ O clusters computed using diffusion Monte Carlo simulations. The wavefunction representations are shown relative to the planar configurations.	105

LISTING OF FIGURES

4.11	The HWW Q_{im} two-dimensional potential energy surface (left) and ground state normalized wavefunction squared (right). The surface's zero-point energy is 319 cm^{-1}	108
4.12	Plot of anharmonic vibrational frequencies for the HCl stretch in the $(\text{HCl})_n(\text{H}_2\text{O})_m$ clusters. The monomer labeling used in the text is applied here for cases where multiple HCl monomers are present. The vibrational frequencies were computed at the global minimum configurations (Minimum) and the DMC predicted stationary point configurations (Planar), and using the DLOC calculations. Available experimental values are plotted for comparison. ^{109,153,40,41}	111
4.13	Plot of anharmonic vibrational frequencies for the OH stretch in the $(\text{HCl})_n(\text{H}_2\text{O})_m$ clusters that have reported experimentally in Reference ¹⁴⁵ . The monomer labeling used in in the text is applied here for cases where multiple H_2O monomers are present. The vibrational frequencies were computed at the global minimum configurations (Minimum) and the DMC most probably configurations (Planar), and using the DLOC calculations.	112
5.1	Global minimum SIP configuration from two perspectives and its embedded H_3O^+ harmonic and coupled anharmonic spectrum. Each stick represents an individual state with the band shapes produced from the convolution of a Gaussians. The intensities of the two spectra are unscaled.	118

LISTING OF FIGURES

- 5.2 Representations of the 12 LMon eigenvectors for the H_3O^+ embedded in the SIP cluster. The first six modes refer to intermolecular motions and the last six intramolecular motions. The abbreviations used are Frus. = Frustrated, Trans. = Translation, Rot. = Rotation, Sym = Symmetric, Asym = Asymmetric, Str. = Stretch. The labels, X, Y, Z are used to refer to the relative axis of the mode, where the Z-axis passes through the Cl^- and the O of the H_3O^+ 119
- 5.3 Higher energy local minima of the SIP and unionized $\text{HCl}(\text{H}_2\text{O})_4$ cluster: (A), non-symmetric higher energy SIP cluster; (B), five-membered ring configuration; (C), four-member ring with water monomer accepting and donating a hydrogen bond to the ring; and (D) four-member ring with water monomer accepting a hydrogen bond from the ring. . 129

List of Tables

3.1	Harmonic and anharmonic frequency (cm^{-1}) of HCl monomer using different electronic structure methods.	39
3.2	Harmonic frequencies (cm^{-1}) of the HCl dimer from indicated calculations see text for details.	39
3.3	Anharmonic frequencies (cm^{-1}) of the HCl dimer from calculations using the LMon-Hückel approaches as described in the text and comparisons with benchmark six-dimensional results.	40
3.4	Harmonic frequencies (cm^{-1}) of the HCl trimer from indicated calculations, see text for details.	41
3.5	Anharmonic frequencies (cm^{-1}) of the HCl trimer from calculations using the LMon-Hückel method as described in the text.	42
3.6	Harmonic frequencies (cm^{-1}) of the HCl tetramer from indicated calculations, see text for details.	44
3.7	Anharmonic frequencies (cm^{-1}) of the HCl tetramer from calculations using the LMon-Hückel method as described in the text.	44
3.8	Harmonic and anharmonic vibrational frequencies (cm^{-1}) of the HCl pentamer.	45

LIST OF TABLES

3.9	Harmonic and anharmonic vibrational frequencies (cm^{-1}) of the HCl hexamer.	45
3.10	Energies (cm^{-1}) of three low-lying stationary points of the HCl trimer and D_e values.	56
3.11	Harmonic frequencies (cm^{-1}) for HCl clusters using the many-body potential surface and <i>ab initio</i> calculations at the respective methods minima. The labels ring, Z and Y refer to the three different conformations of the trimer.	57
3.12	Vibrational frequencies (cm^{-1}) of the HCl trimer from indicated calculations and experiment, see text for details.	59
3.13	Harmonic frequencies for $(\text{HCl})_{4-6}$ clusters using the many-body potential surface at the global minima and $(\text{HCl})_4$ low lying transition state conformations.	67
3.14	HCl trimer and dimer D_e values (cm^{-1}).	75
3.15	HCl trimer and dimer D_0 values (cm^{-1}).	76
4.1	Geometry (\AA and degrees) of indicated configuration from <i>ab initio</i> calculations and the potential energy surface for the global minimum, transition state and dissociated monomers.	87
4.2	Harmonic Frequencies (cm^{-1}) for HCl- H_2O from <i>ab initio</i> calculations and the PES for the global minimum, transition state and dissociated monomers.	88
4.3	Double-well barrier (DWB) and electronic dissociation D_e (cm^{-1}) from <i>ab initio</i> calculations (see text for details) and the PES.	90
4.4	Harmonic, anharmonic and experimental vibrational frequencies (cm^{-1}) for $\text{HCl}(\text{H}_2\text{O})_2$. †=109 ‡=145 *=Tentative Assignment	107
4.5	Harmonic and anharmonic vibrational frequencies for HW. †=109 ‡=145 *=41	110

LIST OF TABLES

4.6	Harmonic and anharmonic vibrational frequencies for HHW. ^{†=109 ‡=145} *=41	110
4.7	Harmonic and anharmonic vibrational frequencies for HHWW. ^{‡=145} *=41	110
4.8	Harmonic and anharmonic vibrational frequencies for HHHW. ^{†=153} *=41	110
4.9	Harmonic and anharmonic vibrational frequencies for HWWW. ^{†=109} *=41	111
5.1	Summary of the SIP H ₃ O ⁺ harmonic stretch frequencies (cm ⁻¹). . . .	118
5.2	Details of the SIP many-body interactions from CCSD(T)-F12/aVDZ.	121
5.3	Details of the components of the PES surface's total number of points, fitting root-mean-squared-deviation (RMSD) and energy span.	121
5.4	Details of the components of the DMS surface's total number of points and fitting root-mean-squared-deviation (RMSD).	122
5.5	Harmonic frequencies (cm ⁻¹) and normalized double harmonic inten- sities of the embedded H ₃ O ⁺ in the SIP configuration computed using the different approaches.	124
5.6	Properties of the embedded H ₃ O ⁺ in the SIP configuration. Distances are reported in Ångstroms and angles in degrees.	124

LIST OF TABLES

5.7	Results of weighted virtual state analysis for the twelve-mode H_3O^+ in the SIP configuration four-mode coupled spectra. Each band is labeled along with the number of IR active VCI states in the band. All states whose weighted coefficients are within 50% of the largest state's coefficient are shown for each respective bands. The percent of the largest virtual VSCF state are given, followed by the respective state. The twelve integers listed in each virtual VSCF state are the excitations from the ground state where each sequential number refers to respective harmonic mode.	127
5.8	Quantum deconstruction of the IR spectrum of the SIP embedded H_3O^+ . The sections <i>Reduced</i> and <i>Complete</i> refer to the results of the reduced-dimensional six-highest-frequency-mode coupled calculation and the full twelve-mode coupled calculation, respectively. The frequencies are reported in cm^{-1} and the intensities in normalized units. The column “# of States” indicates the number of VCI states in the band range	128
5.9	CCSD(T)-F12/aVDZ local harmonic frequencies (cm^{-1}) for the SIP cluster in the alternate non-symmetric conformation.	130

Citations to Previously Published Work

The Chapters 3-5 of dissertation has been adapted from previously published papers.

Chapter 3 is comprised of work from three publications:

1. **John S. Mancini** and Joel M. Bowman, *On-the-fly ab initio calculations of anharmonic vibrational frequencies: Local-monomer theory and application to HCl clusters*, J. Chem. Phys., 139, 164115, (2013), [link].
2. **John S. Mancini** and Joel M. Bowman, *A new many-body potential energy surface for HCl clusters and its application to anharmonic spectroscopy and vibration-vibration energy transfer in the HCl trimer*, J. Phys. Chem. A, 118, 7367, (2013), [link].
3. **John S. Mancini**, Amit K. Samanta, Joel M. Bowman and Hanna Reisler, *Experiment and theory elucidate the multichannel predissociation dynamics of the HCl trimer: Breaking up is hard to do*, J. Phys. Chem. A, 118, 8402, (2014), [link].

Chapter 4 contains research from two publications:

1. **John S. Mancini** and Joel M. Bowman, *Communication: A new ab initio potential energy surface for HCl-H₂O, diffusion Monte Carlo calculations of*

LIST OF TABLES

D_0 and a delocalized zero-point wavefunction, J. Chem. Phys., 138, 121102, (2013), [link].

2. **John S. Mancini** and Joel M. Bowman, *Effects of zero-point delocalization on the vibrational frequencies of mixed HCl and water clusters*, J. Phys. Chem. Lett., 5, 2247, (2014), [link].

Chapter 5 consists of a study from one publication:

1. **John S. Mancini**, Joel M. Bowman, *Communication: Isolating the spectral signature of H_3O^+ in the smallest droplet of dissociated HCl acid*, Phys. Chem. Chem. Phys., (2014).[link].

1

Introduction

1.1 MOLECULAR INSIGHT

All systems in existence are commanded by the same molecular level interactions. These forces impact everything from how water droplets form at the edge of a leaf, to how Chloride reacts to forms holes in the ozone layer above Earth. Despite these interactions dictating the behavior of everything, there remain countless mysteries surrounding them. Many of these question center on small groups of homogenous and heterogenous molecules. Difficult questions like, how do these systems grow and how do they fall apart, remain inquires of fundamental interest. The answers to these question and the steps taken to obtain them, have the potential to impact how

future humans behave with the world. It is the later line of thinking that provides the primary motivation for the work performed in this dissertation.

1.2 ENHANCED UNDERSTANDING WITH THEORY

Experimental spectroscopy, in the field of physical chemistry, strives every year to study more complex systems with greater levels of detail. However, even with the development of new techniques it continues to be necessary that theoretical investigations be performed alongside experiment. The goal of theoretical studies in this case are to validate observations and obtain answers to questions that experiment cannot yet consider. This interplay between theory and experiment has been paramount in understanding the behavior of small molecular systems which contain less than 100 atoms. Perhaps the most prominent examples of small molecular system with high interest are nanoclusters. Nanoclusters are a collection of one or more interacting molecular species. Their study provides a fundamentally important understanding of the forces and dynamics that form and dictate the behavior of larger molecular systems.

This dissertation is focused on recent theoretical studies of molecular nanoclusters which I have performed with the twofold goal of complementing recent experimental observations and presenting new questions for experimental consideration. The spirit of this work can be summarized as the construction and application of new and existing mathematical models based on first principles to describe molecular clusters. These studies delivered a wide array information about the dynamic properties of molecular systems and succeeded in validating, contesting and expanding on various experimental observations.

1.3 STRUCTURE OF DISSERTATION

This dissertation is organized into four separate chapters. Chapter 2, introduces the theoretical background for the work that was performed. This focuses primarily on a series of techniques developed by others, which were utilized and expanded upon over the course of this work. The chapter includes several subsections which briefly review potential energy surfaces, vibrational spectroscopy techniques and quasi-classical simulations. Chapters 3–5 present the application of Chapter 2’s theoretical approaches to study pure hydrogen chloride clusters, mixed hydrogen chloride and water clusters and the ionized form of mixed hydrogen chloride and water. In Chapter 3 the following are presented: an on-the-fly anharmonic frequency study of hydrogen chloride clusters, the development of a many-body hydrogen chloride potential energy surface, the vibrational relaxation behavior of the fundamental stretches in the hydrogen chloride trimer, and the vibrational predissociation dynamics of the hydrogen chloride trimer. Chapter 4 details the creation of a many-body potential surface for hydrogen chloride and water clusters prior to hydrogen chloride auto-ionization. The potential is applied to study the vibrational ground and excited state properties of these heterogeneous systems. Finally, Chapter 5 discusses the calculation of the infrared spectrum for the reported smallest cluster of auto-ionization hydrogen chloride in water using a new embedded potential energy surface.

2

Computational and Theoretical Methods

2.1 OVERVIEW

In the following I will discuss the theoretical and computation methods applied to obtain the results discussed in Chapters 3 - 5. This chapter is divided into sections named Potential Energy Surfaces, Vibrational Spectroscopy and Quasi-Classical Simulations. Each section is divided into subsections, which selectively explore the theoretical techniques applied in this dissertation work. The section Potential Energy Surfaces, discusses the functional representations of solutions to the electronic motion for a molecular system as function of its nuclear coordinates. The applications of these representations to study the nuclear motions are described in the following sections.

The section Vibrational Spectroscopy introduces the algorithms and programs used to study molecules' vibrational ground and excited states. The section Quasi-Classical Simulations details the method used to perform time-dependent molecular dynamic simulations with quantized initial conditions. The focus of this chapter is to provide a general introduction and functional understanding of the topics. All approaches detailed in this chapter have been reported in the literature previously and are cited accordingly.

2.2 POTENTIAL ENERGY SURFACES

2.2.1 INTRODUCTION

In studies of molecular systems, electrons can be approximated as re-orientating immediately with changes in the nuclear coordinates. This approximation, known as the Born-Oppenheimer approximation, allows for the Schrödinger equation to be separated and solvable in terms of the molecule's electronic and nuclear motions.^{1,2} The solutions to the electronic motion (electronic Schrödinger equation) at every possible nuclear configuration for a molecular system is referred to as a potential energy surface (PES). In practice, the PES operates as a map where a single set of molecular coordinates defines a single electronic energy. Once the PES is solved, nuclear properties of the system can be computed by solving the nuclear motions (nuclear Schrödinger equation), which are dependent on the electronic solutions. The concept of the PES is key for the study of the molecular systems presented in this dissertation and is integral for the application of the methods described in the following sections.

The PES can be computed by directly solving the electronic Schrödinger equation at every desired nuclear configuration. This approach is referred to as computing the PES on-the-fly. These calculations are most commonly used to identify important molecular configurations on the PES, such as minima or saddle points, and to

compute harmonic frequencies. More complex nuclear properties, such as dynamics and anharmonic spectroscopy can be studied using on-the-fly approaches as well, but often at a high computational cost. The large cost results from the sizable number of points on the PES that must be solved in order to calculate the dependent nuclear properties. When these properties are studied on-the-fly, lower level solutions to the electronic motion are traditionally used and/or approximations are made about the behavior of the nuclei which reduce the number of required calculations.

An alternate approach to on-the-fly calculations is to fit the system's PES to a functional form. Information about the PES is first obtained by solving the electronic Schrödinger equation at several different configurations, measuring properties with experiments or some combination of theoretical and experimental information. A mathematical form can then be used to represent the collected data. When the data are purely from theory, the resulting function is capable of evaluating the energy for a given set of molecular coordinates that are related to the initial fitting data, that is to say, a localized data set results in a localized potential. In a similar manner when a experimental or mixed data sets are used, the fitted function will re-report the energies required to compute the experimental values. The functional form of a PES, when properly constructed, can be applied to study the nuclear properties of the system just as though the solutions were obtained directly from solving the electronic motions at each point.

No single function has been identified that can characterize the PES of an arbitrary polyatomic system. Therefore, several different functional forms exist which can be used to fit a PES.^{3,4,5,6,7} In all cases, the functional form must have a sufficient number of fitting variables to properly describe the curvature of the PES, while not having too many so as to result in overfitting. Overfitting of PES can cause unphysical behavior in the function's output. Once fit to a proper functional form, the PES is traditionally much simpler to evaluate than the electronic Schrödinger

equation itself; this efficiency allows for a huge speed-up in the calculation time of molecular energies. This speed-up does, however, come at the cost of generating errors due to the differences between functional form and fitted data. The functional form must be considered as an approximation of the true PES, albeit a rather good one. Error in the fitting is propagated in the nuclear properties which are computed by the PES. Beyond the fitting errors, it is important to also mention that the quality of the PES function is only as good as the data, experimental or theoretical, with which it was fit. Higher quality fitting data results in a high quality representation of the potential surface. Similarly the conformational space with which the potential is applicable is dependent on the range of space covered by the fitting data. I mention before continuing forward that for the remainder of this dissertation, potential and the abbreviation PES may be used to refer to both the true energy landscape of the system as well as the fitted function, the respective meanings will be apparent from the context of the text.

In addition to there being a unique energy value at every molecular configuration there is also a unique three-dimensional dipole moment vector associated with each configuration.^{8,9} The dipole moment geometry relation forms a dipole-moment surface (DMS) for the system. The use of the DMS is key for the calculation of infrared intensities in vibrational calculations. Many of the tools applied to consider PES can be applied to DMS.

The work presented in this dissertation was conducted using both on-the-fly and fit PES. In the following subsections the techniques used to generate the fitted PES are described, while the on-the-fly calculations are discussed in Chapter 3. The functional form taken to generate the full dimensional PES are detailed in the subsection titled Full-Dimensional Fitting. The representation of the potential as a sum of monomer and higher-order interactions is described in the subsection called Many-Body Approximation. A series of guidelines followed to construct the PES are given in the

subsection Procedure for Generating New Potential Energy Surfaces. The final subsection, Reduced-Dimensional Fitting, describes the approaches taken to fit reduced dimensional PES. In addition to discussion of the PES, similar methodologies for fitting DMS are also discussed when appropriate.

2.2.2 FULL-DIMENSIONAL FITTING

In the following I selectively introduce the theory behind the fitting approach, which I applied to generate new molecular potential energy surface. First, the fitting approach known as the monomial symmetrization is introduced in order to provide a conceptual understanding of the fitting.³ Next the essentials of a numerically equivalent yet more computationally efficient approach based on invariant polynomial theory is given;³ This approach was used to generate the new PES functions discussed in the later chapters of this dissertation.

The potential energy, V , of a molecular surface can be defined uniquely based on the well defined internuclear distances r_{ij} of the system. Using these distances, the potential can be represented as a polynomial expansion. Consider the potential of a triatomic system as an example, the functional form can be written as:

$$V = \sum_{m=0}^M C_{abc} [y_{12}^a y_{13}^b y_{23}^c]; (m = a + b + c), \quad (2.1)$$

where M is the order of the total polynomial, y_{ij} is a Morse variable, the subscripts 1, 2 and 3 the indices for each atom and C_{abc} representative of the fitting coefficient for a set of a , b and c values. The Morse variable is given by $\exp(-r_{ij}/\lambda)$ where λ is a range parameter of the function. Based off my and others experience this value is fixed at 2.0 bohr. The use of the Morse basis functions help to ensure that at large atomic separations the potential has the proper asymptotic behavior. The C_{abc}

coefficients can be determined using linear least squares fitting approaches.

The above approach is sensible if all three atoms are unique, \mathbf{ABC} . If however, there are identical atoms in the system, $\mathbf{A}_2\mathbf{B}$, then the permutational symmetry of those atoms should be considered. One way to take into account the symmetry is to duplicate and mirror the points of identical atomic displacements. Clearly this is an impractical and unwieldy method when fitting the potentials of larger molecular systems. A more elegant approach is to explicitly consider the system's symmetry in the fitting function itself. This can be done most simply by symmetrizing the monomials so that the basis directly takes into account the identical atoms. In this approach a symmetry operator, S , is applied to the polynomial function:

$$V = \sum_{m=0}^M D_{abc} S[y_{12}^a y_{13}^b y_{23}^c]; (m = a + b + c). \quad (2.2)$$

In the case of a triatomic system with two identical atoms the symmetry operator yields:

$$V = \sum_{m=0}^M D_{abc} [y_{12}^a y_{13}^b y_{23}^c + y_{12}^a y_{23}^b y_{13}^c]; (m = a + b + c), \quad (2.3)$$

where the permutations of the two like atoms are now explicitly considered. This technique can be applied for an effectively arbitrary system where there are multiple different types of identical atoms. The number of equivalent monomials in the fitting function is given by the number of possible atom permutations $i!j!...k!$ for any $\mathbf{A}_i\mathbf{B}_j...X_k$ system. This approach is known as monomial symmetrization.

There exists a numerically equivalent approach to monomial symmetrization that is based on invariant polynomial theory. This approach, which I used to generate new potentials discussed in the later chapters, provides a more compact representation of the PES and therefore, in most cases, presents a more computationally efficient

function to evaluate. Essentially, the functional PES can be written as:

$$V = \sum_{\alpha=0}^M h_{\alpha}(\mathbf{p}(\mathbf{y}))q_{\alpha}(\mathbf{y}), \quad (2.4)$$

where $\mathbf{p}(\mathbf{y})$ is the vector formed by the primary invariant polynomials, and $q_{\alpha}(\mathbf{y})$ (for $1 \leq \alpha \leq M$) are the secondary invariant polynomials. In the case of a triatomic molecule with two identical atoms, the single primary invariant associated with the \mathbf{AA} are y_{12} and the two associated with the \mathbf{AB} is $(y_{13} + y_{23})/2$ and $(y_{13}^2 + y_{23}^2)/2$. The single secondary invariant is equal simply to 1. The total number of primary invariant polynomials for a system with N atoms is given by the number of internuclear distances, $N(N - 1)/2$. The secondary invariant polynomials are determined from the computational algebra software MAGMA. In practice, the permutational invariant fitting approach can be applied to systems of arbitrary size and symmetry. Efficient implementation of this approach was made possible for the PES functions generated in the course of this dissertation work using a series of robust routines described in reference [3].

Considering next the fitting of the DMS. The DMS differs from the PES because the dipole monomer is a vector quantity. Three separate fits, using the approach described above, for the three components could be performed to generate three separate dipole moment surfaces. Instead, however, a single functional form is used that expresses the dipole as:

$$\vec{\mu} = \sum_i w_i(X)\vec{x}(i), \quad (2.5)$$

where X refers to the molecular configuration, $\vec{x}(i)$ the position vector of the i th nucleus and $w_i(X)$ the effective charge on the i th nucleus that depends on X and can be represented in terms of internuclear distances.

2.2.3 MANY-BODY APPROXIMATION

The key to generating a high quality potential energy surface is the construction of a fitting data set consisting of accurate potential energy values computed over the range of configurations for which there are properties of interest. When considering larger molecular systems containing more than 10 atoms these ideals are difficult to satisfy. The computational time required to solve the electronic structure problem for molecular systems scales exponentially with the number of atoms. Furthermore, every additional atom adds three degrees of freedom to the problem, increasing the number of configurations required to properly study the system's conformational space. Fortuitously, in the study of molecular clusters these challenges can be overcome by partitioning the system into a set of non-interacting monomers and a truncated series of interacting subsystems. This approach relies on representing the potential in terms of a truncated many-body expansion.¹⁰

The many-body representation of the total energy V_{total} for an arbitrary sized molecular cluster of N monomers is given by:

$$V_{\text{total}} = \sum_i V_i + \sum_{ij} \Delta^2 V_{ij} + \sum_{ijk} \Delta^3 V_{ijk} + \dots + \Delta^N V, \quad (2.6)$$

where V_i is the energy of the i^{th} monomer, $\Delta^2 V_{ij}$ is the two-body interaction energy between two monomer i and j excluding the monomer energies, $\Delta^3 V_{ijk}$ is the three-body interaction energy between monomers i , j and k excluding the monomer and two-body energies and $\Delta^N V$ the highest-order interaction between all N monomers excluding all lower level interactions. All interactions are summed over every unique combination of monomers. Explicitly, the two-body and three-body interactions are

$$\Delta^2 V_{ij} = V_{ij} - (V_i + V_j), \quad (2.7)$$

and:

$$\Delta^3 V_{ijk} = V_{ijk} - (V_i + V_j + V_k) - (\Delta^2 V_{ij} + \Delta^2 V_{ik} + \Delta^2 V_{ij}), \quad (2.8)$$

where the terms V_{ij} and V_{ijk} in the equations are the total energies of the dimers and trimers, respectively. Each of the respective interaction energies are intrinsic interactions, meaning that the interaction energies are zero at infinite monomer separation. In the case of a N monomer cluster the potential is defined exactly in terms of N separate orders of interaction. However, the contributions to the total energy of the system are dominated by the two- and three-body interactions in most molecular clusters, specifically the ones studied in this dissertation. The two-body interactions are generally observed as the largest total percentage of interaction energy.

One benefit of truncating the many-body expansion is that individual potentials can be fit for only the one-, two- and three-body interactions and still provide an accurate representation of the true PES for an arbitrarily large molecular cluster. Furthermore, this representation allows for a stepwise construction of cluster potentials that can be grown to describe progressively more complex systems. New interactions can be combined with existing potentials to allow for the study of larger heterogenous systems. The many-body interactions can also be constructed with a hybrid representation of the total energy, that is to say, each interaction can be built from a different method. In this way the hybrid approach allows two-body potentials to be built from more accurate energies than the three-body potentials. Consideration of the same level of theory for both two- and three-body interactions may not be possible due to the larger size of trimers. The effective errors in using lower level methods for the three-body interaction are relatively low due to the traditionally smaller contribution of three-body interaction to the total energy relative to the two-body.

The dipole-moment surface can also be represented using the many-body expansion. In most cases the many-body problem converges faster for the dipole-moment and

so only a one- and two-body dipole moment surface are necessary to describe larger systems.¹¹ This is the approach taken when constructing DMS in this dissertation.

2.2.4 PROCEDURE FOR GENERATING NEW POTENTIAL ENERGY SURFACES

The procedure to construct a new functional potential energy surface using the invariant polynomial fitting approach can vary depending on the system and the nuclear properties which the PES is intended to study. Despite this variation, I have identified what I believe to be a series of best practices for the generation of new potentials, specially those intended for use in the many-body representation of clusters. These observations are based on my personal experience generating several many-body interaction potentials. In the following I discuss the physical steps taken to generate new potentials and observations about the construction process.

Consider a molecular cluster for which the desired nuclear properties for study are the vibrational spectroscopy and dynamics. A new many-body potential for this cluster can be constructed in a stepwise fashion starting from the monomer, then the two-body and then the three-body potentials. Several monomer potentials are available from previous high quality experimental studies and high level *ab initio* calculations; they should first be considered for use before a new potential is built. If no previous potentials are available or those that are available need to be improved upon, then the construction of a new potential begins by identifying the minima and harmonic frequencies of the system. These should be done at several different levels of theory in order to determine the appropriate method to describe the system that balances the need for speed and accuracy in the single point energy calculations. An initial series of points for the system are generated from the displacements required to numerically compute the harmonic frequencies, cuts along normal coordinates and direct dynamics calculations. Direct dynamics calculations refer to *ab initio* molecu-

lar dynamic simulations where Newton's equations of motion are used to propagate the molecular system in time with the potential and gradient computed on-the-fly using computationally efficient methods such as Density Functional Theory. Once an initial data set is obtained the points are evaluated using the appropriate electronic structure method and fit to the permutationally invariant function. Ideally the smallest order of the polynomial is chosen to minimize the number of fitting coefficients and therefore minimize the evaluation time of the function. The newly fit potential is tested for its best case fitting error by computing the root-mean-square deviation (RMSD) of the fitting data set. In addition, the RMSD is computed for a separate set of points which have been excluded from the fitting data. Relative energetic orderings of the minima are tested as well as nuclear properties such as the harmonic frequencies. Nuclear calculations which are described in the following subchapter are performed to identify areas of the potential which are not properly described by the fitted function. Based on the results of these tests, additional points are added to the data set and the PES re-fit. This process occurs iteratively until satisfactory small RMSD values are computed, good agreement is observed relative to ab initio measured nuclear quantities and sensible results given by more complex nuclear calculations. When generating data sets for the two-body interactions, points for the fitting data set should be taken from sub-clusters of larger cluster minima. An example of sub-clusters could be the dimer configurations of the system's trimer or tetramers. This ensures the two-body potential is optimized for a many-body representation of the cluster, not applications to the isolated dimer. The same considerations should be made for the three-body interactions. In the later case, part of the fitting datasets can be obtained from points associated with important configurations identified using the one- and two-body PES.

Ideally all many-body interactions should be constructed from Coupled Cluster with singles, doubles and perturbative triples where the basis set is a complete basis

set extrapolation. A database of these calculations, while possible for some system, are too expensive for most. Due to its relative cost and accuracy I instead consider the “gold standard” (based on the systems studied over the course of this dissertation work) to be CCSD(T)-F12/aVTZ where F12 refers to the inclusion of explicit correlation.¹² Explicit correlation serves to effectively increase the quality of Dunning correlation-consistent basis sets by one cardinal, that is to say -F12/aVDZ \approx aVTZ and -F12/aVTZ \approx aVQZ.¹³ This level of theory should be applied for the formulation of one- and two-body potentials. A CCSD(T)-F12/aVTZ three-body potential however would be too computationally expensive to construct, so instead either CCSD(T)-F12/aVDZ or second order Moller Plesset (MP2) with explicit correlation and aVDZ basis can be used. In comparisons performed over the course of this work the two approaches gave similar magnitudes of error relative to CCSD(T)-F12/aVTZ calculations.

I mention again that these observations serve only as a guide for future work based on the work performed in this dissertation. Each new potential will require testing to determine the appropriate methodology. Furthermore as new electronic structure methods are developed and more powerful computers become available the guidelines are likely to become outdated.

2.2.5 REDUCED-DIMENSIONAL FITTING

Over the course of this work there were circumstance where it was useful to consider a full dimensional systems in terms of one or two import normal mode coordinates or linear combinations of normal mode coordinates. In these instances it was not appropriate to fit the system in terms of the intermolecular distances. Three approaches were applied to generate functional forms of these reduced dimensional systems. The

first was a simple linear least squares fit to a high order polynomial:

$$V = \sum_{i=0}^n a_i x^i \quad (2.9)$$

where a_i were to coefficients and n the order of the polynomial. This worked well for fitting the bottom region of simple Morse-like potentials in one dimension. The second approach represents the potential using cubic spline interpolation¹⁴

$$V_l(Q) = \sum_{i=0}^3 a_i(Q)^i; Q_l < Q < Q_{l+1}, \quad (2.10)$$

where V_j is one of n local representations of the potential and a_i are fitting coefficients. In total there are $4n$ coefficients required to define the full $V(Q)$ potential. The coefficients are determined using the requirement that the local function match the polynomial at both end of the intervals, that the first and second derivatives are continuous and that the first derivative at the end intervals are equal to specified value. This interpolation was used to represent double well potentials, which were too difficult to represent with the simple polynomial in x . The Numerical Recipes implementation of this procedure was used.¹⁴ The third reduced fitting approach was a bivariate local technique which used a segmented fifth-degree polynomial in Q_1 and Q_2

$$V_{lkm}(Q_1, Q_2) = \sum_{j=0}^5 \sum_{i=0}^{5-j} a_{ij} Q_1^i Q_2^j, \quad (2.11)$$

where the segmented regions, V_{lkm} , were defined by a series of triangular cells.^{15,16} Each cell's function is described by 21 coefficients. These coefficients are determined using the value of the function, the first and second-order partial derivatives computed for the triangle vertices and the values of the partial derivative of the function computed perpendicular to each side of the triangle. This bivariate interpolation was applied to study potentials reduced to two-dimensions that were characterized by

one or more double wells. The National Center for Atmospheric Research Scientific Computing Division implementation of this approach was used.

2.3 VIBRATIONAL SPECTROSCOPY

2.3.1 INTRODUCTION

The vibrational energy states of a molecular system dictate how a system behaves. The importance of these vibrational states in terms of their fundamental relationship to molecular behavior and their extensive use in experimental identification of molecular systems have led to the development of several theoretical techniques. The simplest of approach is the normal mode analysis. A normal mode analysis yields the harmonic frequencies and corresponding normal mode coordinates of the molecular system. These are obtained by first generating, at a minimum configuration, a matrix of second-derivatives with respect to the displacement of each mass-weighted coordinate. This matrix is known as a Hessian matrix. The Hessian is then diagonalized with the eigenvalues and eigenvectors corresponding to the normal mode frequencies and coordinates. The dominant assumption taken in this calculation is that the behavior of molecular systems at minima can be approximated as a series of non-interacting harmonic oscillators. In reality, the vibrations of molecular systems are not harmonic and interact anharmonically with one another. Several methods have been developed to go beyond the harmonic approximation to include these important anharmonic effects.^{17,18,19,20,21,22,23,24,25,26,27,28}

In the following subsections three techniques are introduced which were applied in the course of this dissertation work to consider anharmonic effects in molecular systems. First, the discrete variable representation is discussed, which was used to compute vibrational ground and excited state properties for reduced dimensional systems.²³ Next, the methods implemented in the code Multimode are

summarized, which were used to study vibrational properties of higher dimensional systems.^{19,20,21,22} Finally, the technique diffusion Monte Carlo is introduced, which was used to solve for the ground state vibrational properties of molecular systems in a numerically exact manner.^{29,30}

2.3.2 DISCRETE VARIABLE REPRESENTATION

The discrete variable representation (DVR) technique was applied to study the vibrations of molecular systems which were reduced to one- or two-dimensions.²³ The DVR approach reformulates the kinetic energy operator of the Schrödinger equation

$$T = \frac{1}{2} \frac{d^2}{dQ^2}, \quad (2.12)$$

into a grid-point representation. The grid is equally spaced along the coordinates with corresponding Fourier functions as basis functions. This results in the DVR formulation of the kinetic energy operator

$$T_{ii'} = \frac{(-1)^{(i-i')}}{2\Delta Q^2} \left\{ \begin{array}{ll} \frac{\pi^2}{3}, & i = i' \\ \frac{2}{(i-i')^2}, & i \neq i' \end{array} \right\}. \quad (2.13)$$

The resulting one dimensional DVR Hamiltonian matrix is then

$$H_{ii'} = T_{ii'} + V(Q)\delta_{ii'}, \quad (2.14)$$

and in two dimensions is

$$H_{ii'jj'} = T_{ii'}\delta_{jj'} + T_{jj'}\delta_{ii'} + \delta_{ii'}\delta_{jj'}V(Q_1, Q_2), \quad (2.15)$$

where the potential energy resides only along the diagonal of the grids. Diagonalization of H yields the corresponding eigenvalues and eigenvectors of interest that

correspond to the vibrational states and wavefunctions of the system.

The advantage of the the DVR approach is its high flexibility to describe arbitrarily defined coordinate spaces. The computed solutions using the DVR approach are numerically exact so long as the potential along the coordinate space is well defined and the number of grid points is sufficiently high. The extension of this approach to larger dimensional systems is computationally challenging, as the size of the H matrix grows exponentially with the number of dimensions. In order to solve larger dimensional problems, two separate approaches are considered in this dissertation.

2.3.3 MULTIMODE

The Multimode program was utilized to compute spectral properties for molecular systems of various sizes.^{19,20,21,22} The program is designed to compute vibrational properties of molecular systems by solving the Watson Hamiltonian in terms of a n -mode representation of the potential. The Watson Hamiltonian for systems with $J = 0$ is given by

$$\hat{H} = \frac{1}{2} \sum_{\alpha\beta} \hat{\pi}_\alpha \hat{\pi}_\beta \mu_{\alpha\beta} - \frac{1}{2} \sum_k \frac{\partial^2}{\partial^2 Q_k^2} - \frac{1}{8} \sum_\alpha \mu_{\alpha\alpha} + V(\mathbf{Q}), \quad (2.16)$$

where α and β are the Cartesian x, y, z coordinates, $\hat{\pi}_\alpha$ is the vibrational angular momentum operator, μ is the effective reciprocal inertia tensor, and $V(\mathbf{Q})$ is the normal coordinate, \mathbf{Q} , dependent potential. In the Multimode calculations $V(\mathbf{Q})$ is evaluated in terms of an n -mode representation of the potential

$$V(Q_1, Q_2, \dots, Q_N) = \sum_i V_i^{(1)}(Q_i) + \sum_{ij} V_{ij}^{(2)}(Q_i, Q_j) \dots + \sum_{i..N} V_{i..N}^{(N)}(Q_i, \dots, Q_N). \quad (2.17)$$

Each of the terms in the n -mode representation correspond to the potential varied along a limited set of normal coordinates such that the term $V_i^{(1)}$ is the potential energy where Q_i is the only non-zero normal coordinate, $V_{ij}^{(2)}$ is the potential energy

given by $V(Q_i, Q_j) - (V_i^{(1)} + V_j^{(1)})$ where both Q_i and Q_j are non-zero, and $V_{i..N}^{(N)}$ is the potential energy when all coordinates are non-zero and the lower-order terms have been subtracted. The n -mode representation allows for each of the terms to be integrated independently, that is to say, single-mode, two-mode, n -mode integration. Due to computational limitations, the n -mode representation in Multimode is limited to $n = 6$. The truncation of the n -mode representation at 6 and in some cases lower can be justified by considering the convergence of the representation starting from $n = 1$ and systematically increasing.

The Watson Hamiltonian eigenvalues and eigenfunctions are solved for using vibrational configuration interaction theory (VCI). In this approach, an initial trial wavefunction is first constructed from vibrational self-consistent field solution theory (VSCF) as the product of the N single mode wavefunctions

$$\Psi_{n_1, n_2, \dots, n_N}^{VSCF}(Q_1, Q_2, \dots, Q_N) = \prod_{i=1}^{(N)} \phi_{n_i}^{(i)}(Q_i), \quad (2.18)$$

where each $\phi_{n_i}^{(i)}$ is the eigenstate of i^{th} single mode function. The variational best forms of $\phi_{n_i}^{(i)}(Q_i)$ are obtained by solving the set of coupled VSCF equations

$$\left(-\frac{1}{2} \frac{\partial^2}{\partial Q_k^2} + \left\langle \prod_{i \neq l}^N \phi_{n_i}^{(i)} \right| V + \frac{1}{2} \sum_{\alpha\beta} \hat{\pi}_\alpha \hat{\pi}_\beta \mu_{\alpha\beta} - \frac{1}{8} \sum_{\alpha} \mu_{\alpha\alpha} \left| \prod_{i \neq l}^N \phi_{n_i}^{(i)} \right\rangle - \epsilon_{n_l}^{(l)} \right) \phi_{n_l}^{(l)}(Q_l) = 0, \quad (2.19)$$

where the integration is performed over $N - 1$ single mode functions. These equations are solved iteratively for each single mode using a finite basis representation where the basis functions are harmonic oscillator wavefunction. The resulting VSCF solutions describes each vibrational coordinate in the effective potential of the other coordinates. In order to explicitly consider coupling of modes, the virtual states of the VSCF ground state are used to expanded the VCI many-mode wavefunction. The ground state VSCF provides an orthonormal basis that results in a generalized

eigenvalue problem. Diagonalization of the resulting VCI matrix using standard techniques yields the desired vibrational states and wavefunctions given in terms of the contributing VSCF states. I note that the later approach was the one taken in the present dissertation work but there are other approaches that are available in the Multimode program.

When considering problems in high dimensionality, the VCI Hamiltonian can be quite large. In order to allow for efficient computations a highly flexible approach is used to construct the VCI basis set. The number of quanta of excitation from the ground state can be explicitly defined for each mode and for each collection of modes, that is to say the number of quanta of excitations when one-mode, two-modes, etc., are excited is pre-defined.

In order to perform the calculations performed in this work a slight modification was made to the standard Multimode packages, 4.9.0 and 5.1.3. Traditionally Multimode requires all $3N - 6$ normal coordinates to be considered where N is the number of atoms. The modification allowed for an arbitrary number of pre-specified normal mode coordinates between 1 and $3N - 6$ to be considered.

If a dipole moment surface is available, the Multimode program, after computing the vibrational states and wavefunctions, can be used to compute pure vibrational infrared intensities. This is done by solving the transition dipole matrix elements for each excited state

$$R_{\nu\nu'}^{\alpha} = \langle \Psi_{\nu}(\mathbf{Q}) | \mu^{\alpha}(\mathbf{Q}) | \Psi_{\nu'}(\mathbf{Q}) \rangle, \quad (2.20)$$

where $\Psi_{\nu}(\mathbf{Q})$ and $\Psi_{\nu'}(\mathbf{Q})$ are the vibrational wavefunctions of ν and ν' , respectively, μ^{α} the component of the molecular fixed dipole moment $\vec{\mu}$ for one of the three cartesian coordinates indexed by α . The integration is performed in the normal coordinates, which allows for the dipole to be considered in an n -mode representation similar to the potential.

2.3.4 DIFFUSION MONTE CARLO

An implementation of the diffusion Monte Carlo (DMC) method was used to obtain numerically exact solutions to the ground state energy and wavefunctions of molecular systems in full dimensionality.^{29,30} The DMC approach begins with the time-dependent Schrödinger equation

$$ih\frac{\partial\Psi}{\partial t} = \frac{\hbar^2}{2m}\frac{\partial^2\Psi}{\partial x^2} + V(x)\Psi, \quad (2.21)$$

where

$$\Psi(x, t) = \sum_{n=0}^{\infty} c_n \phi_n(x) e^{-\frac{i}{\hbar} E_n t}. \quad (2.22)$$

In Ψ , the $\phi_n(x)$ and E_n are the eigenfunctions and eigenvalues of the time independent Schrödinger equation. Two transformations are performed to the above equations to prepare for the DMC calculation, a shift in energy scale by a constant energy E_r and transformation into imaginary time

$$h\frac{\partial\Psi}{\partial\tau} = \frac{\hbar^2}{2m}\frac{\partial^2\Psi}{\partial x^2} - [V(x) - E_r]\Psi, \quad (2.23)$$

and

$$\Psi(x, \tau) = \sum_{n=0}^{\infty} c_n \phi_n(x) e^{-\frac{E_n - E_r}{\hbar} \tau}. \quad (2.24)$$

Implicit in the imaginary time wavefunction, when $n = 0$, are the following asymptotic behaviors: if $E_r > E_0$, $\lim_{\tau \rightarrow \infty} \Psi = \infty$, the wavefunction diverges exponentially fast; if $E_r < E_0$, $\lim_{\tau \rightarrow \infty} \Psi = 0$, the wavefunction vanishes exponentially fast; if $E_r = E_0$, $\lim_{\tau \rightarrow \infty} \Psi = c_0 \phi_0$, the wavefunction converges to the ground state wavefunction. The latter convergence provides the basis for computing the ground state energy, E_0 and wavefunction ϕ_0 for molecular systems in the DMC approach.

Integration of the imaginary time Schrödinger equation can be performed by ap-

plying path integral or diffusion-reaction formalisms. Both lead to an algorithmic solution based on standard Monte Carlo stochastic integration. The later technique is, however, limited to when the wavefunction can be considered as a positive definite probability density, which is true in the case of a ground state wavefunction. The algorithm begins by considering a numerical representation of $\Psi(x, \tau)$ where the wavefunction is defined by points in configuration space known as “walkers.” These “walkers” can be simulated forward in imaginary time according to a random walk under a birth-death process, where “walkers” are generated or removed depending on their energy and the mean energy of all “walkers.” The average energy of the all the “walkers” will eventually converge to the true value of E_r that is equivalent to the value of E_0 and ψ_0 .

More explicitly, the calculations start by defining an imaginary time-step $\Delta\tau$, an inversely proportional “feedback” parameter α , the number of initial “walkers” N_0 , a equilibration time, a total simulation time, and a initial guess of the average ground state wavefunction structure. The value of $\Delta\tau$ is selected to be small enough to avoid substantial systematic error in discretizing the imaginary time but large enough not to result in exhaustive computing time. Similar considerations are made in the selection of N_0 to ensure enough walkers are present to numerically represent the wavefunction but not so many that the computational cost is too great. The equilibration time is chosen to be long enough to allow the “walkers” to equilibrate to a converged state. The propagation time after the equilibration time is performed to allow for better statistical estimates of the ground state energy.

The simulations begins with a collection of N_0 “walkers” initialized as a dirac δ -function at the guess of the average ground state configuration,

$$\Psi(\mathbf{x}_0, 0) = \delta(\mathbf{x} - \mathbf{x}_0), \quad (2.25)$$

where \mathbf{x} contains a list of the N walkers each characterized by M dimensions. The “walkers” are propagated forward according to a gaussian random walk wherein the “walkers” positions are changed according to

$$x_j^i = x_j^{i-1} + \rho_j^i \cdot \sigma, \quad (2.26)$$

where j indexes to the “walkers,” i indexes the time steps, ρ is a vector of random numbers taken from a gaussian distribution with a 0 mean and variance of 1, $\sigma = \sqrt{\hbar\Delta\tau/m}$ and m is a vector of atom masses. A weight for each new x_j^i configuration is computed

$$W(x_j^i) = e^{-\Delta\tau \frac{V(x_j^i) - E_r}{\hbar}} \quad (2.27)$$

along with an integer $m = \min(\text{int}[W(x_j^i) + u], 3)$, where the int function returns an integer value and u is a random number between 0 and 1. The value of m determines what occurs to a given “walker” such that, if $m = 0$ the “walker” is removed, if $m = 0$ the “walker” remains, and if $m > 1$ then $m - 1$ replicas of the walker are added. The final number of “walkers” is updated as N_i . A new reference energy is then computed according to

$$E_r = \langle V_i \rangle - \alpha \frac{N_i - N_0}{N_0}, \quad (2.28)$$

where α is the empirically identified value chosen at the start of the simulation in order to remove smaller unwanted correlations between the $i - 1$ and i “walker” distributions. The process iterates for the specified number of steps, with the final ground state energy computed from the converged portion of the simulation.

In a DMC simulation the convergence regularly occurs within the first 2000 imaginary time steps. The remaining simulation time is then used to compute the ground state energy. Specifically, in this dissertation work the ground state energy was calculated by dividing the converged simulation into separate blocks from which an average E_0 was computed. The average of the all blocks E_0 was computed with the standard

deviation taken to be the statistical uncertainty in the ground state.

A powerful results of the DMC simulations is the ability to generate three-dimensional visualizations of ground state wavefunctions. This is achieved by transforming the final collection of xyz coordinates generated by the DMC simulations into a readable Gaussian cube file. These files were generated by first transforming each of the “walkers” into the Eckart frame relative to a minima or transition state configuration, which is most similar to the average ground state configuration. In order to ensure proper symmetry in the visualized wavefunctions, the coordinates were often duplicated and reflected across appropriate axes. A quartic kernel density estimator was then applied to the spatial coordinate to compute volumetric elements for each type of atom. These volumetric elements were then written to a Gaussian cube file and visualized using the VMD package. The code used to performed this transformation was developed by Volodymyr Babin who first applied it in Reference [31]. It is important to note that while the DMC results are numerically exact, the visualization of the wavefunctions are interpreted qualitatively. This is because for each rendered wavefunction an isovalue, which controls the size of the volume elements shown rendered, must be selected. This value is selected empirically often with support from observations of the same system’s wavefunction computed using reduced dimensional calculations.

2.4 QUASI-CLASSICAL SIMULATION

Time-dependent quantum mechanical studies of molecular systems greater than four atoms are extremely difficult to due to the large number of degree-of-freedom. Therefore, in studies performed in this dissertation an approximation to the true dynamics known as quasi-classical dynamics is considered instead.^{32,33} In these simulations the quantum effects are considered solely in terms of the initial conditions of the system. This simplification give a large speed advantage over other techniques. The quasi-

classical approach treats the nuclear motion classical using Hamilton's equations of motion

$$H = T(\mathbf{p}) + V(\mathbf{q}), \quad (2.29)$$

$$\frac{d\mathbf{p}}{dt} = -\frac{\delta H}{\delta \mathbf{q}}, \quad (2.30)$$

$$\frac{d\mathbf{q}}{dt} = +\frac{\delta H}{\delta \mathbf{p}}, \quad (2.31)$$

where \mathbf{q} are the atomic coordinates, \mathbf{p} the conjugate momenta, t the time, m the mass, T the kinetic energy and V the potential energy. Important effects of zero-point motion are considered in the simulations by first computing the system's harmonic frequencies and then initializing the zero-point energy into the computed normal mode coordinates. Similarly, the effects of vibrational excitations are accounted for by adding additional energy into specified normal mode coordinates. The total simulation energy is considered as the sum of the ground state energy

$$E_{\text{ground}} = \sum_{i=1}^n \frac{1}{2} \omega_i, \quad (2.32)$$

where n is the total number of normal modes and ω and the excited state energy

$$E_{\text{excited}} = \sum_{j=1}^e \omega_j, \quad (2.33)$$

where the sum is over the indices of the modes that are chosen to be excited. The total energy is divided between the kinetic and potential energy of the system according to

$$E_{\text{total}} = E_{\text{ground}} + E_{\text{excited}} = \sum_{i=1}^n \frac{1}{2} P_i^2 + \frac{1}{2} \omega_i^2 Q_i^2, \quad (2.34)$$

where the Q_i and P_i are the normal mode coordinates and the momentum along those coordinates, respectively. The Q_i and P_i values are initialized by

$$Q_i = \frac{\sqrt{2E_i}}{\omega_i} \cos(2\pi R_i), \quad (2.35)$$

and

$$P_i = -\sqrt{2E_i} \sin(2\pi R_i), \quad (2.36)$$

where E_i is the energy associated with normal mode i and R_i a random number between 1 and 0.

Once the system is initialized in this manner, the true PES anharmonic energy is computed. Due to the harmonic assumption and random initialization, the total anharmonic energy is rarely the same between simulations. This is corrected for by scaling the velocities to match either the value given by E_{total} . When anharmonic excited state and zero-point energies are available the velocities can be further scaled to match the anharmonic values. It is worth mentioning that regardless of this scaling the resulting dynamics are fully anharmonic in nature.

The computational cost of performing QCT simulations is much lower than other more complex approaches.^{34,35} This is particularly useful when several thousand of simulations are required to study the distributions of molecular properties and to identify rare events. The classical treatment does however lead to the “quantized” energy leaking from the initialized modes. When the leaking energy is associated with the zero-point energy of the system it results in classical systems with no quantum mechanical analog. In the case of dissociation dynamics, products whose zero-point energies are lower than their true quantum mechanical can have unphysically large rotational or translational energy. The effects of this zero-point energy leak are accounted for after the fact by excluding simulations whose products have vibrational energy lower than the appropriate harmonic or anharmonic zero-point energy amount.

The computational cost of performing simulations that do not have proper zero-point energy and must be discarded is off-set by the low cost of performing each simulation. The energy leakage effect can also be utilized to study vibrational relaxation dynamics where the initialized energy is associated with excitation energy and the relaxation rate and relaxed dynamics can be studied.

3

$(\text{HCl})_n$ Clusters

3.1 OVERVIEW

Hydrogen halides are the simplest forms of hydrogen bonded clusters. Their diatomic nature allows for highly directional interactions with the hydrogen atom donating a hydrogen bond and the halide atom accepting another. The simplicity of these diatomics have garnered significant scientific interest due to the detailed level of molecular insight that can be obtained from their study. In the following chapter theoretical studies performed specifically on the hydrogen halide cluster, $(\text{HCl})_n$, are reported.

This chapter is broken into three sections as follows. The first section details an on-

the-fly approach to computing the anharmonic vibrational frequencies for molecular systems. This technique is applied to HCl clusters ranging from the HCl dimer to the hexamer with direct comparisons made with experimental peak positions. The second section describes the construction of a new many-body potential energy surface to describe arbitrary sized HCl clusters. The new surface is used to study vibrational properties of HCl clusters including a unique example of vibrational energy transfer in the HCl trimer. The final section presents an application of the new HCl potential energy surface to gain a detailed understanding of the vibrational predissociation behavior of the HCl trimer. This work was performed with a parallel experimental investigation of the system, conducted by Dr. Amit K. Samanta and Dr. Hanna Reisler at the University of Southern California.

3.2 ON-THE-FLY AB INITIO CALCULATIONS OF ANHARMONIC VIBRATIONAL FREQUENCIES: LOCAL-MONOMER THEORY AND APPLICATION TO HCL CLUSTERS

3.2.1 CONTEXT

In order to fully understand the behavior of molecules in the bulk phase, studies have been performed on well-characterized molecular clusters.^{36,37,38,39,40,41,42} Examination of these clusters provides detailed information about the interactions that influence the bulk phase. In each cluster the monomers are connected to their neighbors by weak intermolecular interactions. The cooperative effects of these forces can often be observed in the changes of vibrational frequencies as molecular clusters grow in size. These vibrational shifts are readably measured from IR spectroscopy.^{43,44} However, the assignment of the vibrational frequencies, purely from experimental results can be extremely difficult. The measured spectra can become complicated by many factors including, multiple low-lying cluster conformations, combination bands, overtones and multiple isotopes. These effects become more prominent as clusters grow

in size; preventing a clear understanding of their growth. Theoretical calculations of anharmonic vibrational frequencies are key to interpreting these spectra.

The theoretical computation of anharmonic frequencies is a challenging endeavor. Exact solutions of molecular vibrations for up to four atoms are readily available.²⁷ Additional techniques allow for *near* exact solutions for as many as nine atoms.^{24,25,26} In systems greater than nine atoms, calculations become difficult due to the large number of degrees of freedom and the high cost of electronic structure calculations. When the anharmonic frequencies of large systems are pursued, approximations are applied in the form of quantum calculations with limited mode coupling¹⁷ or calculations based on classical mechanics.²⁸ More commonly, anharmonic frequencies of large systems are obtained by avoiding explicit calculations of anharmonicity, but instead add anharmonic effects with empirical scaling factors. These factors have been derived from comparisons between experimental frequencies and harmonic frequencies calculated for specific combinations of electronic structure methods and basis sets.^{45,46} This empirical approach, however, can fail “without warning,” and so is not an ideal solution.

Recently it was reported that the use of scaled harmonic frequencies and double-harmonic intensities hampered the correct interpretation of the water hexamer spectrum.⁴⁷ In contrast, a purely theoretical approach, known as the local-monomer model (LMon), was able to compute frequencies and intensities, including the bend overtone, in very good agreement with the experimental values.⁴⁸ The LMon approach is a “divide and conquer” technique that solves for a cluster’s anharmonic frequencies by first computing each isolated monomer’s normal-modes in the frozen field of all other monomers. The local-monomer normal-modes are then used with an appropriate Hamiltonian to obtain the anharmonic vibrational frequencies. The LMon method has been applied with accurate full-dimensional potential energy surfaces to water clusters ranging from the dimer⁴⁸ to 192-monomers⁴⁹ as well as to the micro-

hydration of atomic ions.^{50,51,52} In studies of clusters with degenerate and near degenerate LMon mode vibrations, such as the water ring tetramer, degeneracy breaking monomer-monomer coupling was considered with the Hückel-coupling approach, (described in detail below).⁵³

The LMon-Hückel approach is a highly versatile and efficient framework for studying molecular clusters. To demonstrate this the model is applied here without a full-dimensional potential energy surface. This type of *on-the-fly*, “first-principles”, calculation is ubiquitous, but predominately in classical molecular dynamics. Typical quantum calculations for larger systems, even just a normal-mode analysis, can require a prohibitively large number of electronic structure energies. Going beyond the harmonic approximation using straightforward approaches is simply not feasible. This is perhaps best illustrated by the recent Communication reporting seven degrees-of-freedom direct dynamic, coupled anharmonic, calculations as the current limit of such calculations.⁵⁴ The LMon method provides a promising framework for direct, *on-the-fly*, quantum applications.

Even the application of the LMon-Hückel to a large cluster in this direct fashion is hampered by the exponential scaling of electronic structure calculations for the full normal-mode analysis required by the Hückel-coupling approach. In order to overcome this limitation, a composite *ab initio* technique is proposed for treating the potential energies in the LMon-Hückel approach. The composite technique applies two separate electronic structure methods to solve for the vibrational frequencies. A computationally efficient method capable of accurate geometry prediction, e.g, MP2, is chosen as the first method method and used for the geometry optimization and harmonic analyses. A more accurate method, e.g., CCSD(T), is then used to determine the energies for the anharmonic calculation. The resulting anharmonic frequencies from the composite method are found to produce frequencies comparable to those calculated solely at the higher level of theory, but at substantially less cost. This

composite approach is analogous to the practice used in energetic studies of large molecular systems where structures are optimized using a lower level of theory, and then the energy evaluated using a higher level single point calculation.

The LMon-Hückel approach and its proposed composite formalism is applied here to hydrogen chloride (HCl) clusters. These diatomic molecular clusters allow the LMon approaches to be tested in their simplest form due to the one-dimensional nature of the HCl stretches.

The study of HCl clusters, specifically (HCl)₂₋₆, shown in Figure 3.1 remains a topic of continued experimental interest. The dimer is the most studied of these clusters.^{55,56,57,58,59,60,61,62,63,64,65,66,67,68,69} It is characterized by a single weak hydrogen bond and a large amplitude motion by which the hydrogen donating and accepting monomers can interchange. The weak hydrogen bonding results in a ground state splitting of 15 cm⁻¹.⁶¹ Multidimensional potential energy surfaces^{67,66,63} have been generated and applied in full, six-dimensional, solutions to the vibrational Schrödinger equation.^{63,64} The trimer has been the focus of considerable effort experimentally.^{70,71,59,72,73,74} In the trimer, (HCl)₃, a “closed-shell” of hydrogen bonds is capable of forming.⁷⁵ Each monomer donates and accepts a single hydrogen bond creating a triangle with C_{3h} symmetry in its lowest energy configuration. This cluster has been studied using high-resolution spectroscopy to determine the excitation energy of the H-Cl stretch in the gas phase.^{71,59} Owing to the high symmetry of this cluster it might be naively concluded that there is a single excitation energy resulting from the equivalence of the three HCl units. The monomers are indeed identical; however, from both spectroscopy and theory it is observed that the three-fold symmetry is broken slightly, in the space of excitation. This symmetry breaking is due to dynamical monomer-monomer coupling, which is directly related to the vibration-vibration energy. The next cluster, the tetramer, has been studied to a lesser extent relative to the smaller clusters.^{70,59,76,72} The minima of the tetramer is characterized

by a puckered ring conformation with four degenerate HCl subunits. The final two clusters, the pentamer and hexamer, both present challenges to modern experimental spectroscopy as well as theory. Both are characterized by lower symmetry than the smaller clusters and a breakdown of the single-ring conformation. These conformational changes can result in broader, less structured spectra and the loss of the size-dependent frequency shift. The pentamer, while still described by a ring at its global minima begins to fold onto itself resulting in five unique monomer subunits. The hexamer loses the single ring conformation and is instead best described as two perturbed trimer clusters stacked on top of each other. The perturbed stacking results in only three unique monomer units describing the cluster. In helium nanodroplets⁷⁰ both clusters were assigned, but only a tentative assignment was made for the pentamer using the ragout-jet FTIR technique.⁷⁶

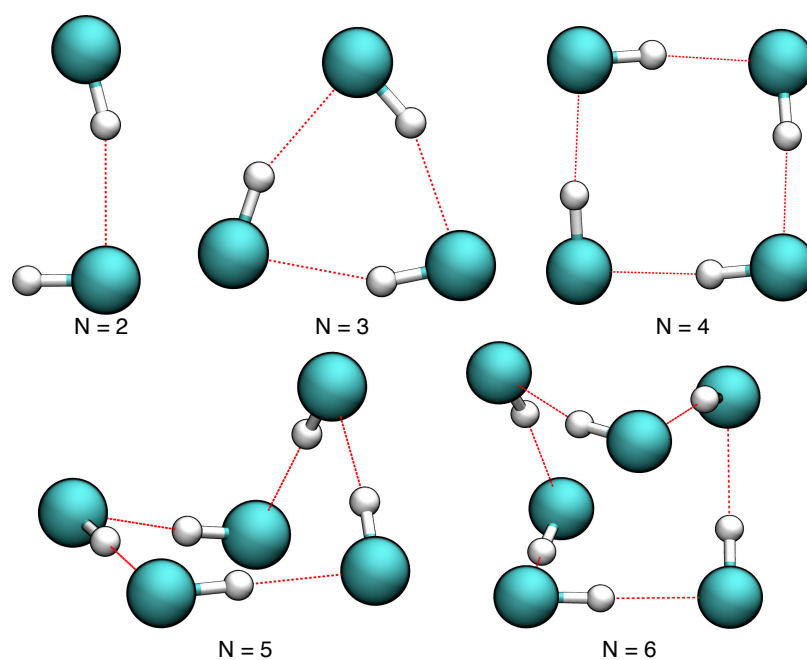


Figure 3.1: Global minimum geometries of HCl clusters.

3.2.2 METHODS FOR PERFORMING ON-THE-FLY VIBRATIONAL CALCULATIONS

Local-Monomer Model

The local-monomer (LMon) model solves the Schrödinger equation in terms of the LMon normal-modes of each monomer embedded in the cluster. The LMon modes are determined, in the specific case of the HCl clusters, from diagonalizing monomer-centric 6×6 Hessians. The resulting LMon modes for a HCl monomer correspond to five low-frequency frustrated translations and rotations and a single high-frequency intramolecular stretch. The simplest and fastest possible application of the LMon method is presented here, which ignores explicit coupling of the stretch to the low-frequency modes. Following this assumption, the 1D Schrödinger equation to be solved is,

$$[T_i + V_i(Q_i) - \epsilon_{n_i}] \chi_{n_i}(Q_i) = 0, \quad (3.1)$$

where i is the specific monomer, Q_i is the LMon intramolecular coordinate, T_i is the kinetic energy, V_i is the potential energy, ϵ_{n_i} the n_i^{th} energy level and χ_{n_i} the n_i^{th} wavefunction. The solution to Equation 3.1 is determined by first generating a 1D potential from a 10^{th} order polynomial fit from 17 *ab initio* energies along the stretching coordinate, Q_i . The *ab initio* energies are non-equally spaced along Q_i to allow for optimal fitting and to span the range of the 1D wavefunction. The potential is then discretized into a 1000 points and the Schrödinger equation solved using the discrete variable representation (DVR).²³ Based on the difference between the ground and first excited state levels in the DVR calculation, the LMon anharmonic fundamental frequency is calculated.

Hückel-Coupling

The harmonic frequencies from the LMon method for a cluster, Ω_i , can be compared to those from a full normal-mode analysis, ω_i . The differences between the two frequencies are expected to be small. However, when degeneracies and near degenera-

cies occur in the LMon results, additional monomer-monomer coupling can be added to bring the LMon frequencies into agreement with the full normal-mode frequencies. This monomer-monomer coupling is added via a Hückel-coupling matrix.⁵³ In the simplest case a single nearest neighbor coupling constant, β_0 , is considered. This coupling constant and the LMon frequencies are arranged into a matrix and diagonalized to give a new set of frequencies, $\tilde{\omega}$, approximately equal to the full normal-mode frequencies, ω . An example of the application of nearest neighbor coupling for the HCl trimer stretches is,

$$\begin{bmatrix} \Omega_1 & \beta_0 & \beta_0 \\ \beta_0 & \Omega_2 & \beta_0 \\ \beta_0 & \beta_0 & \Omega_3 \end{bmatrix} \Rightarrow \begin{bmatrix} \tilde{\omega}_1 & 0 & 0 \\ 0 & \tilde{\omega}_2 & 0 \\ 0 & 0 & \tilde{\omega}_3 \end{bmatrix}, \quad (3.2)$$

where the double arrow refers to the diagonalization of the matrix. This coupling can and is also considered here even in the absence of such degeneracies. For clusters larger than the trimer, multiple coupling constants are required to account for farther than nearest neighbor coupling and bring the LMon and normal frequencies into agreement. The multiple coupling constant matrix for the HCl tetramer is,

$$\begin{bmatrix} \Omega_1 & \beta_1 & \beta_2 & \beta_1 \\ \beta_1 & \Omega_2 & \beta_1 & \beta_2 \\ \beta_2 & \beta_1 & \Omega_3 & \beta_1 \\ \beta_1 & \beta_2 & \beta_1 & \Omega_4 \end{bmatrix} \Rightarrow \begin{bmatrix} \tilde{\omega}_1 & 0 & 0 & 0 \\ 0 & \tilde{\omega}_2 & 0 & 0 \\ 0 & 0 & \tilde{\omega}_3 & 0 \\ 0 & 0 & 0 & \tilde{\omega}_4 \end{bmatrix}, \quad (3.3)$$

where two unique coupling constants, β_1 and β_2 , are used. These coupling constants are then used to modify the LMon anharmonic frequencies of a cluster by simply substituting these for the Ω 's and diagonalizing the resulting matrix.⁵³

The values of coupling constants are determined as parameters in least-squares fits of the split local-monomer model frequencies (LMon _{β_i}) and the full normal-mode fre-

quencies. A general approach to calculating the constants was derived previously⁵³ and involves treating the LMon analysis as an approximation to the full normal-mode analysis.

Composite Ab Initio Approach

In the case of large HCl clusters, geometry optimizations and normal-mode analysis using an accurate electronic structure method e.g., coupled-cluster, requires a large amount of computer time. Due to the high cost, a composite *ab initio* technique is proposed. It is applied to the LMon calculations of anharmonic frequencies for the pentamer and hexamer clusters with preliminary tests applied to the dimer, trimer and tetramer. In the composite technique two *ab initio* methods, which are referred to here as *A* and *B*, are applied. The first method, *A*, is chosen to be a method which can efficiently and accurately predict cluster stationary points. It is used to compute an optimized cluster geometry, perform full and LMon harmonic normal mode analyses and derive Hückel-coupling constants. The second method in the approach, *B*, is selected to be more accurate than *A*, either by including a higher level of electron correlation or a larger basis set. This method is used to compute energies along the LMon mode, HCl stretch, determined from *A* at the minima determined with *A*. The resulting 1D potential, using *B* energies, is then used to calculate LMon anharmonic frequencies. Monomer-monomer coupling is added to these composite LMon frequencies via the coupling constants determined from *A*. The anharmonic frequencies computed with the composite *ab initio* technique are exactly equal to calculation of anharmonic frequencies with *B* when, *A* is able to optimize the cluster to the identical conformation as *B*, and the monomer-monomer coupling derived from the harmonic frequencies using *A* is the same as the coupling in *B*.

Ab Initio Calculations

The global minimum geometries of (HCl)₂₋₆ optimized using CCSD(T)-F12b/aug-cc-pVTZ (aVTZ) theory for the dimer, CCSD(T)-F12b/aug-cc-pVDZ (AVDZ) for

the trimer and tetramer and MP2/6-311++G(3df,3dp) for the pentamer and hexamer can be seen in Figure 3.1. All geometry optimizations were performed starting from the coordinates reported in the Supplementary Information of Ref^[70]. Additional specifics of the *ab initio* methods used in the vibrational analyses are detailed in the following section. All calculations are for Chlorine-35. Electronic structure calculations were performed using MOLRPO 2010.⁷⁷

3.2.3 ON-THE-FLY (HCL)₁₋₆ VIBRATIONAL FREQUENCIES

Monomer

Before reporting on the HCl clusters it is prudent to examine the accuracy of electronic structure methods with respect to the isolated HCl monomer. Anharmonic and harmonic fundamental vibrational frequencies calculated using different levels of theory are reported in Table 3.1 for the monomer along with a benchmark experimental value.⁷⁸ Previous *ab initio* calculations using MRCI and an aug-cc-pV5Z (aV5Z) basis set are in effectively exact agreement with the experimental value.⁷⁹ The frequency of the most rigorous anharmonic calculation, CCSD(T)-F12b/aV5Z, red shifts 6 cm⁻¹ relative to experiment. Reducing the basis set of the CCSD(T)-F12b calculation to aVTZ and aVDZ further red shifts the frequency. When MP2/6-311++G(3df,3pd) is applied, the resulting frequency is red shifted 76 cm⁻¹ from experiment. This apparent failure of MP2 motivates the application of the higher level methods used for the 1D calculation of HCl fundamental energies.

Table 3.1: Harmonic and anharmonic frequency (cm⁻¹) of HCl monomer using different electronic structure methods.

Method	Anharmonic	Harmonic
CCSD(T)-F12b/aV5Z	2892	3009
CCSD(T)-F12b/aVTZ	2891	2994
CCSD(T)-F12b/aVDZ	2906	2996
MP2/6-311++G(3df,3pd)	2962	3057
MRCI/aug-cc-pV5Z ⁷⁹	2886	2993
Experiment ⁷⁸		2886

Dimer

In Table 3.2, harmonic frequencies from full and LMon normal-mode analyses of the dimer are reported using two different electronic structure methods, CCSD(T)-F12b/aVTZ and MP2/6-311++G(3df,3pd). The local-normal-mode analysis LMon frequencies of the dimer are seen to be in near exact agreement with the full normal-mode frequencies using either electronic structure method. Harmonic frequencies computed using MP2 are closer to those computed using the CCSD(T)-F12b, than in the monomer. While this might indicate vibrational frequency calculations of HCl clusters can be performed using MP2, the subsequent large clusters, reported on below, do not show agreement between MP2 and CCSD(T) results. In addition to the reasonable agreement between harmonic frequencies, the two methods give similar global minima, with bond distances, hydrogen bond lengths and angles differing by less than 0.01 Å and 2° respectively.

Table 3.2: Harmonic frequencies (cm⁻¹) of the HCl dimer from indicated calculations see text for details.

Mode	MP2/6-311++G(3df,3pd)		CCSD(T)-F12b/aVTZ	
	Full	LMon	Full	LMon
ν_1	3005	3005	2976	2977
ν_2	2962	2961	2951	2957

Moving beyond harmonic analysis, computed anharmonic frequencies are reported in Table 3.3 where the frequencies listed under the header with two methods used the

composite technique for computing the *ab initio* energies. MP2/6-311++G(3df,3pd), was used for the geometry optimization and harmonic analyses and CCSD(T)-F12b/aVTZ was used to determine the energies of the 1D potential cuts. Frequencies computed using the composite technique henceforth are referred to by the second electronic structure method listed. Table 3.3 also reports benchmark theoretical results, which used a full-dimensional treatment of the system. The composite CCSD(T)-F12b/aVTZ frequencies are in very good agreement with the results obtained using the traditional, non-composite, technique, differing by less than 2 cm⁻¹. The LMon method used here is the simplest possible calculation of anharmonic frequencies for the dimer, requiring (in addition to the geometry optimization and LMon analysis) only 17 electronic structure energies per mode. Even with this simple approach good agreement is achieved with the previous benchmark calculations reported by Ref[63], which required the use of a full, six-dimensional, surface to compute. (Note, however, those calculations account for the interchange tunneling splitting, which is ignored in the present calculations.)

Table 3.3: Anharmonic frequencies (cm⁻¹) of the HCl dimer from calculations using the LMon-Hückel approaches as described in the text and comparisons with benchmark six-dimensional results.

Mode	CCSD(T)-F12b/aVTZ	MP2/6-311++G(3df,3pd) CCSD(T)-F12b/aVTZ	Ref[63]
	LMon	LMon	6D
ν_1	2876	2877	2874
ν_2	2830	2832	2857

Trimer

Both MP2/6-311++G(3df,3pd) and CCSD(T)-F12b/aVDZ levels of theory predict a global minimum with D_{3h} symmetry. The geometric parameters of the two predicted geometries are in close agreement. The MP2/6-311++G(3df,3pd) calculation predicts HCl and hydrogen bond lengths to be 0.006 Å and 0.031 Å longer than the CCSD(T)-F12b/aVDZ geometry. Both methods find a 2 : 1 degeneracy pattern in

the full normal-mode frequencies and a three-fold degeneracy in the LMon frequencies, reported in Table 3.4.

Table 3.4: Harmonic frequencies (cm^{-1}) of the HCl trimer from indicated calculations, see text for details.

Mode	MP2/6-311++G(3df,3pd)			CCSD(T)-F12b/aVDZ		
	Full	LMon	LMon _{β_0}	Full	LMon	LMon _{β_0}
ν_1	2916	2940	2879	2879	2900	2880
ν_2	2952	2940	2910	2910	2900	2910
ν_3	2952	2940	2910	2910	2900	2910
β_0	-12.10			-10.02		

The LMon method predicts a single degenerate frequency using either electronic structure theories, as opposed to the 2 : 1 pattern due to the lack of monomer-monomer coupling in the calculations. This is corrected by applying the Hückel-coupling approach, given for the trimer by Equation 3.2. In Equation 3.2 the matrix on the left hand side contains the monomer-monomer coupling constant, β_0 , given in Table 3.4 and the LMon frequencies, Ω . The right hand side matrix consists of the eigenvalues of the left, where $\tilde{\omega}$ are the coupled LMon _{β_0} frequencies. Considering that the LMon can be described by a single triply-degenerate frequency, Ω_0 , the analytical solutions for the eigenvalues to Equation 3.2 are $\Omega_0 + 2\beta_0$ and $\Omega_0 - \beta_0$, with the former eigenvalue being doubly degenerate. The splitting pattern and more explicitly the LMon _{β_0} frequencies are in perfect agreement with the full normal-modes frequencies for the respective electronic structure calculations. Comparison of the frequency values of the two electronic structure methods finds the MP2/6-311++G(3df,3pd) full and LMon frequencies are all red shifted approximately 40 cm^{-1} from the CCSD(T)-F12b/aVDZ values. However, the coupling constants of the two methods only differs by 2 cm^{-1} . It is worth noting that Equation 3.2 has been used previously by Fárník and Nesbitt as part of an exciton model,⁸⁰ which they used to help assign the spectra of the HCl trimer’s isotopologues. While the LMon-Hückel approach follows in the

spirit of the exciton model, the two methods are distinctly different, and considering their difference, agreement between two models' results is not expected.

Anharmonic frequencies are given for the trimer in Table 3.5. Looking at the traditional and composite CCSD(T)-F12/aVDZ LMon frequencies in Table 3.5, the two methods' triply-degenerate frequency shows excellent agreement with a difference less than 10 cm⁻¹. The three-fold degeneracy in both approaches is corrected when Equation 3.2 is applied, using the anharmonic LMon values for Ω and the β_0 values in Table 3.4. The resulting coupled anharmonic frequencies, LMon _{β_0} , have the proper 2 : 1 degeneracy pattern. In the composite calculations the MP2/6-311++G(3df,3pd) coupling constant is applied. The final coupled anharmonic frequencies, LMon _{β_0} , from the traditional and composite methods using CCSD(T)-F12b/aVDZ differ on average less than 10 cm⁻¹. Considering the agreement between the traditional and composite CCSD(T)-F12b/aVDZ frequencies, the composite CCSD(T)-F12/aVTZ frequencies are calculated. The results show a slight blue shift relative the the smaller basis set calculation which agrees with the trend observed in monomer calculations reported in Table 3.1.

Table 3.5: Anharmonic frequencies (cm⁻¹) of the HCl trimer from calculations using the LMon-Hückel method as described in the text.

Mode	CCSD(T)-F12b/aVDZ		MP2/6-311++G(3df,3pd) CCSD(T)-F12b/aVDZ		CCSD(T)-F12b/aVDZ CCSD(T)-F12b/aVTZ	
	LMon	LMon _{β_3}	LMon	LMon _{β_3}	LMon	LMon _{β_2}
ν_1	2791	2771	2784	2760	2778	2753
ν_2	2791	2801	2784	2796	2778	2790
ν_3	2791	2801	2784	2796	2778	2790

Tetramer

Using CCSD(T)-F12b/aVDZ, it is observed that this cluster is characterized by two identically puckered global minima. Connecting the two minima is a planar structure, 30 cm⁻¹ above the global minima. When studied using MP2/6-311++G(3df,3pd) the

same conformations are observed with the planar geometry 14 cm^{-1} above the global minima. Considering how small the difference is between the planar and puckered geometries, the ground state would likely be delocalized across the two global minima, resulting in the experimental observation of an average planar conformation. The effect of a delocalized ground state is approximated by applying the vibrational analyses to the planar structure. The planar CCSD(T)-F12b/aVDZ optimized geometry's HCl bond is 1.289 \AA and hydrogen bond length is 2.392 \AA . The respective distances using MP2/6-311++G(3df,3pd) are 1.284 \AA and 2.354 \AA . Similar relative deviations of the distances are observed between the two electronic structure methods when comparing the puckered conformations.

Table 3.6 contains the harmonic vibrational analyses of the tetramer. First, consider the differences between the two electronic structure methods. The CCSD(T)-F12b/aVDZ full and LMon frequencies are approximately 30 cm^{-1} blue shifted relative to the MP2/6-311++G(3df,3pd). In both methods, full normal-mode frequencies show a $1 : 2 : 1$ degeneracy pattern while the LMon, due to the degenerate monomer subunits, has a four-fold degeneracy. Diagonalizing the simplest Hückel-coupling matrix, given in Equation 3.3, where $\beta_1 = \beta_0$, $\beta_2 = 0$ and $\mathbf{\Omega}$ are the LMon frequencies, the proper $1 : 2 : 1$ splitting is observed in the the LMon_{β_0} . However, the application of the single coupling constant is not sufficient to bring the full and LMon_{β_0} into agreement for either electronic structure calculation. When two constants are applied in Equation 3.3, $\beta_{(1-2)}$, the average difference between the now fully coupled frequencies, LMon_{β_2} and the full normal-mode frequencies are less than 2 cm^{-1} . Examining the effects of the different electronic structure methods on the coupling constants shows minimal difference in the coupling relative to the deviations in the calculated vibrational frequencies.

Table 3.6: Harmonic frequencies (cm⁻¹) of the HCl tetramer from indicated calculations, see text for details.

Mode	MP2/6-311++G(3df,3pd)				CCSD(T)-F12b/aVDZ			
	Full	LMon	LMon _{β₀}	LMon _{β₂}	Full	LMon	LMon _{β₀}	LMon _{β₂}
ν_1	2857	2895	2865	2858	2831	2863	2837	2833
ν_2	2901	2895	2895	2901	2868	2863	2863	2869
ν_3	2901	2895	2895	2901	2868	2863	2863	2869
ν_4	2919	2895	2924	2919	2883	2863	2890	2884
β_0	-14.73				-13.36			
$\beta_{(1-2)}$	-15.28	-6.39			-12.79	-5.22		

The results of anharmonic frequency calculations are reported in Table 3.7. Comparing the traditional and composite CCSD(T)-F12b/aVDZ results for the four-fold degenerate LMon frequency, the results of the two techniques differ by 12 cm⁻¹. After applying the coupling constants the anharmonic LMon_{β₂} frequencies differ on average 18 cm⁻¹. The latter difference is much smaller than the 70 cm⁻¹ difference between the monomer CCSD(T)-F12b/aVDZ and MP2/6-311++G(3df,3pd) frequencies. The composite CCSD(T)-F12b/aVTZ frequencies shows a blue shift of approximately 15 cm⁻¹ relative to the non-composite CCSD(T)-F12b/aVDZ results.

Table 3.7: Anharmonic frequencies (cm⁻¹) of the HCl tetramer from calculations using the LMon-Hückel method as described in the text.

Mode	CCSD(T)-F12b/aVDZ		MP2/6-311++G(3df,3pd)		CCSD(T)-F12b/aVDZ	
	LMon	LMon _{β₃}	LMon	LMon _{β₃}	LMon	LMon _{β₂}
ν_1	2747	2717	2735	2698	2732	2702
ν_2	2747	2753	2735	2742	2732	2738
ν_3	2747	2753	2735	2742	2732	2738
ν_4	2747	2768	2735	2760	2732	2753

Pentamer and Hexamer

For these clusters, geometry optimizations and harmonic analyses were performed using MP2/6-311++G(3df,3pd). The subsequent anharmonic potentials in the composite approach were generated using CCSD(T)-F12b/aVTZ and CCSD(T)-F12b/aVDZ

for the pentamer and hexamer, respectively. The computed frequencies for the pentamer and hexamer are given in Tables 3.8 and 3.9, respectively.

Table 3.8: Harmonic and anharmonic vibrational frequencies (cm^{-1}) of the HCl pentamer.

Mode	Harmonic				Anharmonic	
	MP2/6-311++G(3df,3pd)				MP2/6-311++G(3df,3pd) CCSD(T)-F12b/aVTZ	
	Full	LMon	LMon _{β_0}	LMon _{β_3}	LMon	LMon _{β_3}
ν_1	2854	2898	2862	2854	2724	2680
ν_2	2888	2894	2883	2888	2721	2714
ν_3	2889	2893	2885	2891	2719	2718
ν_4	2912	2890	2916	2912	2716	2736
ν_5	2920	2890	2919	2920	2716	2747
β_0	-15.2					
$\beta_{(1-3)}$	-14.87	-7.36	0.41			

Table 3.9: Harmonic and anharmonic vibrational frequencies (cm^{-1}) of the HCl hexamer.

Mode	Harmonic				Anharmonic	
	MP2/6-311++G(3df,3pd)				MP2/6-311++G(3df,3pd) CCSD(T)-F12b/aVDZ	
	Full	LMon	LMon _{β_0}	LMon _{β_3}	LMon	LMon _{β_3}
ν_1	2935	2917	2937	2940	2759	2781
ν_2	2933	2917	2927	2933	2759	2773
ν_3	2919	2909	2921	2919	2750	2759
ν_4	2902	2909	2901	2902	2750	2742
ν_5	2895	2907	2895	2896	2746	2735
ν_6	2878	2907	2886	2878	2746	2718
β_0	12.56					
$\beta_{(1-3)}$	-12.75	-6.74	5.75			

Starting with the pentamer, the cluster's global minimum geometry has no identical monomer subunits. As a result, the HCl stretch vibrations using the LMon method are not fully degenerate. However, the lack of monomer-monomer coupling still results in LMon frequencies deviating on average 21 cm^{-1} from the full normal-mode frequencies. Applying a single coupling constant using the following matrix

with $\beta_1 = \beta_0$, $\beta_2 = \beta_3 = 0$ and the diagonal, Ω , equal to the LMon frequencies,

$$\begin{bmatrix} \Omega_1 & \beta_1 & \beta_2 & \beta_3 & \beta_1 \\ \beta_1 & \Omega_2 & \beta_1 & \beta_2 & \beta_3 \\ \beta_2 & \beta_1 & \Omega_3 & \beta_1 & \beta_2 \\ \beta_3 & \beta_2 & \beta_1 & \Omega_4 & \beta_1 \\ \beta_1 & \beta_3 & \beta_2 & \beta_1 & \Omega_5 \end{bmatrix}, \quad (3.4)$$

the difference between the LMon _{β_0} and full normal-modes frequencies is reduced to 4 cm⁻¹. Near exact agreement with the normal-mode frequencies is achieved when the LMon frequencies are fully coupled with three separate constants, $\beta_{(1-3)}$, to give the LMon _{β_3} frequencies. Using the MP2/6-311++G(3df,3pd) harmonic results and subsequent CCSD(T)-F12b/aVTZ 1D cuts, the composite CCSD(T)-F12b/aVTZ anharmonic frequencies were determined.

Moving now to the hexamer, the cluster is characterized by three doubly-degenerate LMon frequencies at the global minimum. These frequencies again are in disagreement with the full normal-mode frequencies. The application of the simple Hückel-coupling matrix using,

$$\begin{bmatrix} \Omega_1 & \beta_1 & \beta_2 & \beta_3 & \beta_2 & \beta_1 \\ \beta_1 & \Omega_2 & \beta_1 & \beta_2 & \beta_3 & \beta_2 \\ \beta_2 & \beta_1 & \Omega_3 & \beta_1 & \beta_2 & \beta_3 \\ \beta_3 & \beta_2 & \beta_1 & \Omega_4 & \beta_1 & \beta_2 \\ \beta_2 & \beta_3 & \beta_2 & \beta_1 & \Omega_5 & \beta_1 \\ \beta_1 & \beta_2 & \beta_3 & \beta_2 & \beta_1 & \Omega_6 \end{bmatrix}, \quad (3.5)$$

with $\beta_1 = \beta_0$ and $\beta_2 = \beta_3 = 0$ yields LMon _{β_0} with an average of 3 cm⁻¹ difference from the full normal-mode frequencies. This agreement with only a single coupling constant underlies the similarities of the hexamer geometry to that of the trimer where only a single coupling constant is required. Additional coupling of the LMon frequen-

cies is achieved by applying three separate constants $\beta_{(1-3)}$ to give the $LMon_{\beta_3}$. The final $LMon_{\beta_3}$ frequencies deviate an average of 1 cm^{-1} from the full normal-mode frequencies. Only three coupling constants are required to couple the six $LMon$ modes. If four constants are applied overfitting occurs and the coupled and full normal-mode frequencies no longer agree. Finally, applying the composite technique CCSD(T)-F12b/aVDZ, anharmonic frequencies were determined.

Comparisons with Experiment

The presented anharmonic frequencies represent the simplest approach to computing anharmonic frequencies in a computationally efficient manner. It is likely that the simplicity of the approach results in errors in the calculations. To explore the extent of these errors, the theoretical frequencies are compared to experiments for the trimer, tetramer, pentamer and hexamer. Figure 3.2 shows stick spectra using anharmonic frequencies computed using the highest level composite computations with MP2/6-311++G(3df,3pd) double harmonic intensities, alongside digital renderings of experimentally measured spectra. The theoretical values are all blue-shifted relative to the experiments. Important trends seen experimentally, such as the ordering of prominent cluster peaks, are captured by the present calculations without scaling or semi-empiricism. The theoretical shift varies on average approximately 30 cm^{-1} between clusters. The approximate average peak errors relative to experimental peaks for the trimer, tetramer, pentamer and hexamer are 20 cm^{-1} , 40 cm^{-1} , 50 cm^{-1} and 20 cm^{-1} , respectively.

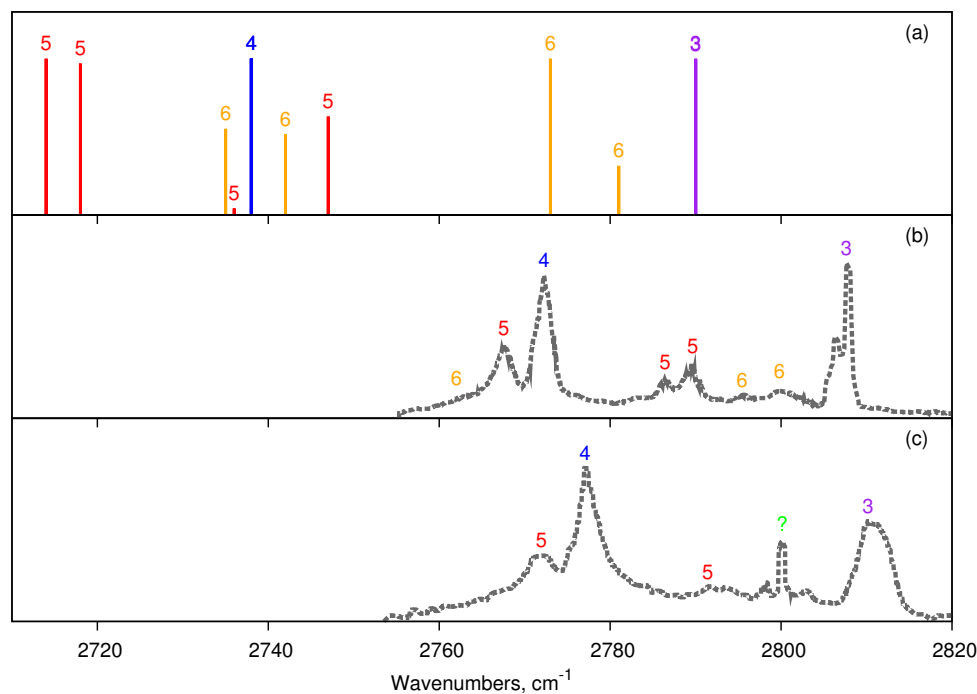


Figure 3.2: Anharmonic stick spectra and relative intensities of the HCl trimer, tetramer, pentamer and hexamer from the current work (a), helium nanodroplets⁷⁰ (b) and ragout-jet FTIR⁷⁶ (c). Additional peak positions of note are trimer: 2810 cm^{-1} and tetramer: $2774 - 2778\text{ cm}^{-1}$.⁵⁹ Dimer peak positions from jet-cooled infrared spectroscopy: 2880 cm^{-1} and 2857 cm^{-1} .⁶⁰

Errors in the calculations which can be traced to the various assumptions that were made. Starting from the application of the composite method, test applications on the trimer and tetramer indicate errors in assuming the ability of MP2/6-311++G(3df,3pd) to match CCSD(T)-F12b/aVTZ geometries result in frequency errors of approximately 12 cm^{-1} . Deviations in MP2/6-311++G(3df,3pd) and CCSD(T)-F12b/aVTZ coupling constants in the tetramer were as large as 3 cm^{-1} , which due to diagonalizing of the coupling matrixes can result in twice the deviation in the frequencies. Combining these errors, the total error of the composite techniques is on the order of 18 cm^{-1} . Considering anharmonic MP2/6-311++G(3df,3pd) calculations of the monomer result in a 70 cm^{-1} error, the composite technique is a substantial improvement. Based on calculations of the monomer, the explicit error in anharmonic CCSD(T)-F12b/aVTZ and CCSD(T)-F12b/aVDZ frequency calculations is 5 cm^{-1}

and 20 cm⁻¹. Additional errors that exist in the *ab initio* methods, such as basis set superposition error, are difficult to measure. The final source of error is the lack of low-frequency mode coupling, i.e. 1D approximation. While it is an extreme case for the effects of low-frequency mode coupling, theoretical benchmark 6D calculations and the 1D calculations of the dimer give an approximate error of 27 cm⁻¹ for the lack of coupling (assuming non-errors in the potential). The final maximum errors in the calculations are predicted to be on the order of 50 cm⁻¹.

3.2.4 SUMMARY AND CONCLUSIONS

In this section a method to compute *on-the-fly* anharmonic vibrational frequencies for molecular clusters, using the local-monomer method is reported. The local-monomer model gives a ideal framework to solve for the molecular vibrations of molecular clusters effectively. In the direct approach, additional improvements to the computation time were made possible by a composite *ab initio* technique. The method was applied successfully to compute anharmonic frequencies for the HCl dimer, trimer, tetramer, pentamer and hexamer. The calculations were capable of computing frequencies a maximum of 50 cm⁻¹ away from experiment.

The computational cost of the direct method demonstrated here is quite small, especially relative to traditional approaches. Consider, the largest cluster studied here, the HCl hexamer. The optimization at each step computes the gradient which, if numerical gradients are employed, requires 60 electronic energy points. The subsequent numerical Hessian calculation to compute harmonic frequencies requires 2593 energies. Given that a single point HCl hexamer CCSD(T)-F12b/aVDZ calculation requires 85 minutes of CPU time on a single compute node, each optimization step would take 85 hours to compute and the full hessian would take over 150 days. Such calculations are too computationally expensive. Using MP2/6-311++G(3df,3pd) the

computation times are reduced substantially, requiring 20 minutes per single point energy, 20 hours per optimization step and 36 days to generate the Hessian. However anharmonic frequencies computed using MP2/6-311++G(3df,3pd) were shown to be quite inaccurate in computations of the HCl monomer. In the LMon calculations of the HCl hexamer the composite technique was used which allows for the speed of MP2/6-311++G(3df,3pd) in the optimization and harmonic analysis along with the accuracy of CCSD(T)-F12b/aVDZ. The most costly part of the calculations was the full harmonic analysis. Computation of the anharmonic frequencies are relatively cheap, requiring only 51 CCSD(T)-F12b/aVDZ energies to study the three doubly-degenerate monomers (17 points each).

Improvements to the LMon results can be achieved by coupling low-frequencies vibrations to HCl stretches. Diatomic clusters, such as $(\text{HCl})_n$, when examined using the LMon method are described by a single high-frequency stretching mode and five low-frequency modes. Calculations fully coupling the five low-frequency modes to the stretch allows for highly accurate studies of the anharmonic vibrational frequencies. Such calculation can only be considered using the LMon approach.

3.3 A NEW MANY-BODY POTENTIAL ENERGY SURFACE FOR HCl CLUSTERS AND ITS APPLICATION TO ANHARMONIC SPECTROSCOPY AND VIBRATION-VIBRATION ENERGY TRANSFER IN THE HCl TRIMER

3.3.1 CONTEXT

Despite the clear success of the LMon approach to study HCl clusters in the previous section, the on-the-fly approach is still limited in its application. In order to study dynamic properties such as pre-dissociation behavior or vibrational energy relaxation and exhaustively large number of potential evaluations are required. This motivated the creation of a rapidly callable many-body potential energy surface to describe HCl

clusters of arbitrary size.

Specifically, the surface is constructed from previous highly accurate, semi-empirical monomer⁷⁸ and dimer⁶³ surfaces and a new high-level *ab initio* three-body potential. The new potential is applied in this section to study the properties of the HCl trimer, (HCl)₃. The stationary points, normal frequencies and D_e values are computed. Anharmonic vibrational energies for the H-Cl stretches of the ring are calculated with explicit 3-mode coupling and local-monomer calculations, which are compared to the previous on-the-fly calculations and experiment. In the latter calculations the Hückel-approach is used. The resulting coupling constant from the Hückel-approach can also be used to model the time-dependent vibration-vibration energy transfer of a single H-Cl stretch excitation to the neighboring monomers of the trimer. This energy transfer is investigated harmonically using quantum and classical approaches and anharmonically using quasi-classical simulations. The accuracy and the applicability of the many-body potential is tested on larger clusters by performing geometry optimizations and normal-mode analyses of the tetramer, pentamer and hexamer. Additional testing is performed by computing the anharmonic H-Cl stretch frequencies for the tetramer using explicit 4-mode coupling calculations and comparing the results with experiment.

3.3.2 (HCL)_N MANY-BODY POTENTIAL ENERGY SURFACE

A one-, two, and three-body potential energy surface for an arbitrary cluster (HCl)_n is given by

$$V_n = \sum_{i=1}^n V_{\text{one-body}}(i) + \sum_{i<j}^n V_{\text{two-body}}(i, j) + \sum_{i<j<k}^n V_{\text{three-body}}(i, j, k), \quad (3.6)$$

where the indices i , j and k denote the collective coordinates of each of the n monomers.

One-Body Potential

The one-body potential potential energy, $V_{\text{one-body}}$, is the spectroscopically accurate potential energy function of Coxon and Hajigeorgiou.⁷⁸ This potential was constructed from least-squares fits to microwave and infrared spectral lines of the isolated HCl monomer in its various isotopic forms.

Two-Body Potential

The intrinsic two-body potential energy, $V_{\text{two-body}}$, is computed using the ES1-EL potential energy surface for the dimer.⁶³ The ES1-EL surface is a semi-empirical surface based on the ES1 potential of Elrod and Saykally⁶⁶ with the addition of an electrostatic interaction potential. The original ES1 potential was generated from least-squares fits to spectroscopic data and guided by an earlier *ab initio* potential energy surface.⁶⁸ The ES1-EL surface used in exact quantum calculations accurately predicts spectroscopic properties including, rotational-vibrational levels,⁸¹ ground state splittings, vibrational predissociation behavior,⁵⁸ and the dissociation energy, D_0 , to within 14 cm^{-1} of the most recent measurement.⁸² The 14 cm^{-1} disagreement is due in part to the original potential being fit to an earlier dissociation energy 8 cm^{-1} different from the most recent measurement.

The intrinsic two-body potential is obtained from the ES1-EL dimer potential using the simple expression

$$V_{\text{two-body}}(i, j) = V_{\text{dimer}}^{\text{ES1-EL}}(i, j) - V_{\text{monomer}}^{\text{ES1-EL}}(i) - V_{\text{monomer}}^{\text{ES1-EL}}(j), \quad (3.7)$$

where the dimer potential is just the full ES1-EL potential and the monomer potential was obtained using a 10th-order polynomial fit in the H-Cl distance of the monomer energy with the two monomers separated to their dissociation limit. This fit was done

for numerical convenience.

Three-Body Potential

The intrinsic three-body HCl potential energy surface, denoted $V_{\text{three-body}}$, was generated from a least-squares fit to 51,466 three-body energies computed using coupled cluster with single, doubles, perturbative triples and explicit correlation (CCSD(T)-F12a) and the augmented correlation consistent double zeta basis set (aug-cc-pVDZ or aVDZ). The energies were calculated using the 2010 MOLPRO quantum chemistry program.⁷⁷ Specifically, $V_{\text{three-body}}$ is determined as

$$V_{\text{three-body}} = V_{\text{trimer}}^{ab \text{ initio}} - \sum_{i < j}^3 V_{\text{dimer}}^{ab \text{ initio}}(i, j) - 3 \sum_{i=1}^3 V_{\text{monomer}}^{ab \text{ initio}}(i), \quad (3.8)$$

where $V_{\text{trimer}}^{ab \text{ initio}}$ is the full HCl trimer energy, $V_{\text{dimer}}^{ab \text{ initio}}(i, j)$ are the energies of the three dimers and $V_{\text{monomer}}^{ab \text{ initio}}(i)$ are the three monomer energies all calculated at the CCSD(T)-F12/aVDZ level of theory.

The fit was performed using a sixth-order polynomial with a permutationally invariant basis in the fifteen variables, $\exp(-r_{ij}/\lambda)$, where r_{ij} is the intermolecular distance between two atoms and λ a range parameter chosen to be 2 bohr.^{3,83,84} These Morse-like variables assure the proper dissociation limits are described by the fit. The potential spans geometries with maximum center-of-mass monomer distances ranging between 4.7 and 30.0 bohr. Geometries in this range are characterized by three-body energies as low as -2482 and as high as 236 cm^{-1} , and full trimer energies as large as $23,450 \text{ cm}^{-1}$. The total three-body root-mean-square (RMS) fitting error is 6 cm^{-1} . A plot of the fitting RMS as a function of three-body energy is given in Figure 3.3.

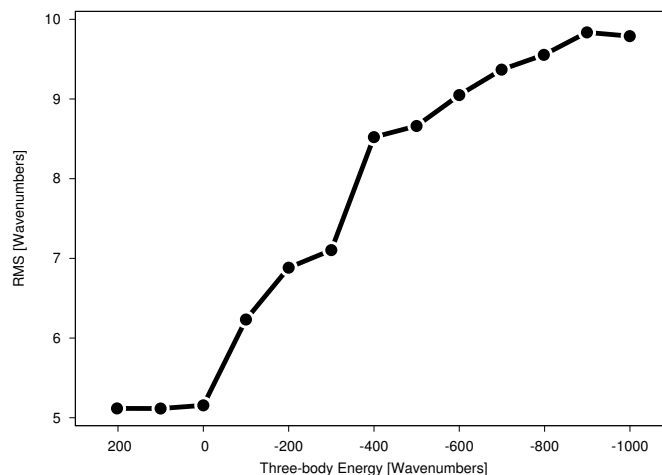


Figure 3.3: Root-mean-square (RMS) of the three-body potential fitting error as a function of the trimer’s three-body energy.

Points for fitting were generated by first performing direct-dynamics trajectories of the HCl trimer using Density Functional Theory B3LYP/aVDZ energies and gradients. Then the energies of a subset of the B3LYP/aVDZ geometries from trajectories were re-evaluated using CCSD(T)-F12/aVDZ. This level of theory was chosen for its speed and accuracy. The effectiveness of the aVDZ versus a larger aug-cc-pVTZ (aVTZ) basis was tested on the HCl trimer. The trimer’s three stationary points were optimized and normal-mode analyses performed using the two levels of theory. The resulting harmonic frequencies differ on average 8 cm^{-1} and their absolute three-body energies differ on average 11 cm^{-1} . These results indicate that the aVDZ energies are of sufficient accuracy for this study.

In addition to the three-body potential energy surface, a fit to the full trimer energies was done as a means of testing the coverage and accuracy of the CCSD(T)-F12/aVDZ-based surface. The full trimer surface was tested using classical molecular dynamics to assure that all relevant configurations were considered for the full trimer potential, as well as the intrinsic three-body potential (which was based on the same geometries). Additionally, the coverage of the fitted full trimer potential was monitored by comparing its ability to accurately reproduce *ab initio* normal-mode fre-

quencies, dissociation energies and stationary point energies. An iterative procedure of fitting, testing and adding points was used until the desired accuracy and span of the surface was achieved. Tests similar to those of the full energy surface were then performed for the three-body potential added to the one- and two-body potentials. Considering, however, that electronic structure properties are not an absolute reference for the results of the many-body potential, the surface was deemed sufficient when the addition of more points resulted in no significant change in the HCl trimer's properties, i.e. stationary points, harmonic frequencies and dissociation energy. It is perhaps worth stating that this hybrid potential is expected to perform better than V_{trimer} , because the one- and two-body components are, by design, of experimental or near-experimental accuracy.

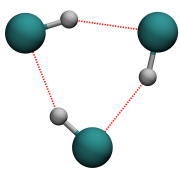
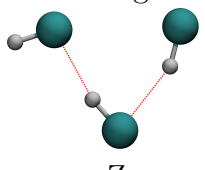
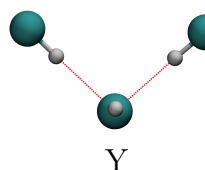
3.3.3 CALCULATIONS OF THE HCL TRIMER

General Properties

Various properties of the HCl trimer were computed using the many-body potential. The three stationary points of the potential, previously reported by Rauk and Armstrong, were located.⁸⁵ Images of these geometries are reported in Table 3.10, along with their relative energies computed from the new potential surface, CCSD(T)-F12a/aVDZ and CCSD(T)-F12a/aVTZ calculations. The D_e values using these methods are also reported in Table 3.10. All of the harmonic frequencies for the three trimer configurations, the dimer and monomer are given in Table 3.11. The behavior of the two- and three-body potentials as the trimer dissociates to three separate monomers or to a dimer and monomer are demonstrated in Figure 3.4. The two-body, three-body and total energies all vary smoothly across the dissociation coordinates. It is clear from the figure that the two-body interaction energy contributes a significant amount more to the total energy than the three-body energy. At

the global minimum the total two-body energy is -2047 cm^{-1} while the three-body interaction energy is -316 cm^{-1} . In addition to the two-body interaction stabilizing the trimer more than the three-body, it also remains “turned on” at longer distances. The two- and three-body interaction potentials each respectively “turn-off” at Cl – Cl distances of ~ 40 and ~ 25 bohr.

Table 3.10: Energies (cm^{-1}) of three low-lying stationary points of the HCl trimer and D_e values.

Structure	Many-Body	CCSD(T)-F12a/aVDZ	CCSD(T)-F12a/aVTZ
 Ring	0	0	0
 Z	737	740	725
 Y	1138	1297	1196
<i>Trimer</i>			
$D_e [3(\text{HCl})]$	2336	2570	2394
$D_e [\text{HCl} + (\text{HCl})_2]$	1643	1813	1678
<i>Dimer</i>			
$D_e [2(\text{HCl})]$	692	756	707

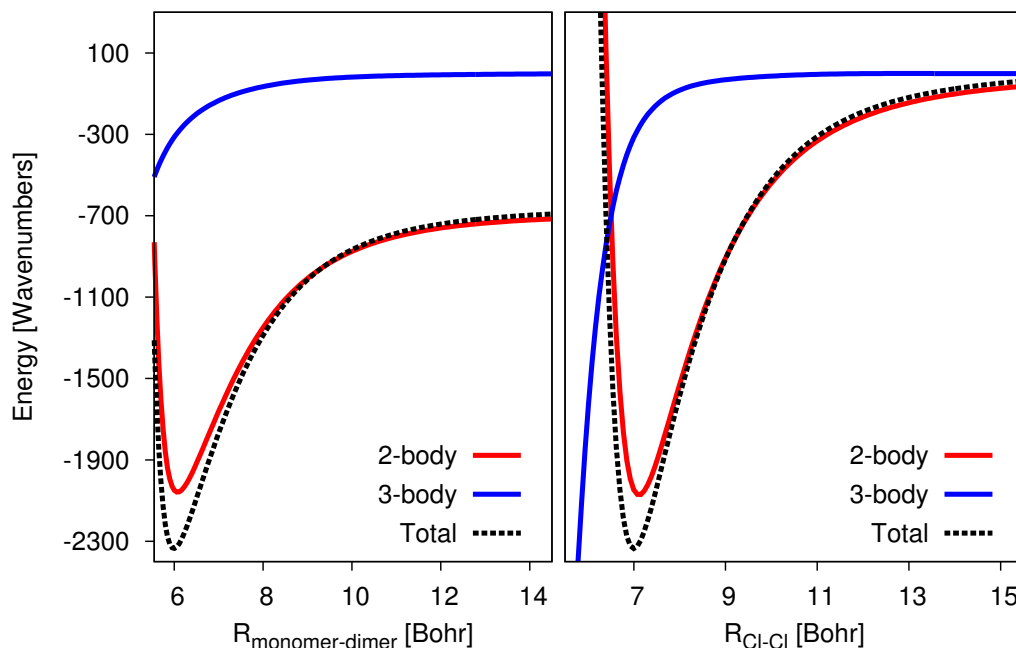


Figure 3.4: Potential energy surface cuts of the two-, three- and many-body (total) potentials of the trimer. The configuration of the minima in each cut is the ring conformation. Cuts were taken (left) as a function of the monomer–dimer center-of-mass distance along a path which leads to dissociation into a dimer and a monomer and (right) as a function of the Cl–Cl distance as the monomers are uniformly compressed and then separated.

Table 3.11: Harmonic frequencies (cm^{-1}) for HCl clusters using the many-body potential surface and *ab initio* calculations at the respective methods minima. The labels ring, Z and Y refer to the three different conformations of the trimer.

PES			CCSD(T)-F12a/aVTZ		
ring	Z	Y	ring	Z	Y
95	27	6	81	39	16
95	68	53	81	78	58
119	89	72	97	93	67
208	106	81	219	118	141
208	138	98	219	186	173
268	178	158	287	200	191
271	242	196	293	251	235
271	247	291	294	265	323
439	389	299	480	428	343
2904	2932	2959	2874	2901	2917
2927	2960	2981	2906	2932	2932
2927	2980	2984	2906	2975	2950

The potential energy of the new many-body surface should be of higher accuracy than the *ab initio* methods (CCSD(T)-F12a/aVTZ) used to perform the previous on-the-fly study of the trimer. Considering the improved accuracy of the new potential, anharmonic fundamental excitation energies for the ring trimer using the aforementioned local-monomer and Hückel-coupling approach are computed. Anharmonic H-Cl stretch frequencies are also computed using explicit 3-mode coupling to further test the assumption that the explicit anharmonic and harmonic stretch couplings are comparable. The program Multimode^{19,20,21} was used to solve for the vibrational energies. The three H-Cl stretching normal-modes were chosen as the coordinates for a vibrational configuration interaction calculation, leaving all other normal coordinates fixed at zero. The calculation was performed with 10 primitive harmonic basis functions for each mode. The maximum quanta for a single mode was tested from 7–10, and these results converged to within 0.01 cm⁻¹. In the calculations only the three stretches were allowed to couple, that is to say, a 3-mode representation was considered. This simplified calculation allows for explicit examination of the anharmonic coupling in terms of just the stretches and allows for direct comparison with the Hückel-coupling calculation. The inclusion of lower frequency modes in the calculation are possible, however, their effects are likely to be small. This assumption is in contrast to vibrational calculations of the HCl dimer where, due to significant tunneling splitting, low frequency modes should be considered for accurate vibrational calculations.^{63,65,59} Tunneling splitting in the trimer has been reported as insignificant.⁸⁶

The H-Cl stretch frequencies from harmonic full normal-mode (Full), local-monomer (LMon) and Hückel-coupling (LMon_{β₀}) calculations, as well as from anharmonic local-monomer, Hückel-coupling and explicit three-mode coupling (3-mode) calculations are reported in Table 3.12. The gas phase experimental value is given for comparison in Table 3.12. As expected, the full harmonic normal-mode frequencies show a 1:2 degen-

eracy pattern whereas the local frequencies are triply degenerate. In the Hückel-model in Equation 3.2, the normal-mode frequencies split analytically according to a singly degenerate $\Omega_0 - \beta_0$ and doubly degenerate $\Omega_0 + 2\beta_0$ values. Considering these analytical functions the local-monomer frequency and the full normal-mode frequencies, the β_0 for the trimer is $\sim 8 \text{ cm}^{-1}$. Application of β_0 to the local-monomer frequency using Equation 3.2 gives the Hückel-coupled frequencies in exact agreement with the full normal frequencies. Moving then to the anharmonic frequency calculations, the degenerate local-monomer anharmonic frequency shifts 90 cm^{-1} relative to the harmonic results. The degenerate anharmonic local-monomer frequencies were coupled using the harmonic β_0 to give the Hückel-coupled anharmonic frequencies with a 1:2 degeneracy pattern. Comparing the latter to the explicit three-mode calculation the differences are quite small, with ν_1 differing by 5 cm^{-1} and the degenerate ν_2 and ν_3 differing by 1 cm^{-1} . The three-mode and Hückel-coupled frequencies for the infrared active modes, ν_2 and ν_3 are within 5 cm^{-1} of the gas phase experimental value.^{71,59} These calculations, using the new potential, are in better agreement with experiment than previous Hückel-coupled CCSD(T)-F12b/aVTZ calculations which reported the infrared active vibration to be 2790 cm^{-1} .⁸⁷

Table 3.12: Vibrational frequencies (cm^{-1}) of the HCl trimer from indicated calculations and experiment, see text for details.

	Harmonic			Anharmonic			Experiment ⁷¹
	Full	LMon	LMon _{β_0}	3-Mode	LMon	LMon _{β_0}	
ν_1	2904	2919	2904	2788	2808	2793	-
ν_2	2927	2919	2927	2814	2808	2815	2810
ν_3	2927	2919	2927	2814	2808	2815	2810
β_0	7.51						

Vibration-Vibration Energy Transfer

The previous subsection demonstrated that in the local-monomer picture the H-Cl stretches of the trimer are triply degenerate. This degeneracy, however, is lifted

by monomer-monomer coupling, which is directly related to the rate of vibration-vibration energy transfer between the monomers. Considering this, the quantum Hückel-model can be used to simulate a wavepacket propagating in a three-state system, where each state is a monomer-centric H-Cl stretch.

The steps taken in the wavepacket calculation are the following.

The eigenstates of the Hückel matrix, ψ_n , are given in terms of the monomer basis, ϕ_n , by

$$\psi_1 = \frac{1}{\sqrt{3}}\phi_1 + \frac{1}{\sqrt{3}}\phi_2 + \frac{1}{\sqrt{3}}\phi_3 \quad (3.9)$$

$$\psi_2 = \frac{1}{\sqrt{2}}\phi_1 - \frac{1}{\sqrt{2}}\phi_3 \quad (3.10)$$

$$\psi_3 = \frac{1}{\sqrt{6}}\phi_1 - \frac{2}{\sqrt{6}}\phi_2 + \frac{1}{\sqrt{6}}\phi_3 \quad (3.11)$$

Inverting, the three localized states are given by,

$$\phi_1 = \frac{1}{\sqrt{3}}\psi_1 + \frac{1}{\sqrt{2}}\psi_2 + \frac{1}{\sqrt{6}}\psi_3 \quad (3.12)$$

$$\phi_2 = \frac{1}{\sqrt{3}}\psi_1 + \frac{\sqrt{2}}{\sqrt{3}}\psi_3 \quad (3.13)$$

$$\phi_3 = \frac{1}{\sqrt{3}}\psi_1 - \frac{2}{\sqrt{2}}\psi_2 + \frac{1}{\sqrt{6}}\psi_3 \quad (3.14)$$

The Hückel eigenstate, ψ_1 corresponds to the $\Omega_0 - \beta_0$ eigenvalue and ψ_2 and ψ_3 correspond to the degenerate $\Omega_0 + 2\beta_0$ eigenvalue. The local eigenstates are all equivalent.

The initial localized wavepacket, Ψ , is chosen as $\Psi(0) = \phi_2$. For the present discussion this is the initially excited H-Cl monomer. As usual, the time-dependence of the wavepacket is given by (with $\hbar = 1$),

$$\Psi(t) = \frac{1}{\sqrt{3}}\psi_1 e^{-iE_1 t} + \frac{\sqrt{2}}{\sqrt{3}}\psi_3 e^{-iE_3 t}, \quad (3.15)$$

where $E_1 = \Omega_0 - \beta_0$ and $E_3 = \Omega_0 + 2\beta_0$. The projection of this wavepacket at some later

time onto the initial wavepacket is denote by $C_{\text{excited}}(t)$ where “excited” is a reminder that this is the vibrationally excited monomer. $C_{\text{excited}}(t)$ is given immediately by

$$C_{\text{excited}}(t) = \frac{1}{\sqrt{3}}\psi_1 e^{-iE_1 t} \left[3 \cos\left(\frac{(E_1 - E_3)t}{2}\right) - i \sin\left(\frac{(E_1 - E_3)t}{2}\right) \right] \quad (3.16)$$

The time-dependent population of the initially excited state is $|C_{\text{excited}}(t)|^2$, and this is given by

$$P_{\text{excited}}(t) = \frac{5}{9} + \frac{4}{9} \cos((E_1 - E_3)t) \quad (3.17)$$

The populations of the initially unexcited states are given by a similar procedure, with the result

$$P_{\text{unexcited}}(t) = \frac{2}{9} - \frac{2}{9} \cos((E_1 - E_3)t) \quad (3.18)$$

Applying this approach, the time-dependent population which result from the wavepacket calculation is given by

$$P_{\text{excited}}(t) = \frac{5}{9} + \frac{4}{9} \cos(3\beta_0 t) \quad (3.19)$$

for the initially excited state and by

$$P_{\text{unexcited}}(t) = \frac{2}{9} - \frac{2}{9} \cos(3\beta_0 t) \quad (3.20)$$

for both initially unexcited states. Note that there are two equivalent “unexcited” populations and that the sum of the three time-dependent probabilities adds to one, as it should.

The time constant, τ , associated with the energy transfer is the time when $P_{\text{excited}}(t)$ first reaches a minimum, $\pi/3\beta$. In the present case $\beta_0 = 7.51 \text{ cm}^{-1}$ and this gives a τ value of 0.73 ps. The population at τ in the original excited state is 1/9 and 4/9 in both of the unexcited states. The average populations of the three states over a

period, 2π , are $5/9$ in the original excited state and $2/9$ in the unexcited states.

Before describing the classical calculations of this energy transfer, it is worth noting that quantum calculations of the splitting of the HCl trimer monomer stretch energies were done previously using the same Hückel (also known as Exciton)-model by Fárnik and Nesbitt.^{59,71} In their calculations the same matrix given in Equation 3.2 was used, except the local frequencies and β_0 and were determined from least-squares fits to experimental infrared peaks of the trimer's isotopologs. Their calculations yielded a local HCl stretching frequency of 2807.90 cm^{-1} (in fortuitously exact agreement with the local-monomer frequency reported in Table 3.12) and a coupling constant of -1.89 cm^{-1} . As these authors noted this coupling constant results in a ring vibrational energy transfer time of $\sim 2.8 \text{ ps}$. The agreement with the present analysis is quite good, with the difference between the experiment and theoretical constants coming from the 5 cm^{-1} error in the fundamental frequency calculation, note above.

Classical simulations of this vibration-vibration energy transfer among the monomer is of interest for purely theoretical reasons, as it offers another example of the difference (or not) between classical and quantum coherence, an issue that was recently illuminated by Miller.⁸⁸ In addition, these simulations are also of specific interest because they are related to the study of the predissociation dynamics of the HCl trimer discussed in the following section. In the current study, the classical molecular dynamics trajectory calculations were performed for the trimer in its ring configuration. Simulations were performed using the Verlet propagator with a 0.25 fs time step on the PES. The chosen time step resulted in an energy drift less than 7 cm^{-1} over the course of the simulations. Each simulation began with a single local-monomer H-Cl stretch of the ring being excited with no additional energy added to the other modes of the ring. The energy of the excitation, 50 cm^{-1} , was kept small to minimize anharmonic effects and in this way to keep the three HCl oscillators on-resonance with each other. The system was initialized using normal-mode sampling. Over 300 trajectories

were simulated, each propagated with a 0.25 fs time step. The local-monomer stretch energies were recorded every 1 fs for each trajectory and the behavior of the three stretches independently average over all 300 trajectories. The classical results are shown in Figure 3.5 along with the results of the wavepacket propagation. As seen in the 3 ps shown, there is virtually identical agreement between the classical and quantum calculations of the time-dependent populations. Thus, on this, and actually longer time scales, the vibration-vibration energy transfer serves as a clear example of agreement between classical and quantum coherence.

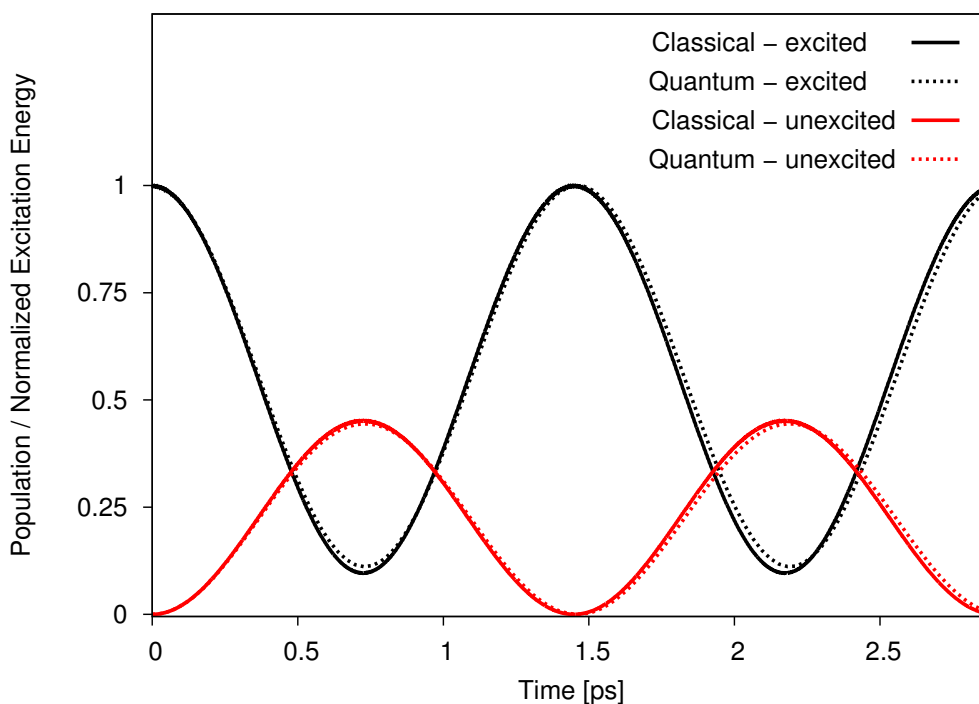


Figure 3.5: Vibration-vibration energy transfer of the local H-Cl stretch in the HCl trimer, computed using the Hückel-model and classical trajectories. The unexcited stretch refers to either of the two unexcited monomer stretches, as their behavior is identical in both models. Additional details provided in the text.

Given that trimer system is treated essentially harmonically, both in the quantum Hückel-model and in the classical model, their agreement is not surprising. In order to consider a perhaps more meaningful representation of the energy transfer an an-

harmonic quasi-classical study of the vibrational relaxation was also performed. This study began with each normal mode initialized with a scaled harmonic energy so that the total ZPE equals the correct one determined from a DMC simulation, which is discussed in the following section, and one local H-Cl stretch mode was given its ZPE plus an additional energy of 2810 cm^{-1} , corresponding to one quantum of excitation. An ensemble of 5,800 quasi-classical trajectories were run and the energies of the local H-Cl stretches monitored as a function of time. The ensemble-averaged HCl monomer excitation energies were considered for roughly 250 ps and fit using a single-exponential, $E = b + ae^{-k_0t}$, and bi-exponential $E = b + a_1e^{-k_1t} + a_2e^{-k_2t}$ functions. The two functions were characterized by small fitting errors, less than 0.007 normalized energy units.

Plots of the vibrational energy relaxation and subsequent stretch relaxation are given in Figure 3.6. The anharmonic transfer process occurs first with a rapid, 0.7 ps, energy transfer (similar to the observed harmonic energy transfer process) where 14% of the initial energy is removed from the initial stretch. Then a subsequent, slower energy exchange occurs, which can be described by either a single exponential with a time constant of 44 ps or a bi-exponential with a fast and slow component of 15 and 77 ps, respectively. Over the course of the 250 ps trajectory, the original excitation energy distributes among the H-Cl stretching modes with virtually no transfer of energy to the intermolecular modes. The harmonic classical recurrences are not observed, very likely because the present simulations are anharmonic and because the inclusion of ZPE motion in the intramolecular modes distorts the perfect planar ring configuration.

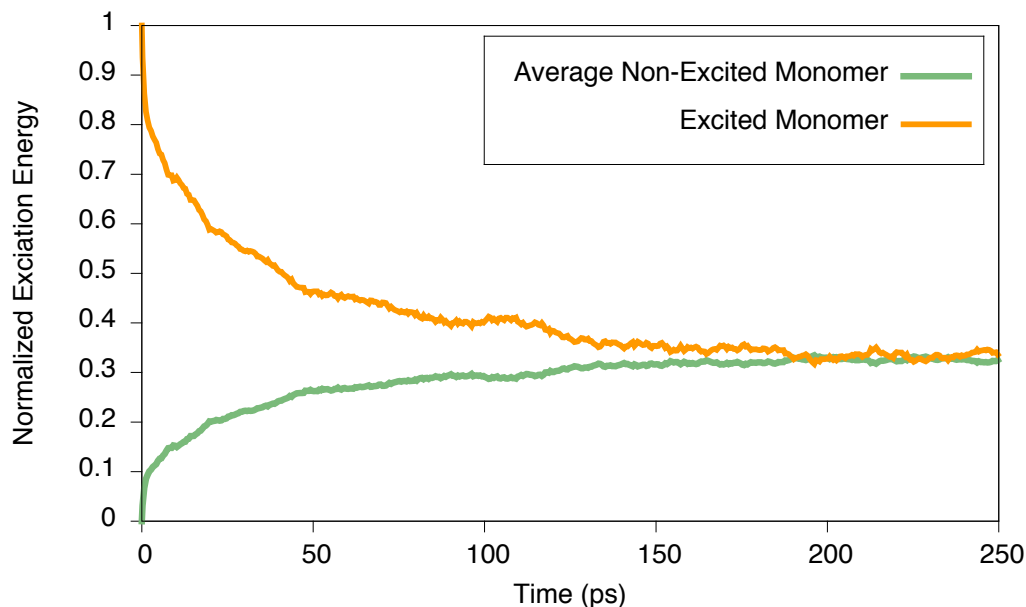


Figure 3.6: Vibration-vibration energy transfer of the local H-Cl stretch in the HCl trimer, computed using quasi-classical trajectories. Additional details provided in the text.

Figure 2.

3.3.4 CALCULATIONS OF LARGER HCl CLUSTERS

The new many-body potential can be applied to systems larger than the trimer with very realistic results. Consider the HCl tetramer, which takes a bent ring configuration at its global minimum. This tightly bound ring represents a conformation where the four-body interaction is likely to be at its highest. Computing the CCSD(T)-F12a/aVDZ interaction energies of the HCl tetramer, the individual contributions are 83% two-body, 15% three-body and 2% four-body. Thus 98% of the interaction energy is captured by the two- and three-body potentials. The effect of the absence of the four-body interaction was examined by performing a geometry optimization of the tetramer on the new potential. The resulting geometry differs from the previously optimized CCSD(T)-F12a/aVDZ geometry in the H-Cl stretches by 0.01 Å, in the hydrogen bond distances by 0.01 Å and in the bending angle by 0.1°. In addition, a Multimode calculation for the four H-Cl stretching modes was performed.

This calculation considered the normal-modes of the four H-Cl stretches with all other normal-modes set to zero, an explicit 4-mode calculation. The details of the basis and integration points were identical to those of the trimer 3-mode study presented above. The vibrational study was conducted for the planar configuration of the tetramer, considering that zero-point energy of the tetramer would likely be enough for the tetramer to freely pass over the 13 cm^{-1} bending barrier (measured on the new potential) resulting in an averaged planar geometry. The planar and bent configurations of the tetramer are in Figure 3.7. The calculation determined the fundamental frequency of the degenerate infrared active mode to be 2789 cm^{-1} , which is within 11 cm^{-1} of the gas phase experimentally reported range, $2774 - 2778 \text{ cm}^{-1}$.^{59,71} The new potential was also used to optimize the global minimum geometries of the HCl pentamer and hexamer clusters, previously computed using MP2/6-311G++(3df,3pd).^{70,89} Comparing the *ab initio* and new potential's optimized pentamers and hexamer geometries are both characterized by a root-mean-square-deviation less than 0.11 \AA . The normal-mode frequencies for the two tetramer conformations, the pentamer and the hexamer are reported in the Table 3.13.

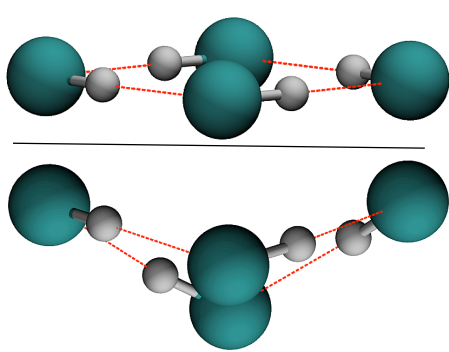


Figure 3.7: Transition state (top) and global minimum (bottom) of the HCl tetramer.

Table 3.13: Harmonic frequencies for (HCl)₄₋₆ clusters using the many-body potential surface at the global minima and (HCl)₄ low lying transition state conformations.

Tetramer-Planar	Tetramer-Bent	Pentamer	Hexamer
2i	8	3	31
33	27	10	34
108	112	13	37
116	114	19	37
116	116	107	48
118	116	113	55
235	228	116	102
248	236	122	103
248	240	124	111
250	240	212	117
274	314	222	124
372	373	229	125
372	373	248	180
500	476	254	194
2891	2894	316	210
2907	2911	378	244
2907	2911	386	249
2918	2921	391	280
-	-	467	316
-	-	2898	329
-	-	2913	346
-	-	2914	377
-	-	2923	405
-	-	2927	441
-	-	-	2906
-	-	-	2912
-	-	-	2919
-	-	-	2923
-	-	-	2932
-	-	-	2938

Although not examined here, the many-body potential can be applied to vibrations other than H-Cl stretches. Measurements of the dimer internal molecular modes (not contain in the fitting data set) that were calculated using ES1-EL⁶³ shows agreement with experimental measurements.^{66,90,81} Considering the latter agreement and the global nature of the new three-body potential, the many-body potential's description of the intermolecular modes of the trimer and larger clusters should also be accurate.

The potential can also be used for the calculation of H-Cl stretch combination bands and overtones. However, the expected accuracy is somewhat uncertain because the experimental data set from which the dimer potential was built does not contain stretching overtones.⁶⁶

3.3.5 SUMMARY AND CONCLUSIONS

In this subsection a new one-, two- and three-body potential energy surface for hydrogen chloride clusters of arbitrary size is presented. The potential was constructed from an experimentally accurate one-body potential, a high quality semi-empirical two-body potential and a new high-level *ab initio* three-body interaction. The latter three-body potential was fit to 52,000 CCSD(T)-F12a/aVDZ three-body energies with an RMS fitting error of 6 cm^{-1} . The new many-body potential was applied to study the HCl trimer. The stationary points, harmonic frequencies of the trimer were all computed. The local-monomer method with Hückel-coupling was used to compute the anharmonic frequencies as well as explicit 3-mode coupled frequencies. Both theoretical methods predicted the infrared active vibration to within 5 cm^{-1} of experiment. The comparison of the 3-mode coupled and local-monomer anharmonic frequencies further validates the use of harmonic Hückel-coupling as a highly effective and justified correction to the local-monomer method. A wavepacket calculation using the Hückel-model was used to consider the rate of vibration-vibration energy transfer in the HCl trimer. A coherent beating between excited and unexcited states was observed. Nearly identical beating was seen in classical dynamic calculations of the energy transfer. Anharmonic quasi-classical studies of the vibration-vibration energy transfer revealed a very different transfer processes occurs between the HCl monomers. Finally, the applicability of the new potential to clusters larger than the trimer is demonstrated. Geometries for the tetramer, pentamer and hexamer were computed in agreement with *ab initio* studies. In addition, an anharmonic 4-mode

coupled anharmonic frequency calculations were performed for the tetramer in good agreement with experiment.

3.4 EXPERIMENT AND THEORY ELUCIDATE THE MULTICHANNEL PREDISSOCIATION DYNAMICS OF THE HCl TRIMER: BREAKING UP IS HARD TO DO

3.4.1 CONTEXT

The hydrogen bond (H-bond) is the most pervasive bond in nature. It holds the strands of DNA together⁹¹ as well as provide the glue for water.⁹² Not surprisingly all aspects of this bond, including its formation and breakup, have been of ongoing interest to both theoreticians and experimentalists for over a century.^{93,94,95,96} This desire to understand H-bonding has prompted the study of several paradigm systems for which the energetics and dynamics can be interrogated exhaustively, with the bulk of the work focused on dimers of water and other small hydride molecules.^{97,98,99,58,100,65,101,102,103,104} Recently, impressive progress has been made towards detailed studies of prototypical H-bonded systems larger than dimers.^{105,106,107,41,108,76,70,109,59} These studies stand to reveal much more about the dissociation dynamics of H-bonded networks and the cooperative nature of these interactions.

The hydrogen chloride trimer, $(\text{HCl})_3$, as discussed in the previous sections is an ideal prototype for such detailed studies.^{76,70,59,71,75,86,72,85,73,74} The stretch fundamental frequency of the trimer has been measured with high-resolution spectroscopy in the gas phase at 2810 cm^{-1} ,^{59,71} which is enough excitation energy result in dissociation via one of two channels. Breaking two hydrogen bonds leads to dimer + monomer fragments (Channel I), whereas breaking of three hydrogen bonds generates directly three monomers (Channel II).

In this section the theoretical contribution to a combined experimental and theoretical study are presented. The experimental work studied the vibrational predis-

socialiton of the HCl trimer in a pulsed supersonic molecular beam after a pulsed IR excitation of the HCl stretch at 2810 cm⁻¹. The dissociated rotationally excited HCl fragments were ionized by (2+1) resonance-enhanced multiphoton ionization (REMPI) and detected using time-of-flight (TOF) mass spectrometry and velocity map imaging (VMI).^{110,102,103,99,101,97} These experiments resulted in the measurement of correlated product state distributions. The molecular dissociation energies, D_0 , of both channels I and II were computed based on the measured distributions and the conservation of system energy

$$D_0(\text{Channel I}) = E_{\text{rot}}(\text{monomer}) + E_{\text{vib,rot}}(\text{dimer}) + E_{\text{T}} - h\nu_{\text{IR}} - E_{\text{internal}}(\text{trimer}), \quad (3.21)$$

$$D_0(\text{Channel II}) = \sum_{i=1}^3 E_{\text{rot}}(\text{monomer}_i) + E_{\text{T}} - h\nu_{\text{IR}} - E_{\text{internal}}(\text{trimer}), \quad (3.22)$$

where $E_{\text{int}}(\text{trimer})$ is the internal energy of the trimer prior to excitation, $h\nu_{\text{IR}}$ is the 2809 cm⁻¹ used for the HCl excitation, $E_{\text{rot}}(\text{monomer})$ is the rotational energy of the single HCl monomer or i^{th} HCl monomer, $E_{\text{vib,rot}}(\text{dimer})$ is the rovibrational energy of the dimer cofragment, and E_{T} is the c.m. translational energy. The study is the first experimental study of its kind to follow the evolution of an H-bonded trimer from initial vibrational excitation to fragment internal and translational energy distributions.

3.4.2 THEORETICAL METHODS FOR THE STUDY OF (HCL)₃ PREDISSOCIATION

The previously constructed (HCl)₃ many-body potential energy surface was used to study trimer's predissociation. As stated previously, in the context of the trimer the many-body representation is complete, characterizing the three one-body interactions, the three two-body interactions and the one three-body interaction. Dissociation energies were calculated using the D_e values of the PES and also complete basis set (CBS) calculations, along with numerically exact zero-point energies computed using

DMC simulations^{29,30} for the trimer and dimer and discrete variable calculations²³ for the monomer. The dynamics studies were performed using quasi-classical trajectories.

The DMC simulations were performed for the HCl dimer and trimer. Five simulations were performed for each system using 30000 “walkers,” an imaginary time step of 2.5 atomic units, an α value of 0.4, an equilibration period of 3000 steps and a propagation period of 39400 steps. A trajectory demonstrating the convergence of the simulations for the trimer is given in Figure 3.8. The dimer and trimer ZPEs were taken to be the average of their five simulations and their respective standard deviations taken to be the statistical uncertainty associated with their respective simulations. Additional errors associated with the three-body potential were considered in the DMC calculations by comparing the extent with which the three-body energy affected the ZPE by computing DMC simulations with just the one- and two-body potentials and by comparing anharmonic HCl monomer ZPE computed using same ab initio method as the three-body potential and the Coxon and Hajigeorgiou⁷⁸ monomer potential’s ZPE. The error in the ZPE associated with the three-body potential was found to be $\sim 1 \text{ cm}^{-1}$. The ZPE for the HCl monomer was computed using a DVR.

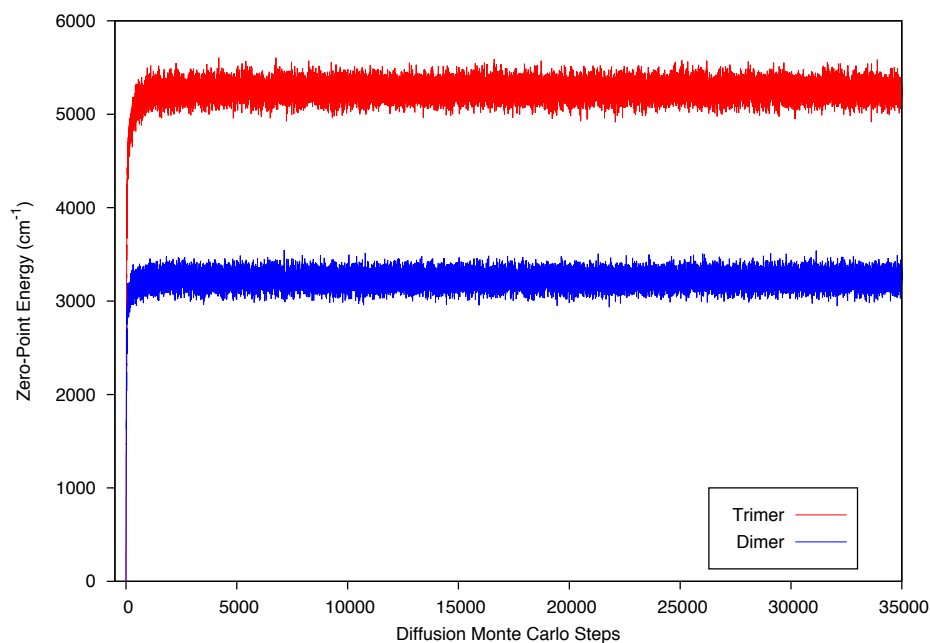


Figure 3.8: Diffusion Monte Carlo simulation of the HCl dimer (blue) and trimer (red) as a function of imaginary time step.

Quasi-classical trajectories were propagated to obtain the dissociation dynamics of the HCl trimer system. Simulations were performed using the Verlet propagator with a 0.25 fs time step on the PES. The chosen time step resulted in an energy drift less than 7 cm^{-1} over the course of the simulations. Every trajectory was performed with zero-point energy (ZPE) and additional vibrational excitation energy of one local-monomer stretch; the details of this excitation will be discussed as the calculations are introduced. The dissociation of the trimer was monitored with respect to the three monomer s.c.m. distances. If all three distances were greater than 6.5 \AA , then dissociation to three monomers occurred, but if one distance was less than 6.5 \AA , then the trimer was labeled as dissociating to a dimer and monomer. This distance is sufficiently large for the intermolecular interaction to be negligible. Trajectories giving any fragment (monomer or dimer) with less than the proper ZPE were discarded.

The predissociation dynamics of the trimer were first explored by initializing the QCT at global minimum with ZPE scaled to the anharmonic value and one extra quanta of stretch energy, 2810 cm^{-1} . A set of 20 trajectories, each simulated for over

20 ns, were performed. Three of the trajectories dissociated to a monomer and a dimer, but only one with at least ZPE in the products. The remainder of the trajectories failed to dissociate. Additional shorter timescale trajectories were performed to collect dissociative “outlier” trajectories. This approach yielded an additional six trajectories that dissociated to a monomer and a dimer. The length that the simulations needed to be propagated to observe cluster dissociation is consistent with the nanosecond lifetime indicated by experimental linewidths.^{59,71}

Based on the dissociative results a “critical” open-chain configuration was located from which dissociation occurred. This is the Z configuration shown in Table 3.10. A set of trajectories starting from this critical geometry were performed to study the energy distributions of the dissociated products. These trajectories were initiated with scaled ZPE (using the same scaling factor applied at the minima) and the remaining relaxed fundamental excitation energy microcanonically distributed among the nine low frequency modes. A total of 100,000 trajectories were performed in this manner, each propagated for 10 ps. In total 20,176 trajectories dissociated to a monomer and a dimer.

A final series of trajectories involving the dissociation of “hot” dimers was performed. These trajectories were initiated from the dimer global minimum with the goal of examining the energy distributions of the two monomers. Scaled ZPE was added to the dimer at its global minimum using the scaling factor derived from DMC simulations. Excitation energy of $1,100\text{ cm}^{-1}$ was added microcanonically to the low-frequency vibrations of the dimer. This energy coincides with an internal dimer energy which would allow two monomers to dissociate both with $J'' = 5$. In total 85,000 trajectories were performed with 2,882 dissociating with at least ZPE in the two monomers.

3.4.3 GROUND STATE PROPERTIES AND DISSOCIATION ENERGIES OF $(\text{HCl})_{2-3}$

Isosurface representations of the HCl dimer and trimer are given in Figure 3.9. The dimer ground state wavefunction is highly delocalized across the two equivalent global minima resulting in two banana shaped proton distributions. Relative to the dimer, the trimer is much more localized with the hydrogen bonds remaining unbroken in the ground state. The protons are still delocalized about the global minimum geometry forming three mushroom shaped proton distributions. The anharmonic ZPEs from the DMC (and DVR) for the monomer, dimer and trimer are 1483, 3235 ± 1 and $5260 \pm 1 \text{ cm}^{-1}$, respectively. Relative to harmonic ZPEs the anharmonic values are red-shifted 14 cm^{-1} in the monomer, 81 cm^{-1} in the dimer and 106 cm^{-1} in the trimer.

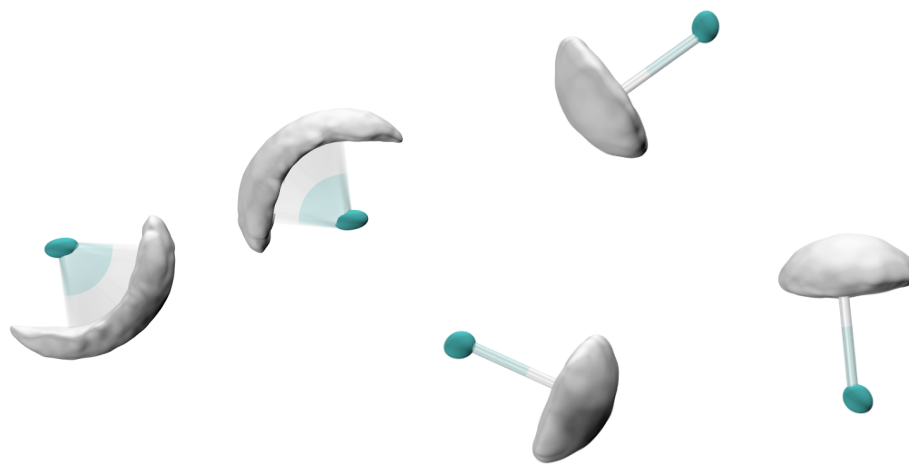


Figure 3.9: Isosurface representations of the HCl dimer (left) and trimer (right) ground state wavefunctions.

Complete basis set (CBS) extrapolations were performed to determine highly accurate D_e values for the HCl trimer system. The results of these calculations should be considered benchmark values for the dissociation energy. The extrapolated energies were computed at CCSD(T)/aug-cc-pVTZ optimized geometries using CCSD(T)/aug-cc-pVXZ where X refers to the cardinal number in the basis set. The three variable

extrapolation fitting function, $E(X) = E_{\text{CBS}} + Ae^{-XB}$, was used, where A and B are fitting parameters and X=2, 3, 4 and 5, i.e., aug-cc-pVDZ, aug-cc-pVTZ, aug-cc-pVQZ and aug-cc-pV5Z. The D_e values from the many-body potential and CBS calculations are given in Table 3.14.

Table 3.14: HCl trimer and dimer D_e values (cm^{-1}).

System	D_e [PES]	D_e [CBS]
$(\text{HCl})_3 \rightarrow 3(\text{HCl})$	2336 ± 45	2373
$(\text{HCl})_3 \rightarrow \text{HCl} + (\text{HCl})_2$	1643 ± 31	1675
$(\text{HCl})_2 \rightarrow 2(\text{HCl})$	692 ± 14	699

The true dissociation energies, D_0 , which includes the differences between the electronic dissociation, D_e , and the respective zero-point energies for the trimer and dimer are listed in Table 3.15. The experimental results reported in Table 3.15 are taken from VMI experiments. Two sets of theoretical dissociation energies were computed using the DMC ZPE and D_e values obtained with the many-body potential (PES) and also from complete basis set calculations (CBS). Both the PES and CBS dissociation energies are in excellent agreement with the experimental measurements. The more accurate CBS values deviate a maximum of 10 cm^{-1} when the theoretical and experimental error bars are considered. While the D_e values of the PES were reported in the previous subsection for the trimer but an estimate of their error in those measurements is made here. Beginning with the two-body interaction, the 14 cm^{-1} difference from the experimental D_0 and the ES1-EL potential is taken to be the PES error associated with breaking a hydrogen bond between two monomers. Due to this error the two-body error of the D_e for the dimer is $\pm 14 \text{ cm}^{-1}$ for each H-bond broken. The three-body error in the D_e value can be taken from the difference between the three-body interaction energy computed using the many-body potential and complete basis set calculation, $\pm 3 \text{ cm}^{-1}$. The experimental trimer dissociation energies obtained for Channels I and II and the dimer's dissociation energy of 439 cm^{-1} ⁸² place the cooperative (non-additive) contribution at $\sim 250 \text{ cm}^{-1}$, in

good agreement with the theoretical values of $\sim 251 \text{ cm}^{-1}$ and $\sim 271 \text{ cm}^{-1}$, obtained for the two theoretical methods.

Table 3.15: HCl trimer and dimer D_0 values (cm^{-1}).

System	D_0 [PES]	D_0 [CBS]	Experiment
$(\text{HCl})_3 \rightarrow 3(\text{HCl})$	1526 ± 46	1564 ± 1	1545 ± 10
$(\text{HCl})_3 \rightarrow \text{HCl} + (\text{HCl})_2$	1102 ± 33	1133 ± 2	1142 ± 20
$(\text{HCl})_2 \rightarrow 2(\text{HCl})$	425 ± 29	431 ± 1	439 ± 1 ⁸²

3.4.4 ROTATIONAL AND TRANSLATION DISTRIBUTIONS OF (HCL)₃ FRAGMENTS

Two different VP channels are possible following excitation of the trimer's H-Cl stretch fundamental; Channel I (monomer + dimer) has an excess energy of $\sim 1700 \text{ cm}^{-1}$ [$2809 - (\sim 1100 \text{ cm}^{-1})$] and Channel II (three monomers) restricts the excess energy to $\sim 1300 \text{ cm}^{-1}$ [$2809 - (\sim 1500 \text{ cm}^{-1})$]. The corresponding maximum allowed J'' values for HCl from these channels are 12 and 10, respectively. Figure 3.10 presents a comparison of these experimental populations and the relative populations computed by QCT calculations. Both theory and experiment show that the rotational populations decrease sharply for $J'' \geq 5$, and the population of $J''=11$ is only $\sim 5\%$ of the population of $J''=5$. Since $J''=11$ is the only level that is associated solely with Channel I, it has special importance in image analysis, as demonstrated below. According to the calculations the HCl rotational state distribution corresponding to Channel I is broad, encompassing all the allowed states and peaking at $J''=4$.

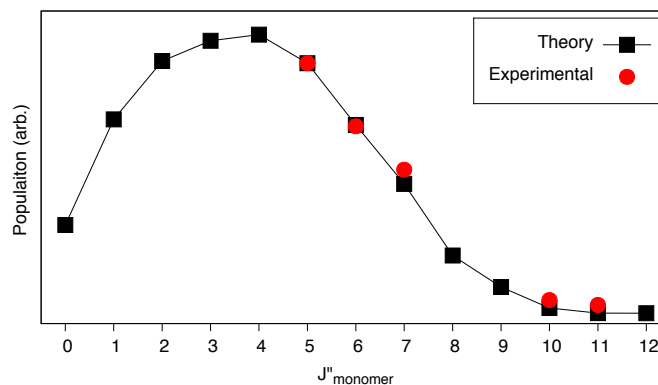


Figure 3.10: Comparison of theoretical and available experimental HCl monomer rotational populations.

Figure 3.11 displays the experimental and theoretical c.m. E_T distributions from HCl monomer fragments in different J'' levels, where the experimental results characterize all HCl fragments, regardless of the dissociation process, and the theoretical results characterize only monomers that dissociate from Channel I. While the experimental and theoretical distributions match quite well for $J''=10$, they deviate progressively more as the monitored J'' level decreases, with the greatest mismatch for $J''=5$.

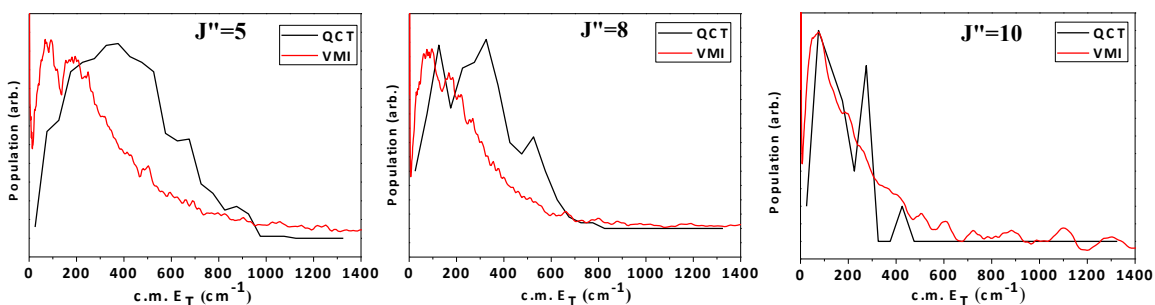


Figure 3.11: Comparison of c.m. E_T distributions obtained by detecting HCl fragment (red curve) in $J''=5$, 8 and 10. Black curves are the corresponding distributions obtained from QCT calculation for Channel I.

The cause for this mismatch becomes clear when considering the possible internal energies of the dimer cofragments associated with each monitored HCl(J'') monomer fragment. The dimer internal energy distribution is given in Figure 3.12. The inset of Figure 3.12 displays the percentage of monomers that could possibly dissociate at a

given J'' . When the internally “hot” dimers dissociate, they produce monomers with a broad E_T distribution extending to very low translational energies. The dissociation of these “hot” dimer fragments, $[(\text{HCl})_2]^{**}$, into two HCl monomers is referred to as Channel Ia. The final velocity of the $\text{HCl}(J'')$ monomer generated via this pathway depends on the velocities of dimers generated in Channel I and the velocity of HCl generated via Channel Ia.

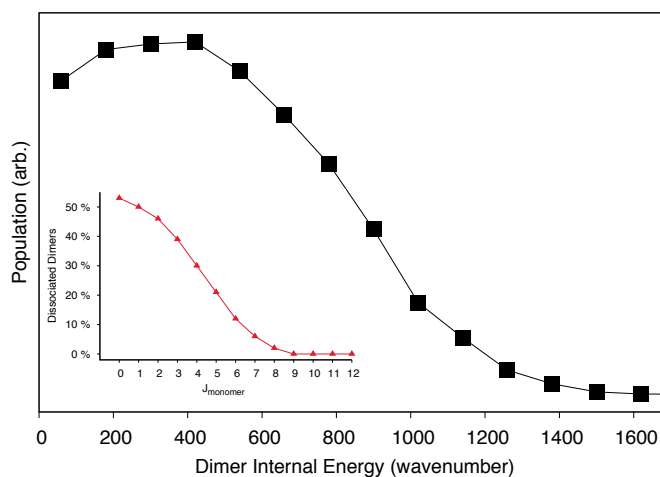


Figure 3.12: Internal energy distribution of dissociated dimer relative to its anharmonic ZPE (black). The inset (red) contains a plot of the percentages of monomers which can possibly dissociate from the dimer with a given J'' , assuming that one monomer dissociates with $J'' = 0$ and zero translational energy.

The limited amount of internal energy in the dimer results in relatively lower translational energies for the “hot” dimer fragments. This is supported by the results of the final series of QCT trajectories performed on the HCl dimer. The translational energy distribution for $J'' = 5$ compared with the distribution of the monomer dissociated directly from the trimer is shown in Figure 3.13 where the dimer’s monomer distribution is clearly much colder than the trimer’s distribution.

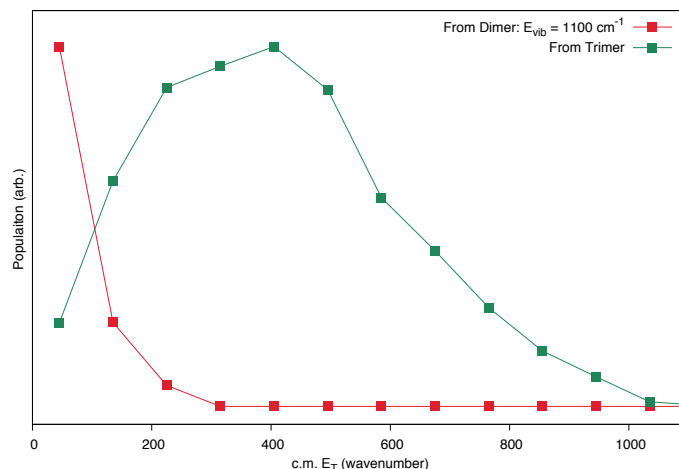


Figure 3.13: HCl monomer translational distribution for $J'' = 5$ with the monomer dissociating from an internally “hot” dimer (red) and vibrationally excited trimer via the monomer + dimer channel (green).

3.4.5 DISSOCIATION MECHANISM OF $(\text{HCL})_3$

The QCT calculations show that the rate-limiting step in the VP is the transfer of H-Cl stretch excitation to the intermolecular modes of the trimer. This is in agreement with Farnik and Nesbitt, who suggested based on their spectroscopic work that V-V transfer is followed by energy transfer to low frequency modes and then ring opening.^{59,71} Indeed, simulations find that once the H-Cl stretch relaxes, one H-bond can break and the ring can transition to an open chain configuration, 737 cm^{-1} higher in energy. This conformer is stable enough to allow energy to localize and break a second H-bond, forming a monomer and dimer (Channel I). The minimum energy path to this configuration is demonstrated in Figure 3.14.

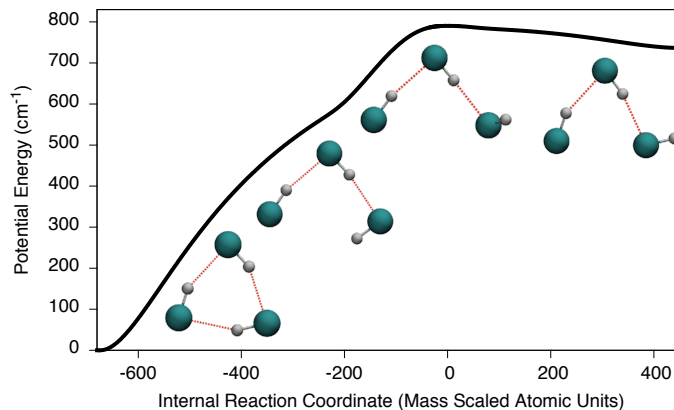


Figure 3.14: Minimum energy path from trimer to open-chain configuration.

The trajectory calculations show that even after reaching the critical configuration of the open-chain trimer, the breaking off of an HCl monomer is not instantaneous; it involves many vibrational motions, with H-bonds breaking and reforming until finally an HCl monomer breaks off. Similar behavior has been found before in QCT calculations of the water trimer.¹⁰³ This may indicate a common mechanism of breakup of cyclic trimers. The measured rotational energy distribution of the HCl monomer and the c.m. E_T distributions correlated with specific $\text{HCl}(J'')$ fragment states are quite broad, in accordance with the experimental observations.

3.4.6 SUMMARY AND CONCLUSIONS

The combination of experiment and theory were able to yield a wealth of information and accurate results on the detailed dissociation mechanism of the ring HCl trimer. The calculations demonstrate that it is now possible to describe properties of clusters such as D_0 and cooperative three-body interactions with excellent accuracy. The successful description of the multi-channel breakup of the benchmark HCl trimer is important also in predicting the success of calculations of dissociation dynamics of larger H-bonded networks for which experiments are becoming progressively more difficult. The excellent agreement between theory and experiment demonstrated here

attests to the ability of such calculations to provide reliable values of properties and mechanisms for larger H-bonded clusters.

4

Mixed $(\text{HCl})_n$ and $(\text{H}_2\text{O})_m$ Clusters

4.1 OVERVIEW

The molecular properties of heterogenous clusters present a challenging and important system for rigorous study. These systems can often behave significantly differently than their homogenous precursors. One such system that is of both fundamental and practical interest are clusters of water and hydrogen chloride. A reasonable assumption upon the mention of a system such as this is the general chemistry reaction $\text{HCl}(\text{aq}) + \text{H}_2\text{O}(\text{aq}) \rightarrow \text{H}_3\text{O}^+(\text{aq}) + \text{Cl}^-(\text{aq})$. This equation for acid formation however does not apply at the nanocluster limit. The question of when such a transition occurs remains a hotly debated question. In order to understand the transition, a detailed

understanding of the nanoclusters that are stable as molecular HCl and H_2O must be obtained. These clusters provide a challenging system for investigating the effects of heterogeneity in molecular clusters. In the HCl cluster study in Chapter 3 there was a 1 : 1 ratio of hydrogen bond donors and acceptors. The heterogeneous system has, for every additional heterogeneous pair, a ratio of 3 : 2 donors to acceptors. This uneven ratio allows for a very different set of molecular configurations and behaviors than in the homogeneous case of either H_2O or HCl.

This chapter is divided into two sections as follows. The first presents the construction of a full-body potential energy surface for the HCl- H_2O dimer. The potential is used to resolve a debated aspect of the ground state behavior, specifically whether the experimentally observed conformation is planar or bent. In addition, a benchmark value for the dimer dissociation into two fragments is computed. The second section builds off the HCl- H_2O dimer potential as well as the $(\text{HCl})_n$ potential presented in Chapter 3 to create a many-body $(\text{HCl})_n(\text{H}_2\text{O})_m$ potential. Vibrational ground state properties of the cluster are detailed for the mixed dimer, trimers and tetramers along with their respective fundamental stretch excitations.

4.2 A NEW AB INITIO POTENTIAL ENERGY SURFACE FOR HCl- H_2O , DIFFUSION MONTE CARLO CALCULATIONS OF D_0 AND A DELOCALIZED ZERO-POINT WAVEFUNCTION

4.2.1 CONTEXT

Complexes of HCl with H_2O have been the focus of recent experimental^{98,97,111,112,40,41} and theoretical^{113,114,115,116,117} studies. The high interest in these complexes is due, in part, to their impact on atmospheric chemistry, specifically their role in ozone depletion.^{118,119,120,121} Recent studies have focused on the static and dynamic behaviors of small HCl- $(\text{H}_2\text{O})_n$ clusters to gain knowledge of their interactions at an atomic level. These clusters remain a challenge particularly with respect to the

movement from molecular $\text{HCl}(\text{H}_2\text{O})_n$ to the ionized $\text{Cl}^-(\text{H}_2\text{O})_{n-1}\text{H}_3\text{O}^+$ clusters. Several theoretical studies have pointed to ionization at a four-water monomer cluster.^{122,123,124,125,126,127,128} However, recent high level quantum mechanical studies predict the coexistence of non-ionized clusters at the four monomer limit.^{114,117} The complexity of the problem is even more apparent from the lack of experimental consensus on the identification of the ionized cluster.^{129,40} A building block to understanding the clusters at the four-water limit and beyond is a detailed knowledge of even smaller $\text{HCl}\text{-H}_2\text{O}$ clusters, the first of which is the $\text{HCl}\text{-H}_2\text{O}$ dimer. The dimer, which is of great interest in its own right, has been firmly identified using a variety of techniques including velocity-map imaging with resonance-enhanced multiphoton ionization,^{98,97} infrared studies in liquid helium,^{55,41,40,70} microwave spectroscopy,^{130,131} ragout-jet FTIR^{132,109} cavity ringdown spectroscopy¹³³ and infrared-matrix isolation spectroscopy.^{134,135,136,137,138} Of these studies refs. 1 and 2 have reported studies of the molecular dissociation of the dimer. In those studies the fragments translational energy distributions were measured, allowing for the determination of the dimer's dissociation energy (D_0), which was reported to be $1334 \pm 10 \text{ cm}^{-1}$.⁹⁸ Previous theoretical studies^{124,139,140,127} have reported values of D_0 ; at the highest level of theory, CCSD/aug-cc-pVDZ+,¹²⁷ with an approximate anharmonic zero-point energy (ZPE) calculated from MP2/aug-cc-pVDZ+, a value of 1189 cm^{-1} was reported. This is not in good agreement with experiment.

Previous theoretical studies of the dimer indicate that its potential surface is characterized by three stationary points all consisting of the HCl donating a hydrogen bond to the H_2O molecule.^{126,125,139,141,140,124,127} The non-planar structure global minimum with labeled coordinates is shown in Figure 4.1. It is clear from examining the structure that there exists two equivalent non-planar minima with a planar C_{2v} saddle-point connecting them through a bend of the θ_2 angle and a slight bend in the θ_3 . Estimates of this double well barrier height vary with different levels of the-

ory, with the previous highest-level CCSD(T)/6-311++G(2d,2p) calculation giving 85 cm^{-1} .¹⁴¹

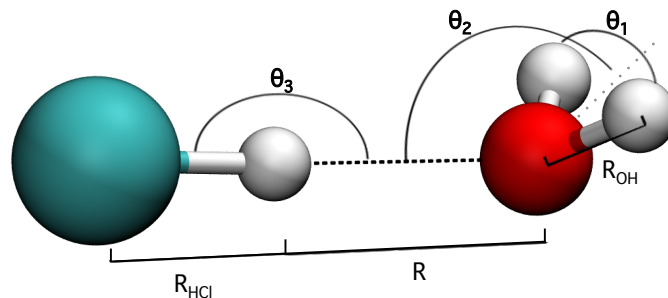


Figure 4.1: Geometry of the global minimum with labeled coordinates.

Given how low the saddle-point barrier is, the question of what experimental configuration is observed has been of interest because of the likely possibility for the ZPE of the system to lie close to the barrier and this might result in a delocalized wavefunction spanning the double well potential. The dimer ZPE from harmonic vibrational analysis using the optimized global minimum geometry was found to exist above the isomerization barrier for MP2, MP3, MP4 and CCSD(T) with a 6-311++G(2d,2p) basis set.¹⁴¹ In the same study an MP3-level 1-D potential with the aforementioned basis as a function of the bending angle with all other modes fixed at their optimized configuration was fit to a polynomial and used to obtain a ZPE 4 cm^{-1} below the inversion barrier. From this, the authors suggested the possibility of an average geometry of C_{2v} structure. Delocalized wavefunctions of this type have been reported previously in full dimensional calculations in systems like H_5^+ ,^{142,143} H_3O_2 ,¹⁴⁴ and CH_5^+ .⁸³

The nature of the ground state configuration of HCl-H₂O has been inferred by examining experimentally fit rotational coefficients and theoretical models. Kisiel et al.¹³⁰ reported a 1-D potential cut along θ_2 at the MP2/aug-cc-pVDZ level of theory assuming θ_3 to be 180 deg. The potential was fit to a quartic-quadratic potential and the ZPE determined from the analytical double well solutions to be just below the

inversion barrier. A calculated expectation value of the ground state angle was reported to be ~ 146 deg. In these studies, statistically better fits to rotational spectra were achieved by using this non-planar angle. From their study an estimate of the A rotational constant of 12 cm^{-1} was made. However, later Ragout-jet FTIR spectroscopy¹³² and infrared laser spectroscopy in helium droplets¹⁴⁵ both estimated the A-constant to be $14 - 15 \text{ cm}^{-1}$.

Here a new, full (nine)-dimensional potential energy surface (PES) is reported to describe the HCl-H₂O system. The full-dimensional potential is used to perform Diffusion Monte Carlo (DMC) simulations in order to compute accurately the ground state wavefunction of the dimer and obtain accurate ground state energies for the dimer and fragments. The DMC results are used alongside complete basis set limit dissociation energy calculations to obtain D_0 values for the dimer. Analogous calculations are reported for the fully deuterated isotopologue of the dimer.

4.2.2 THEORETICAL METHODS FOR THE STUDY OF THE $(\text{HCL})(\text{H}_2\text{O})$

The PES is a fit to 44637 configurations and energies obtained with CCSD(T)-F12b,¹² using the aug-cc-pVTZ basis set. All energies were calculated using the 2010 MOLPRO quantum chemistry program⁷⁷ The energies were fit by representing the PES in a basis of permutationally invariant polynomials in Morse-like variables, $\exp(-r_{ij}/\lambda)$, where r_{ij} is the intermolecular distance between two atoms and λ a range parameter chosen to be 2 a.u.³ The maximum total polynomial order of the fit is six. The surface is characterized by a total RMS fitting error of 24 cm^{-1} . A plot of the energy as a function of the number of points and the respective RMS fitting error is shown for a portion of the fitting data in Figure 4.2. A separate set of 615 geometries ranging from 0 to 9000 cm^{-1} above the global minimum that were not included in the fitting set was used to further test the surface. In the test set, the RMS of geometries with energies greater than 3500 cm^{-1} increased as a function of the energy to a maximum

RMS of 80 cm^{-1} at 9000 cm^{-1} . Given that the purpose of the surface is an accurate description of the dissociation of the complex as well as a future goal of the IR spectroscopy of experimentally relevant states, the present PES is adequate for these purposes. The geometries, reported in Table 4.1, and harmonic frequencies, reported in Table 4.2 of the dimer's minimum, saddle point and dissociated monomers are all well described by the surface. Smooth dissociation of the dimer into HCl and H_2O is achieved at large separations as shown in Figure 4.3.

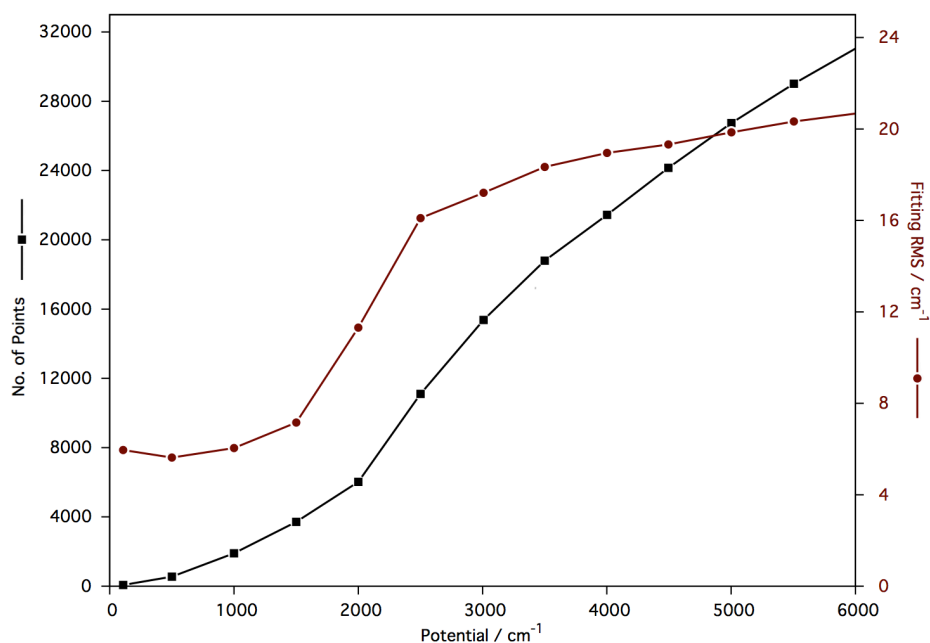


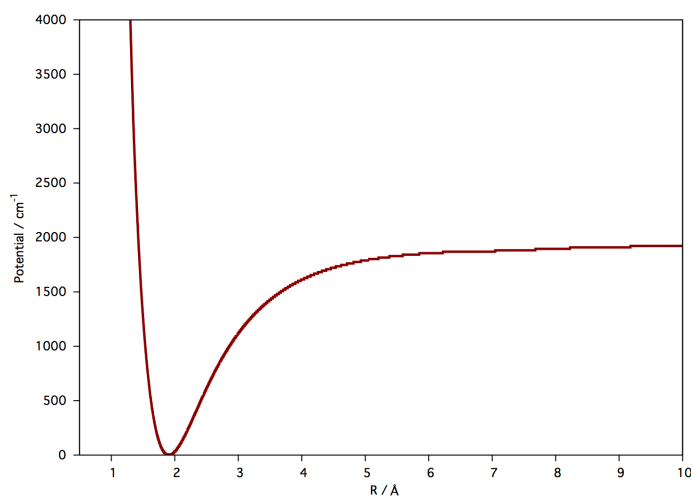
Figure 4.2: Energy as a function of the number of points and the respective RMS fitting error for a portion of the fitting data.

Table 4.1: Geometry (\AA and degrees) of indicated configuration from *ab initio* calculations and the potential energy surface for the global minimum, transition state and dissociated monomers.

	Minimum		Planar		Monomers	
	<i>ab initio</i>	PES	<i>ab initio</i>	PES	<i>ab initio</i>	PES
R_{HCl}	1.292	1.292	1.289	1.289	1.277	1.277
R_{OH}	0.960	0.960	0.959	0.959	0.959	0.956
θ_1	105.15	105.12	105.64	105.67	104.44	104.45
θ_2	135.63	135.87	180.0	179.93	-	-
θ_3	177.96	177.43	180.0	180.0	-	-
R	1.902	1.903	1.916	1.917	-	-

Table 4.2: Harmonic Frequencies (cm^{-1}) for $\text{HCl-H}_2\text{O}$ from *ab initio* calculations and the PES for the global minimum, transition state and dissociated monomers.

Minimum		Planar		Monomers	
<i>ab initio</i>	PES	<i>ab initio</i>	PES	<i>ab initio</i>	PES
145	149	152	161 <i>i</i>	-	-
167	169	146	142	-	-
190	196	150	152	-	-
452	458	386	391	-	-
559	562	512	512	-	-
1647	1649	1644	1646	1650	1641
2800	2800	2841	2848	2994	2991
3826	3827	3838	3842	3835	3836
3940	3934	3948	3951	3944	3954

**Figure 4.3:** Minimum energy potential along the dissociation coordinate of the dimer computed using the new dimer potential energy surface.

The data for fitting was obtained from geometries calculated using classical direct-dynamic simulations, performed with density functional theory, B3LYP/ aug-cc-pVTZ. These classical simulations began with a variety of different kinetic and potential energies. Long-distance molecular configurations characterized by a $\text{HCl-H}_2\text{O}$ separation greater than 5.5 \AA were sampled by re-evaluating portions of the shorter-distance geometries at increased intermolecular separation. The maximum Cl-O distance of the fitted geometries was 12 \AA . The surface fitting proceeded in the usual iterative fashion, specifically, by 1) performing a preliminary fit, 2) testing the fit

using classical trajectories and DMC calculations of the ZPE and then 3) adding additional points in poorly described areas and re-fitting. The process completes when the objectives are met. In the present case, this is when the surface produces accurate properties of stationary points, yields sensible classical trajectories up to around 15 000 cm^{-1} and dissociates smoothly with an accurate description of the fragments.

As is well known, basis set superposition error (BSSE) is a concern in hydrogen-bonded systems. To investigate this for HCl-H₂O, counterpoise (CP) corrected energies¹⁴⁶ and benchmark energies determined from a complete basis set (CBS) extrapolation¹⁴⁷ were calculated. The CBS calculations also account for basis set incompleteness error (BSIE). The CP correction was applied according to

$$\Delta E_{\text{BSSE}} = E_{\text{HCl}}^* + E_{\text{H}_2\text{O}}^* - E_{\text{HCl}}^\dagger - E_{\text{H}_2\text{O}}^\dagger \quad (4.1)$$

$$E_{\text{CP}} = E_{\text{dimer}} - \Delta_{\text{BSSE}}, \quad (4.2)$$

where E^* refer to the energies of the monomer in the dimer basis and E^\dagger are the energies of the monomers in their own basis, both in the same configuration as in the dimer complex. The CBS calculations were performed by fitting CCSD(T) energies computed using aug-cc-pVDZ, aug-cc-pVTZ, aug-cc-pVQZ and aug-cc-pV5Z and the following equation

$$f(n) = E_{\text{CBS}} + \alpha e^{-\beta n}, \quad (4.3)$$

where n is the cardinal number of the basis set, $f(n)$ the energy, α and β fitting parameters and E_{CBS} the energy at the complete basis set limit determined by the fit. A comparison of some relevant uncorrected, CP-corrected, CBS and PES determined energies are given in Table 4.3. The CP-corrected energies gave a higher energy D_e and double-well barrier height than the CBS values. In this case, the uncorrected energies as well as those from the PES are in good agreement with the CBS values.

Table 4.3: Double-well barrier (DWB) and electronic dissociation D_e (cm^{-1}) from *ab initio* calculations (see text for details) and the PES.

Property	PES	CCSD(T)/aVTZ-F12b	CCSD(T)/aVTZ-F12b-CP	CCSD(T)/CBS
DWB	59	59	70	49
D_e	1924	1929	1848	1915

DMC calculations were conducted in the standard way.^{29,30} In these calculations 30000 “walkers” were equilibrated for 10000 steps and propagated for 190000 steps with a step size of 2.5 imaginary atomic time units and an α of 2.5. The ZPE was determined by performing 19 block averages of the trajectory and then taking the average of the 19 blocks to be the ZPE and the deviation in the blocks as the statistical uncertainty. The value of the ZPE is within 3 cm^{-1} of simulations using a 5.0 imaginary atomic time unit step size, thus assuring minimal systematic errors are present with the smaller step size.

4.2.3 GROUND STATE PROPERTIES OF THE $(\text{HCl})(\text{H}_2\text{O})$

Based on the DMC simulations, the bound HCl-H₂O complex’s anharmonic ZPE is $6688 \pm 3 \text{ cm}^{-1}$. The ZPE from the surface of the dissociated H₂O and HCl monomers was obtained by performing a DMC calculation with the fragments separated by 12 Å and a value of $6126 \pm 3 \text{ cm}^{-1}$ was determined. This compares very well with a separate DMC using the spectroscopically-accurate Partridge-Schwenke water potential¹⁴⁸ and a new HCl potential. The latter was generated from a 8th order polynomial fit using a Morse-like basis to 215 CCSD(T)/aug-pVTZ-F12b points. The DMC ZPE for these separated fragments is $6121 \pm 2 \text{ cm}^{-1}$, which is in excellent agreement with the PES result.

From the PES dimer and fragment ZPEs and the PES D_e of 1924 cm^{-1} , D_0 is given by $1362 \pm 3 \text{ cm}^{-1}$. This is in good agreement with the experimental value of $1353 \pm 4 \text{ cm}^{-1}$. However, using the D_e from the CCSD(T)/CBS calculation and the ZPE from the Partridge-Schwenke and current HCl potential the D_0 is given by 1348

cm^{-1} with an uncertainty of ± 3 , in even better agreement with experiment. (It is interesting to note that using the harmonic ZPEs from the PES, the D_0 is 1254 cm^{-1} , which is not in good agreement with the rigorously calculated D_0 and experiment.) The D_0 for the deuterated isotopologue was calculated to be $1476 \pm 3 \text{ cm}^{-1}$ (using the CBS D_e).

In addition to determining the ZPE, the DMC calculations allow for the visualization of the HCl-H₂O wavefunction. An isosurface showing the ground state wavefunction of the dimer is given in Figure 4.4. As seen, the hydrogen atoms of the water molecule are largely delocalized across the two global minima, yielding an average C_{2v} configuration. Similar delocalized behavior was observed for the DMC calculations on other deuterated forms of the complex.

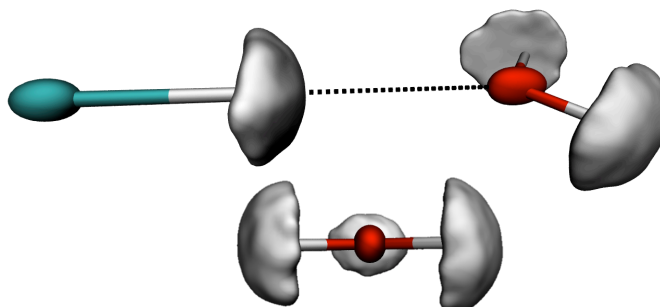


Figure 4.4: Visualization of the HCl-H₂O dimer DMC ground state wavefunction from two perspectives.

To further support this visual finding of delocalization of the ground vibrational state wavefunction, a 1-D Schrödinger equation using the relaxed 1-D potential along the transition state's out-of-plane imaginary frequency bending mode was solved numerically.^{149,150,151} Specifically, this involved moving along the imaginary normal mode coordinate of the saddle point and the performing a geometry optimization using the other real valued normal mode coordinates. In these calculations the relaxed 1-D cut was fit to a 10th order polynomial. The Schrödinger equation was solved numerically using 1000 equally-spaced points using a discrete variable repre-

sentation calculation. The ZPE is 52 cm^{-1} above the double-well barrier. In addition, the square of the double-well wavefunction indicates that the most probable configuration is that of the planar C_{2v} geometry. A plot of the 1-D double well potential with its ZPE and the square of the wavefunction are given in Figure 4.5. In addition, to investigate isotope effects on the ZPE barrier, a 1-D potential curve for the DCI- D_2O dimer was constructed and solved resulting in a ZPE 13 cm^{-1} above the barrier and a delocalized wavefunction.

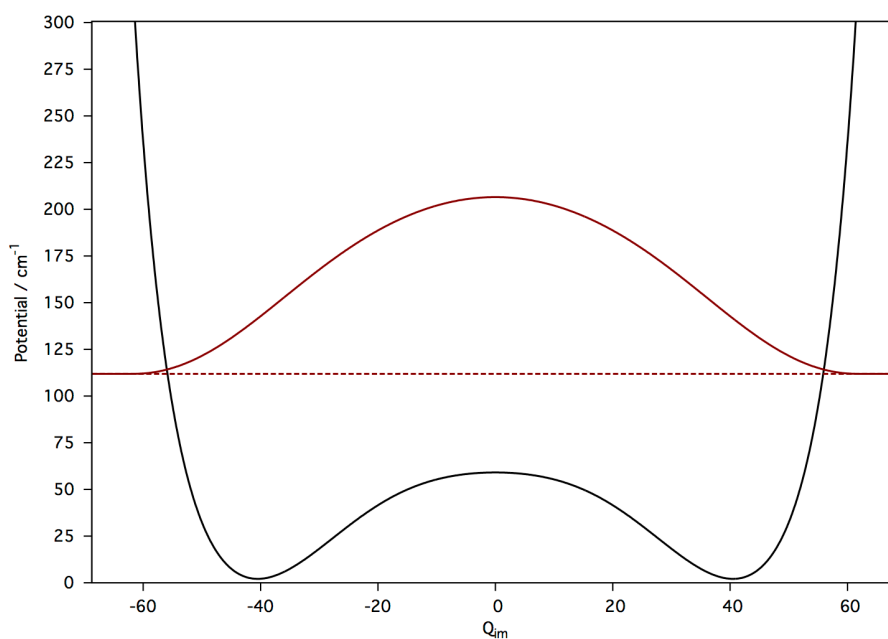


Figure 4.5: Relaxed 1-D potential cut along the imaginary frequency mass-scaled normal mode of the transition state. The solution to the 1-D Schrödinger equation for the ZPE and the square of the wavefunction are shown in red.

Additional support for the reality of the C_{2v} zero-point geometry comes from a comparison of theoretical and experimental rotational constants. The rotational constants were computed using the geometries optimized on the PES. The B- and C-constants are 0.13 cm^{-1} in both geometries and A-constant is 11.47 cm^{-1} in the C_s global minimum and 14.34 cm^{-1} in the planar C_{2v} saddle point. The latter is in good agreement with the experimentally reported values from infrared spectroscopy of 14.85 cm^{-1}

from studies in helium¹⁴⁵ and between 14-15 cm^{-1} from gas phase studies.¹³²

4.2.4 SUMMARY AND CONCLUSIONS

To conclude, an accurate full-dimensional potential energy surface based on CCSD(T)-F12b/aug-cc-pVTZ energies was constructed for of HCl-H₂O. The surface is capable of reproducing the geometries, harmonic frequencies, dissociation energy and isomerization pathway of ab initio calculations. The surface was used to perform rigorous calculations of the dimer D_0 and report a value of $1348 \pm 3 \text{ cm}^{-1}$ in good agreement with the experimentally measured value of $1334 \pm 10 \text{ cm}^{-1}$. In addition, the DMC calculations allowed for the visualization and rigorous determination of the HCl-H₂O ground state geometry as being highly delocalized over the double well minimum resulting in an average C_{2v} configuration. The delocalized average C_{2v} was further verified by determination of the double well ZPE above the inversion barrier in a 1-D calculation using in the saddle point imaginary-frequency normal mode. Additional support comes from agreement of the saddle-point geometry's A-constant, 14 cm^{-1} , with experimental values, $\sim 14 - 15$.^{145,132}

4.3 EFFECTS OF ZERO-POINT DELOCALIZATION ON THE VIBRATIONAL FREQUENCIES OF MIXED HCL AND WATER CLUSTERS

4.3.1 CONTEXT

It is traditionally assumed in molecular studies that a global minimum energy configuration can effectively characterize the properties of a system, e.g., rotation constants. This concept hinges on the zero-point motion at the system's global minimum effectively "averaging-out" to zero-displacement and localizing the system at the global minimum configuration. If, however, an estimate of the zero-point energy at the

minimum is larger than or even comparable to barrier(s) to other isomers, then delocalization of the zero-point wavefunction may be indicated. This is especially the case if there are low-frequency, large-amplitude motions that connect to other stationary points. In these cases, properties based on assuming a global minimum reference structure may be in error.

The previous section demonstrated a clear example of this delocalized ground-state behavior in terms of the $(\text{HCl})(\text{H}_2\text{O})$ dimer.^{152,141,130} The $(\text{HCl})(\text{H}_2\text{O})$ dimer is the smallest mixed cluster and as such it is the start of a series of mixed $(\text{HCl})_n(\text{H}_2\text{O})_m$ clusters that eventually leads to the formation of ionized HCl acid. This is a topic of considerable interest.^{153,141,145,109,129,133,154,116,155,36,117,114,126,127,139,128,125,123,124,140,156,136,131,135,137,134,55,157} A number of theoretical studies have reported that the smallest cluster for which HCl dissociation occurs is four H_2O and one HCl.^{154,116,126,127,139,128,123,124,140,41,157} Infrared vibrational spectroscopy experiments on the clusters have sought to identify the first case of acid formation.^{153,40,41,145,129,109,133} In the course of these studies it has been suspected that the larger clusters may exhibit similar delocalization behavior as that observed in the dimer. Electronic structure calculations have found that the lowest energy configurations of mixed clusters containing between three and five monomers are non-planar rings. The non-planar conformation is reasonable as these place the free OH stretches above and below the plane of the ring. However, if the barrier for the free OHs to move through the plane of the cluster is small enough, the cluster could delocalize over several configurations in the ground vibrational state. Indeed, detailed analysis of the microwave spectrum of the $(\text{HCl})_2(\text{H}_2\text{O})_1$ cluster performed by Kisiel and co-workers concluded that some aspects of the spectrum imply an effectively planar configuration.¹⁵⁵ Since the global minimum is not planar, this stands as another example of a delocalized ground state. The authors go on to say that the precise details of the cluster's internal motions are still to be resolved. This is done here for $(\text{HCl})_2(\text{H}_2\text{O})_1$ and for other $(\text{HCl})_n(\text{H}_2\text{O})_m$ clusters.

Finally, while ground-state delocalization has been reported in numerous systems, including Ar_nHF,^{158,159} CH₅⁺,¹⁶⁰ H₅⁺,^{161,143,162} H₃O₂⁻,¹⁶³ and H₃O⁺(H₂O)₃Cl⁻,^{154,117,36,157}, the effects of the delocalization on fundamental vibrational frequencies have not been extensively studied.

In this section, the details of the zero-point behavior of all (HCl)_n(H₂O)_m dimers, trimers and tetramers are reported along with how the delocalization affects these cluster's fundamental vibrational frequencies. Direct comparisons are made with available experimentally reported vibrational frequencies. The studies were performed using diffusion Monte Carlo calculations and anharmonic coupled vibrational calculations, all conducted on a state-of-the-art many-body potential energy surface. While previous theoretical studies of the vibrational spectroscopy were performed for these systems,^{141,126,125,127} no study considered the effects of ground-state delocalization combined with an anharmonic, coupled-mode vibrational analysis.

4.3.2 MANY-BODY POTENTIAL FOR (HCL)_n(H₂O)_m CLUSTERS

All calculations in this section were conducted with a new full-dimensional, many-body potential energy surface containing all one- two- and three-body interactions for the (HCl)_n(H₂O)_m clusters (without consideration of dissociation to ions). The many-body potential, V , for a cluster consisting of n HCl monomers and m H₂O monomers, and limited to three-body interactions, is given by

$$\begin{aligned}
 V(\mathbf{H}_n, \mathbf{W}_m) = & \sum_{i=1}^n V_{\text{H}}(i) + \sum_{i=1}^m V_{\text{W}}(i) + \\
 & \sum_{i<j}^n V_{\text{HH}}(i, j) + \sum_{i=1}^n \sum_{j=1}^m V_{\text{HW}}(i, j) + \sum_{i<j}^m V_{\text{WW}}(i, j) + \\
 & \sum_{i<j<k}^n V_{\text{HHH}}(i, j, k) + \sum_{i<j}^n \sum_{k=1}^m V_{\text{HHW}}(i, j, k) + \sum_{i=1}^n \sum_{j<k}^m V_{\text{HWW}}(i, j, k) + \sum_{i<j<k}^m V_{\text{WWW}}(i, j, k),
 \end{aligned}
 \tag{4.4}$$

where H refers to HCl monomers and W refers to H_2O monomers. This notation is used, when convenient below, to refer to the various clusters.

The many-body potential is constructed from existing and new *ab initio*-based potentials. The homogenous one- two- and three-body interactions are described by the WHBB many-body water potential^{11,48} and with the many-body HCl potential detailed in Chapter 3.¹⁶⁴ In both potentials the one-body monomer potentials are spectroscopically accurate ones.^{78,148} The intrinsic two-body HCl potential is extracted from the semi-empirical EL-ES1 dimer potential.⁶⁴ The heterogenous two-body interaction for HW is accounted for using an intrinsic two-body fit to the same $\sim 44,000$ configurations used to generate CCSD(T)-F12/aug-cc-pVTZ potential in the pervious section.¹⁵² The two-body and three-body components of the WHBB potential are a permutationally invariant fit to roughly 30,000 CCSD(T)/aug-cc-pVTZ energies and 40,000 MP2/aug-cc-pVTZ energies, respectively. All of the previously reported potentials have been used to compute dynamic and spectroscopic properties, for their respective systems, in agreement with experiment.^{165,58,166,152,167} New to this work are two MP2-F12/aug-cc-pVDZ, permutationally invariant, intrinsic three-body potentials for the HHW and HWW interactions. These new three-body potentials were each constructed from fits to roughly 50,000 energies using permutationally invariant polynomials up to total order six in terms of Morse variables, $\exp(-r_{ij}/\lambda)$, where r_{ij} are the intermolecular distances and the range parameter, λ , equals 2 bohr.^{3,83,84} The root-mean squared deviation of the two fits were both less than 7 cm^{-1} . A plot demonstrating the fitting RMS as function of the computed energies is given in Figure 4.7. The RMS errors are small at the areas near the global minima (-542 for HHW and -792 for HWW) and when the potentials are effectively zero. It is of note that the three-body RMS's do rise as the three-body interaction energy becomes less than the interaction at the minimum. This is because fewer configurations are computed at these points as they relate to areas where the two-body interactions are highly re-

pulsive. The MP2-F12 method was chosen due to its speed and ability to reproduce three-body energies for a test set of configurations to within 20 cm^{-1} of CCSD(T)-F12/aug-cc-pVTZ calculations. All energies were computed using MOLPRO 2010.⁷⁷ The four-body interactions in the $(\text{HCl})_1(\text{H}_2\text{O})_3$, $(\text{HCl})_3(\text{H}_2\text{O})_1$ and $(\text{HCl})_2(\text{H}_2\text{O})_2$ clusters account for less than 4% of the total interaction energy. Its small contribution justifies excluding this higher-body interaction in the many-body potential.

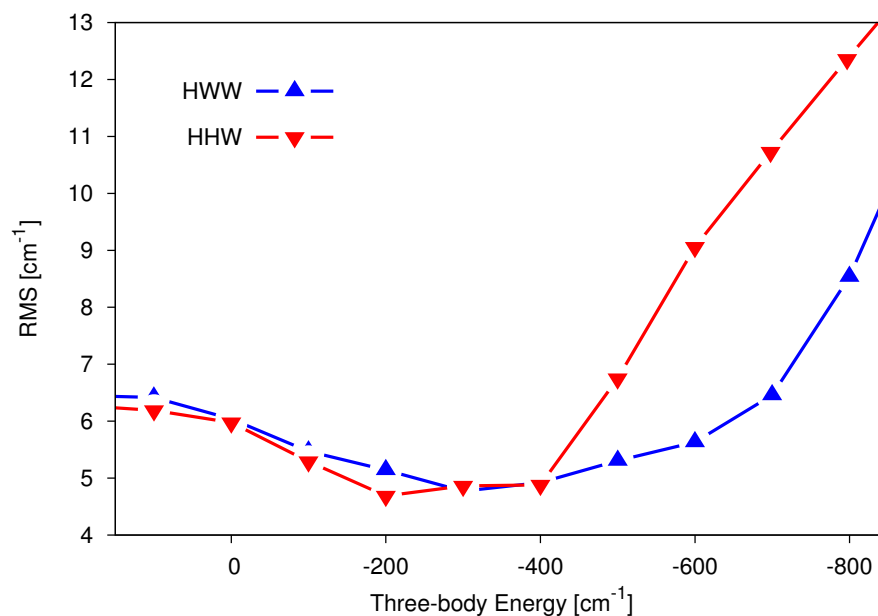


Figure 4.6: Root-mean-square (RMS) of the three-body potential fitting errors as a function of the trimers' three-body energies.

The many-body potential allows for smooth dissociation of any arbitrary sized cluster with each of the interactions going to zero at their respective interaction limits. The range and relative contributions of the various interactions, as it pertains to the two mixed trimers, are shown with one-dimensional cuts shown in Figure 4.7. The cuts were constructed by simultaneously compressing and then separating the three monomers along vectors which allow the monomers to pass through the respective trimer minima. Examination of the plots shows that the two-body interactions contribute substantially more to the total interaction energy ($\sim 85\%$) relative to the

three-body interactions ($\sim 15\%$). The three-body energy is relevant only at small molecular distances, with the interaction becoming effectively zero at average heavy atom distances greater than 6 Å and 5 Å for the HHW and HWW potentials, respectively.

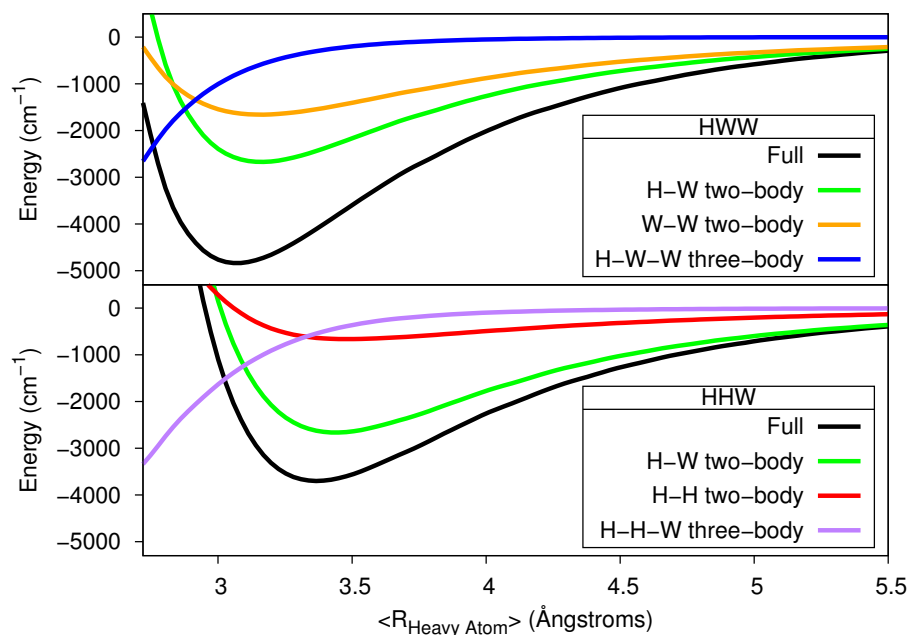


Figure 4.7: Potential energy cuts of three-body and two-body potentials in the $(HCl)_2(H_2O)$ [HHW] and $(HCl)-(H_2O)_2$ [HWW].

4.3.3 THEORETICAL METHODS FOR THE STUDY THE $(HCl)_n(H_2O)_m$

The many-body potential surface was used to perform diffusion Monte Carlo simulations for the six mixed clusters to obtain the full-dimensional ground state vibrational wavefunctions.^{29,30} Plotting and visual examination of these wavefunctions as shown in the previous studies reported in this dissertation, allows for the extent of ground state delocalization to be surmised. Furthermore, by comparing the wavefunction plots with the geometries of optimized stationary points, a DMC based configuration may be identified. The simulations for each system were performed using 30,000 “walkers” an imaginary times step of 2.5 atomic units, an α value of 0.4, an equilibra-

tion period of 3,000 steps and a propagation period of 10,000 steps. Two simulations were performed for each system starting from the completely planar configuration and from the global minimum. The plotted wavefunctions correspond to the lowest zero-point energy of the two simulations. In the case of the dimer, the calculations reported in the previous section repeated with the many-body representation of the potential and not the explicit dimer potential.

Coupled, anharmonic vibrational configuration interaction calculations were performed to obtain the stretching and bending energies of the dimer, trimer and tetramers of $(\text{HCl})_n(\text{H}_2\text{O})_m$. The calculations were done using with the code Multimode^{19,20,21}. Ideally, a full-dimensional calculation considering all the modes, including ones that span the global minimum and saddle points, should be done. However, such a calculation is not feasible for the large systems studied here, and so two approximate approaches were taken. In brief, in one approach the ground state is characterized by a single-reference configuration, either the global minimum or a planar saddle point. Calculations are then performed at these configuration for a subset of high-frequency local or full normal-modes which contain the HCl stretches, the OH stretches and the HOH bend. In another, novel approach, multiple coupled vibrational calculations (in a subset of local normal-modes) are done over a reaction path or surface which describe the configurations which are explored by the large amplitude motions of the clusters. This path or surface is constructed along the imaginary frequency normal-modes of the first or second-order planar saddle points, with the geometry optimized with respect to all non-imaginary frequency normal-modes. The imaginary frequency normal-modes correspond predominately to the wagging motions of the free-OHs. The later approach is denoted DLOC, to indicate it's "delocalized" nature.

In the delocalized approach (DLOC) the Schrödinger equation is solved in reduced dimensionality using one or two large amplitude modes described in detail below. This is done by first defining a reaction coordinate or surface that contains the relevant

saddle points and minima. The imaginary frequency normal-mode Q_{im} of a first-order saddle^{151,150,149} or two imaginary frequency normal-modes of a second-order saddle point, if that is the relevant saddle point, are used to construct coordinates. In all cases the imaginary frequency normal-modes correspond predominantly to the free OH wagging motions. At each point on the surface the corresponding geometry is optimized with respect to all non-imaginary frequency normal-modes. A discrete variable representation calculation²³ using 150 points per dimension is used to solve for the delocalized ground state wavefunction of the surface. The vibrational frequencies of hundreds of configurations on the surface are computed, weighted according to the surface's wavefunction squared and the values integrated to give a single set of delocalized vibrational frequencies. In light of the DMC results the HWWW's reduced dimensional surface was generated in two dimensions, centered on a second-order saddle point, with the free OH of monomers β and γ in planar configurations and the OH of monomer α in a non-planar configuration. The grid of points along the two imaginary frequencies were optimized with respect to all the other non-imaginary normal-modes except for the normal-mode associated with the large amplitude motion of monomer α 's free OH.

Returning to the Multimode calculations, in both the single and multi reference calculations the low frequency modes were considered to have negligible effects on the vibrations. In the previous studies of HCl trimer, Chapter 3, good agreement between similar local calculations and those performed here were achieved without the consideration of low frequency vibrations.¹⁶⁴ Calculations were performed using either a traditional approach involving the full normal-modes or a local approach. The traditional approach solves for the vibrational frequencies in terms of the normal-modes of the whole cluster. The largest of these calculations was applied to HWW which included seven modes and a three-mode representation of the potential. The local approach uses the local-monomer (LMon) technique described in Chapter 3.^{48,87} The

LMon method results in three-dimensional calculations for the H_2O monomers and one-dimensional calculations for the HCl. In clusters with multiple HCl monomers, the HCl's stretches are considered in the field of the H_2O monomer(s). Substantially smaller computation time is required to performed the LMon calculations, with anharmonic frequency errors on average less than 10 cm^{-1} relative to those computed using traditional calculations. The local method makes it computationally possible to perform the hundreds of calculations involved in the DLOC approach, as well as to study the HWWW (eight modes) and HHWW (ten modes) cluster at their stationary points. The Multimode basis was chosen to mirror the basis set of previous LMon studies of HCl and water cluster. The modes involving the HCl and H_2O monomers used 10 and 13 harmonic basis functions, respectively.

The global minimum and neighboring low-lying stationary points (under 600 cm^{-1}) of the dimer, trimers and tetramers were located on the potential using codes contained in the NLOpt optimization package.¹⁶⁸ The planar configurations for the six clusters studied here are shown in Figure 4.8. While all the clusters' (with the exception of the dimer) form non-planar ring configuration at their global minima, the planar stationary points provide a better reference structure for this study (see discussion below). In the global minima the free OHs all point either above or below the plane of the ring, alternating between the different sides of the ring plane. Other low-energy stationary points are characterized by the free OHs oriented, individually, either in or out of the ring plane. It should be noted that the configuration of the $(\text{HCl})_2(\text{H}_2\text{O})_2$ cluster with the monomer ordering HWWW is lower in energy than the HHWW ordering shown in Figure 4.8. The HHWW form is, however, the one reported experimentally^{41,40,153} and so is focused on here.

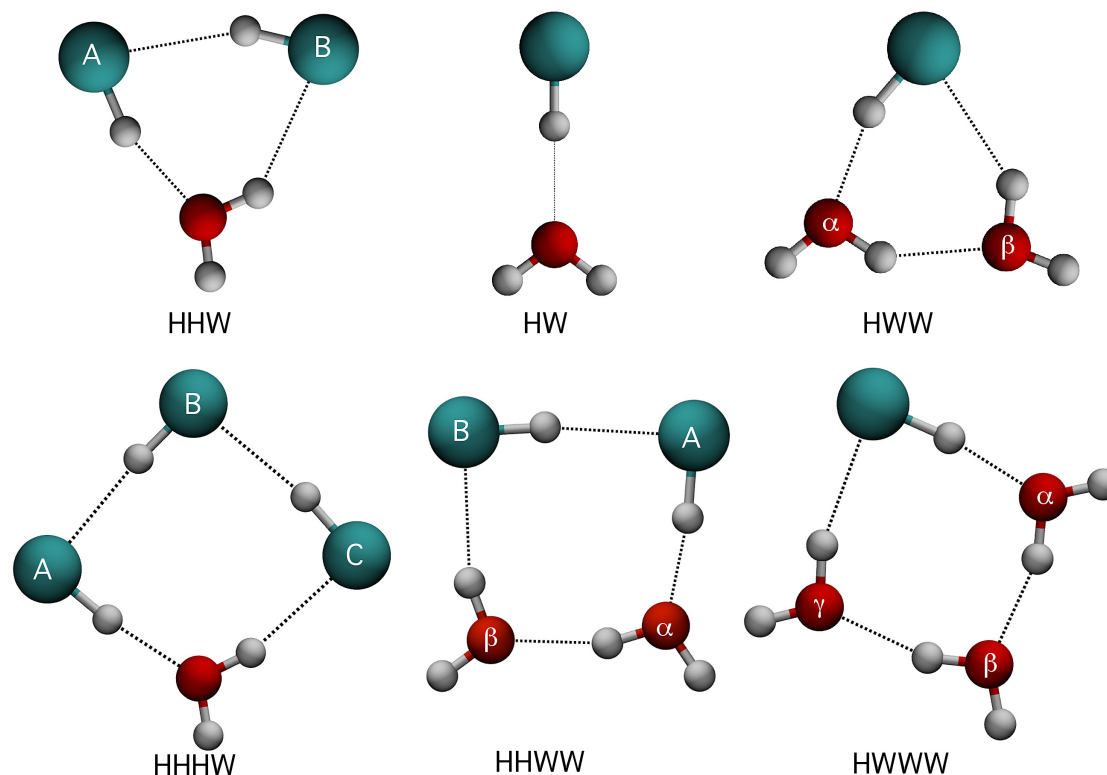


Figure 4.8: Planar configurations of indicated HCl and H_2O clusters.

4.3.4 VIBRATIONAL GROUND STATE PROPERTIES OF $(\text{HCl})_n(\text{H}_2\text{O})_m$

Isosurface plots of the zero-point wavefunctions are shown in Figures 4.9 and 4.10 where, in Figure 4.9 the reference planar configurations in Figure 4.8 rotated 90 out of the plane of the page. In Figures 4.9 and 4.10, the H atom motion of the free OH bonds displays the most delocalization. The HCl monomers are relatively more localized, certainly far more localized than was seen in the HCl dimer.^{64,165} This seems reasonable due to constraints imposed by the ring configuration, as was demonstrated by the contrasting nature of the DMC wavefunctions of the HCl dimer and ring trimer.¹⁶⁵ The extent of the delocalization in the free OHs can be understood by examining the magnitude and shape of the OH wavefunction densities in the planar positions of the clusters. Each free OH in the clusters behaves uniquely and so they are best addressed individually. Full delocalization occurs when the OH

density smoothly spans the two out-of-plane positions. These OHs move freely in the ground state as though no barrier to isomerization exists. The OHs of HW and HWW(α), where the letter in parentheses refers to the specific monomer labeled in Figure 4.8, both show this delocalized behavior. Experimental observations of these OHs would find them in the plane of the cluster. Partial delocalization occurs when the density in the planar positions is smaller than the out-of-plane positions. In this case the zero-point energy in the OH large amplitude motion is not large enough to overcome the planar barrier entirely, but still large enough to allow a significant amount of barrier crossing to occur. Experimentally, these OHs will be seen as nearly planar. The free OHs of HHW, HWW(β), HHHW, HHWW and HWWW(α) all show this behavior and are best described by an effective planar orientation. The near planarity of the HHW reported here is in agreement with recent microwave observations of the cluster.¹⁵⁵ Small or zero delocalization occurs when nearly no hydrogen density is observed in the planar position. These OHs remain localized on one side of the plane of the molecule in the ground state. Localized free OHs appear only in HWWW(β) and HWWW(γ), with HWWW(γ) being much more localized than HWWW(β). It is worth noting that this transition to a more localized configuration as the number of H_2O monomer increases is not surprising if one recalls that the water trimer's ground state wavefunction is localized at ring shaped global minima with the OHs all in non-planar orientations. In the case of mix-clusters, as the number of H_2O monomers grows the clusters begin to behave more like the pure H_2O clusters for which the free OHs localize.¹⁶⁹

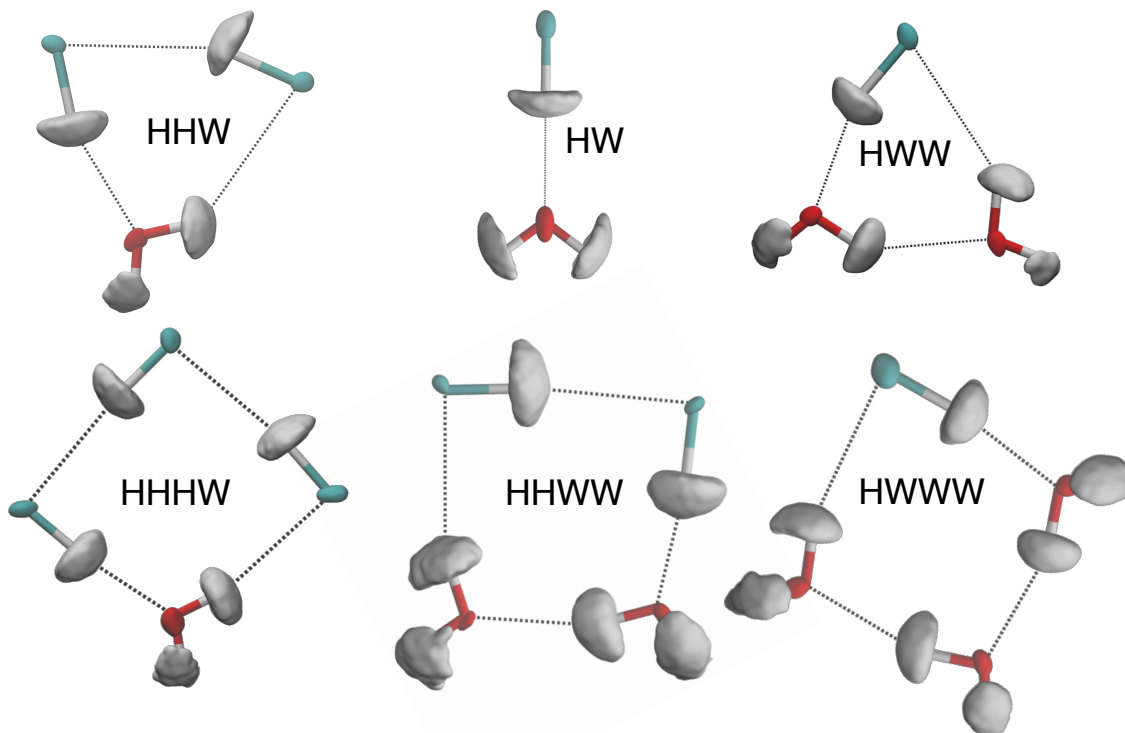


Figure 4.9: An isosurface representations of the vibrational ground state wavefunctions of the indicated mixed HCl and H_2O clusters computed using diffusion Monte Carlo simulations. The wavefunction representations are shown relative to the planar configurations.

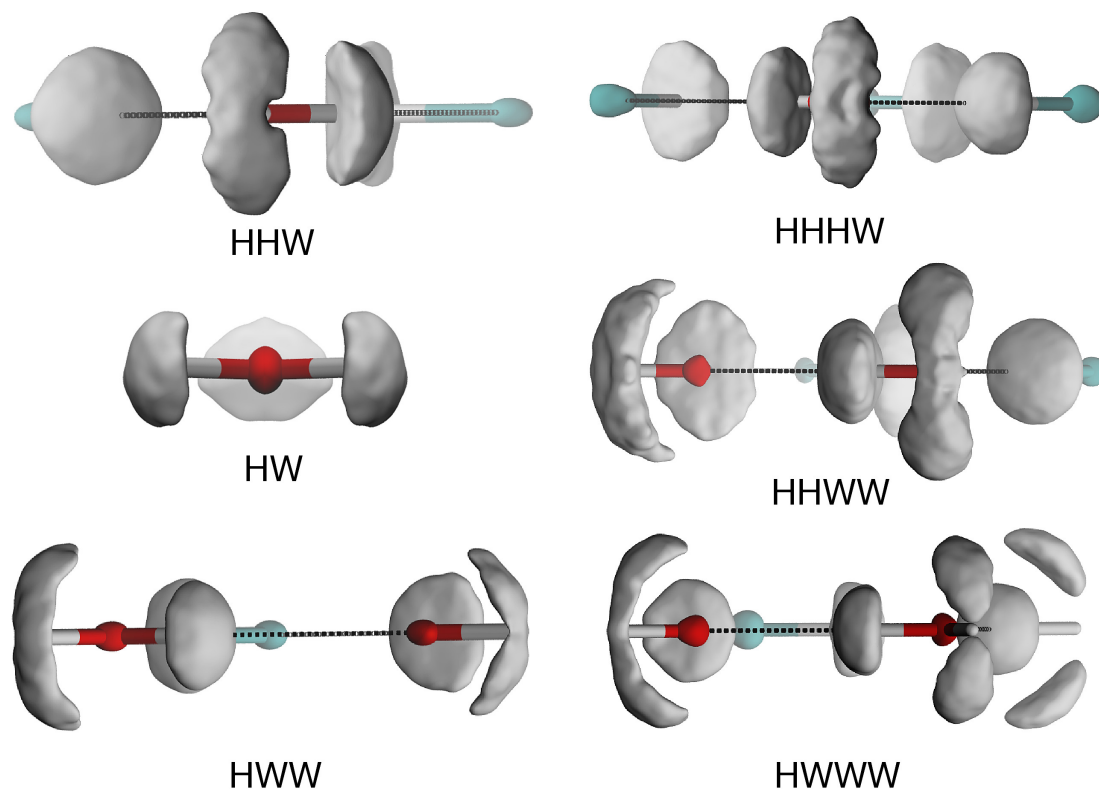


Figure 4.10: Isosurface representations of the vibrational ground state wavefunctions of the indicated mixed HCl and H₂O clusters computed using diffusion Monte Carlo simulations. The wavefunction representations are shown relative to the planar configurations.

Based on the DMC wavefunctions, the most-probable zero-point structures were determined, which represent the best single-reference geometry to perform vibrational calculations. The planar saddle points are the most-probable configurations for all but the HWWW cluster. A non-planar, first order-saddle point best describes HWWW, with the monomer (γ) and (β) oriented on opposite sides of the ring plane and monomer (α) in a plane of the ring. The energy differences in wavenumbers between the global minimum and the DMC most-probable configurations are: 57(HW); 366(HWW); 117(HHW); 326(HHWW); 72(HWWW) and 100(HHHW). It is also worth mentioning that the third-order planar saddle point configuration of HWWW is 586 cm^{-1} above the global minimum. Considering how high this is relative to the other cluster's planar configurations it is not surprising that it is largely unsampled in the ground state. For convenience in what follows the DMC predicted

structures are referred to as “planar”.

4.3.5 VIBRATIONAL EXCITED STATE PROPERTIES OF $(\text{HCl})_n(\text{H}_2\text{O})_m$

Anharmonic coupled vibrational energies were computed for the $(\text{HCl})_n(\text{H}_2\text{O})_m$ clusters using single-reference approaches at the global minima and planar geometries, and also using the DLOC approach. Presented first is a detailed discussion of the HWW cluster, which best demonstrates the effects of delocalization on the vibrational frequencies. The vibrational frequencies of all six clusters are then discussed in a more summary fashion.

The anharmonic and harmonic vibrational frequencies of the HWW trimer are presented in Table 4.4, where the results in the “Minimum” and “Planar” columns refer, respectively, to the single reference results computed at the global minimum and planar second-order saddle point configuration. The results in the “DLOC” column refer to the calculation that spanned multiple stationary points using the coordinates and wavefunction weighting shown in Figure 4.11. This notation is also applied below. As seen, the HCl stretch exhibits a 133 cm^{-1} harmonic and 170 cm^{-1} anharmonic shift between the two configurations. As expected, the DLOC calculation predicts the HCl stretch fundamental between the stationary point calculations but closer to the planar configuration result. Similar differences in the stationary point results of the OH stretches are observed, with the exception being the bound OH stretch of monomer β . The calculated bend frequency, however, shows very small variation between the three calculations. These results point to the large amplitude motions having a large effect on the computed vibrational frequencies resulting in large blue shifts. Comparing the computed values with experiment for the HCl-stretch, there are differences of -118 , $+52$, and -30 cm^{-1} for the minimum, planar and DLOC calculations, respectively. The better agreement with experiment for the planar and especially the DLOC calculation is expected, based on the discussion of the DMC wavefunction, where the

most probable configuration is the planar one. The delocalization of the wavefunction is large and thus the DLOC calculation is expected to provide the best physical description of the three and so the closer agreement with experiment is gratifying. The next most-sensitive results are for the H-bonded OH-stretch of H₂O(α). For this stretch the planar and DLOC results are in much better agreement with the tentative experimental assignment. The other OH-stretches differ only slight amongst the three calculations. The agreement of the computed OH-stretches with experiment is satisfactory, especially with regards to the more robust predictions of Reference¹⁴⁵. Considering the understandably poor results for the HCl-stretch using the minimum as the reference, it is worth noting that a one-dimensional anharmonic HCl stretch frequency has been reported for the global minimum using MP3/6-311++G(2d,2p).¹⁴¹ The result of 2467 cm⁻¹, which is in good agreement with experiment appears to be fortuitous and probably due to cancellation of error in the MP3 calculation.

Table 4.4: Harmonic, anharmonic and experimental vibrational frequencies (cm⁻¹) for HCl(H₂O)₂. †= 109 ‡= 145 *=Tentative Assignment

	Minimum		Planar		DLOC	Experiment
	Harm.	Anharm.	Harm.	Anharm.	Anharm.	
$\nu_{\text{bend-(H}_2\text{O)}_\alpha}$	1643	1586	1641	1580	1585	-
$\nu_{\text{bend-(H}_2\text{O)}_\beta}$	1654	1598	1646	1590	1587	-
$\nu_{\text{stretch-HCl}}$	2550	2342	2683	2512	2430	2460 [†]
$\nu_{\text{bonded stretch-(H}_2\text{O)}_\alpha}$	3695	3480	3751	3556	3518	3563 ^{†*}
$\nu_{\text{bonded stretch-(H}_2\text{O)}_\beta}$	3782	3590	3786	3589	3591	3618 ^{†*}
$\nu_{\text{free stretch-(H}_2\text{O)}_\beta}$	3898	3703	3927	3725	3717	3764 ^{†*} /3708 [‡]
$\nu_{\text{free stretch-(H}_2\text{O)}_\alpha}$	3910	3710	3946	3764	3742	3791 ^{†*} /3731 [‡]

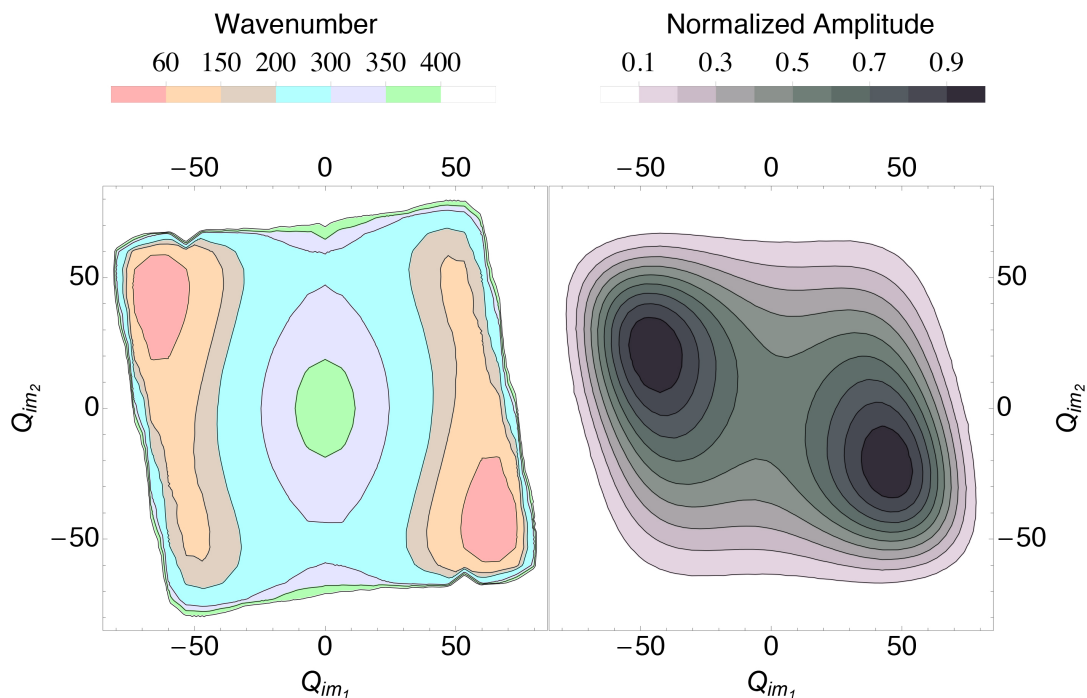


Figure 4.11: The HWW Q_{im} two-dimensional potential energy surface (left) and ground state normalized wavefunction squared (right). The surface's zero-point energy is 319 cm^{-1} .

To sum up thus far, agreement between experiment and the DLOC and planar configuration calculations validates the conclusion from the DMC wavefunctions of the zero-point state that the OHs are indeed highly delocalized. Also, the neglect of dynamical coupling to low-frequency intermolecular modes in the LMon approach used for this mixed cluster appears to be justified for the desired level of accuracy, which is of the order of $10\text{-}20 \text{ cm}^{-1}$. This level of accuracy was found for several homogeneous water clusters¹¹ for which benchmark results are available and also for the very floppy HCl discussed in Chapter 3.⁸⁷ To briefly review, for the latter the local normal-mode approach gives 2847 and 2860 cm^{-1} for the two HCl fundamentals⁸⁷ compared to the benchmark results of 2857 and 2877 cm^{-1} .⁶⁴ The delocalization of the free OHs have a significant effect on both the OH and HCl stretches resulting in inaccurate calculation of the fundamentals at the global minimum.

Analogous calculations to those just discussed for HWW were performed for each

cluster with their explicit values reported in Tables 4.5, 4.6, 4.7, 4.8 and 4.9. Plots of each cluster's reduced dimensional potentials and their respective wavefunctions, similar to Figure 4.11, are reported in the supporting information of 170. Due to the large number of calculated peak it is more useful to consider the results of Tables 4.5 - 4.9 in a general fashion with respect to the available experimental results than on an individual basis. Plots of the available experimental peak positions of the HCl-stretch and corresponding calculated results are shown in Figure 4.12. Comparing the single-reference calculations, the average absolute deviation is 65 cm^{-1} . The minimum and planar configuration results' absolute differences from the DLOC calculations are 39 and 30 cm^{-1} , respectively. The deviations between calculations are, however, not uniform. The largest differences are observed for the lowest frequency stretch in each of the clusters. These low frequency stretches all correspond to stretches of HCl monomers (labeled A in Figure 4.8) that donate a H-bond to a H_2O monomer. The exception to this behavior appears to be for HWWW. This is because unlike the other clusters the H-bond H_2O monomer's free OH is in a non-planar configuration in its ground state according to the DMC calculation. This allows the ground state in the area of the HCl monomer to resemble the global minima configurations. The similar configurations results in near equivalent vibrational frequencies. In this cluster the predicted vibrational frequency's agreement with experiment is of note as its peak position was only speculatively assigned in Reference 109. The mean absolute differences between the experimental peak positions and calculated results are $\sim 20 \text{ cm}^{-1}$ for the DLOC and planar calculations and 50 cm^{-1} for the minimum calculations. These summary results illustrate clearly the importance of considering the delocalized nature of the ground vibrational state (and also the excited state).

Table 4.5: Harmonic and anharmonic vibrational frequencies for HW.^{†=109 ‡=145 *=41}

	Minimum		Planar		DLOC	Experiment
	Harm.	Anharm.	Harm.	Anharm.	Anharm.	
$\nu_{\text{bend-H}_2\text{O}}$	1648	1592	1648	1582	1587	-
$\nu_{\text{stretch-HCl}}$	2803	2653	2853	2719	2689	2715*/2724 [†]
$\nu_{\text{bonded stretch-H}_2\text{O}}$	3827	3655	3829	3661	3656	-
$\nu_{\text{free stretch-H}_2\text{O}}$	3933	3748	3943	3758	3755	3762.9 [‡]

Table 4.6: Harmonic and anharmonic vibrational frequencies for HHW.^{†=109 ‡=145 *=41}

	Minimum		Planar		DLOC	Experiment
	Harm.	Anharm.	Harm.	Anharm.	Anharm.	
$\nu_{\text{bend-H}_2\text{O}}$	1646	1588	1639	1579	1581	-
$\nu_{\text{stretch-(HCl)}_A}$	2663	2484	2751	2597	2544	2580 [†]
$\nu_{\text{stretch-(HCl)}_B}$	2870	2759	2863	2753	2748	2757 [†] /2774*
$\nu_{\text{bonded stretch-H}_2\text{O}}$	3781	3573	3789	3592	3582	-
$\nu_{\text{free stretch-H}_2\text{O}}$	3905	3711	3929	3740	3729	3723 [‡]

Table 4.7: Harmonic and anharmonic vibrational frequencies for HHWW.^{‡=145 *=41}

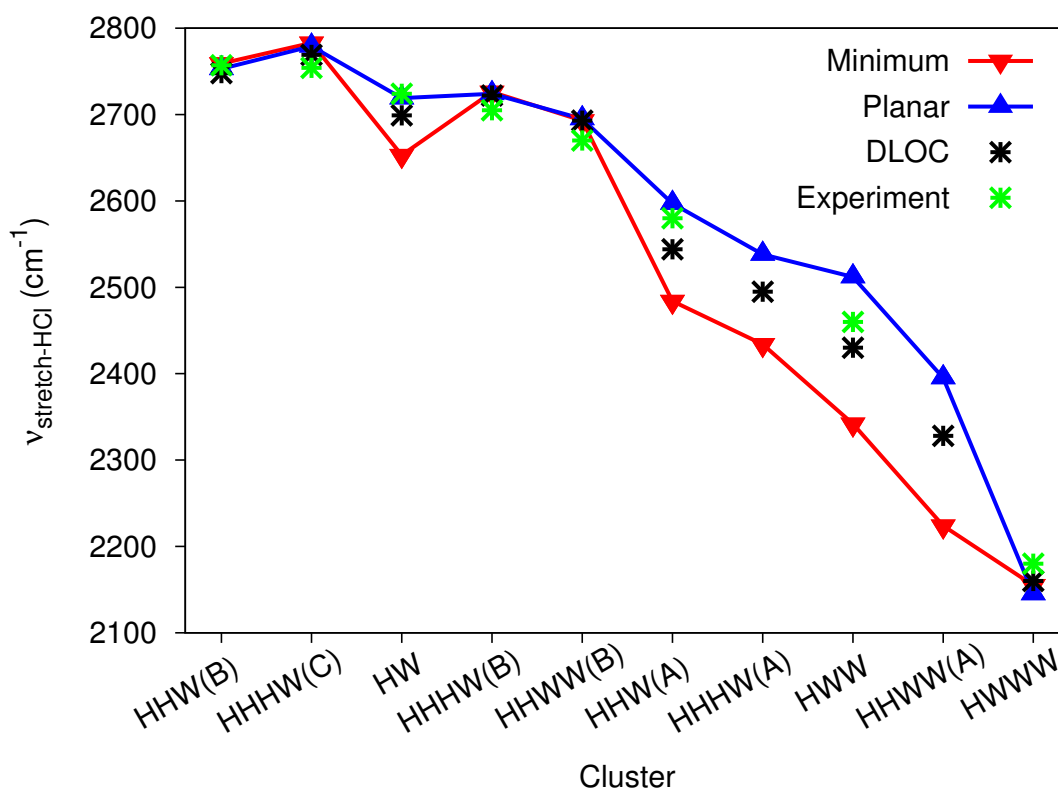
	Minimum		Planar		DLOC	Experiment
	Harm.	Anharm.	Harm.	Anharm.	Anharm.	
$\nu_{\text{bend-(H}_2\text{O)}_\alpha}$	1652	1603	1659	1605	1605	-
$\nu_{\text{bend-(H}_2\text{O)}_\beta}$	1674	1609	1673	1607	1609	-
$\nu_{\text{stretch-(HCl)}_A}$	2433	2224	2581	2395	2328	-
$\nu_{\text{stretch-(HCl)}_B}$	2813	2693	2814	2695	2693	2670*
$\nu_{\text{bonded stretch-(H}_2\text{O)}_\alpha}$	3637	3407	3695	3493	3461	-
$\nu_{\text{bonded stretch-(H}_2\text{O)}_\beta}$	3758	3546	3766	3550	3547	-
$\nu_{\text{free stretch-(H}_2\text{O)}_\alpha}$	3875	3686	3908	3724	3718	3731 [‡]
$\nu_{\text{free stretch-(H}_2\text{O)}_\beta}$	3897	3712	3911	3738	3719	-

Table 4.8: Harmonic and anharmonic vibrational frequencies for HHHW.^{†=153 *=41}

	Minimum		Planar		DLOC	Experiment
	Harm.	Anharm.	Harm.	Anharm.	Anharm.	
$\nu_{\text{bend-H}_2\text{O}}$	1670	1609	1666	1603	1602	-
$\nu_{\text{stretch-(HCl)}_A}$	2619	2434	2700	2538	2495	-
$\nu_{\text{stretch-(HCl)}_B}$	2846	2726	2845	2724	2722	2705*
$\nu_{\text{stretch-(HCl)}_C}$	2884	2783	2881	2779	2769	2754 [†]
$\nu_{\text{bonded stretch-H}_2\text{O}}$	3749	3534	3753	3550	3540	-
$\nu_{\text{free stretch-H}_2\text{O}}$	3894	3716	3910	3739	3728	-

Table 4.9: Harmonic and anharmonic vibrational frequencies for HWWW.^{†=109 *=41}

	Minimum		Planar		DLOC	Experiment
	Harm.	Anharm.	Harm.	Anharm.	Anharm.	
$\nu_{\text{bend}}-(H_2O)_\alpha$	1655	1606	1657	1605	1608	-
$\nu_{\text{bend}}-(H_2O)_\beta$	1667	1608	1674	1610	1610	-
$\nu_{\text{bend}}-(H_2O)_\gamma$	1683	1611	1676	1613	1613	-
$\nu_{\text{stretch}}-HCl$	2376	2155	2368	2145	2160	2180 [†]
$\nu_{\text{free stretch}}-(H_2O)_\alpha$	3570	3342	3565	3337	3368	-
$\nu_{\text{free stretch}}-(H_2O)_\beta$	3660	3449	3688	3482	3474	-
$\nu_{\text{free stretch}}-(H_2O)_\gamma$	3749	3542	3754	3545	3547	-
$\nu_{\text{bonded stretch}}-(H_2O)_\beta$	3889	3695	3887	3693	3690	3708*
$\nu_{\text{bonded stretch}}-(H_2O)_\alpha$	3896	3706	3896	3705	3717	3718*
$\nu_{\text{bonded stretch}}-(H_2O)_\gamma$	3914	3721	3929	3730	3726	-

**Figure 4.12:** Plot of anharmonic vibrational frequencies for the HCl stretch in the $(HCl)_n(H_2O)_m$ clusters. The monomer labeling used in the text is applied here for cases where multiple HCl monomers are present. The vibrational frequencies were computed at the global minimum configurations (Minimum) and the DMC predicted stationary point configurations (Planar), and using the DLOC calculations. Available experimental values are plotted for comparison.^{109,153,40,41}

An analogous summary plot is given in Figure 4.13 for the OH stretches. The single-reference calculations absolute mean deviation is 21 cm^{-1} . The minimum and

planar configuration results average absolute deviations from the DLOC results are, 17 and 9 cm^{-1} , respectively. Comparing the computed frequencies with experiment, the frequencies differ by 17 cm^{-1} from the global minimum results, 15 cm^{-1} from the planar configuration results and 9 cm^{-1} from the DLOC results. While the differences are not as large as in the HCl stretches, the consideration of the delocalization still results in the computation of more accurate OH stretch frequencies. It should be noted that the HOH bends show no more than a 10 cm^{-1} difference between any of the three calculations.

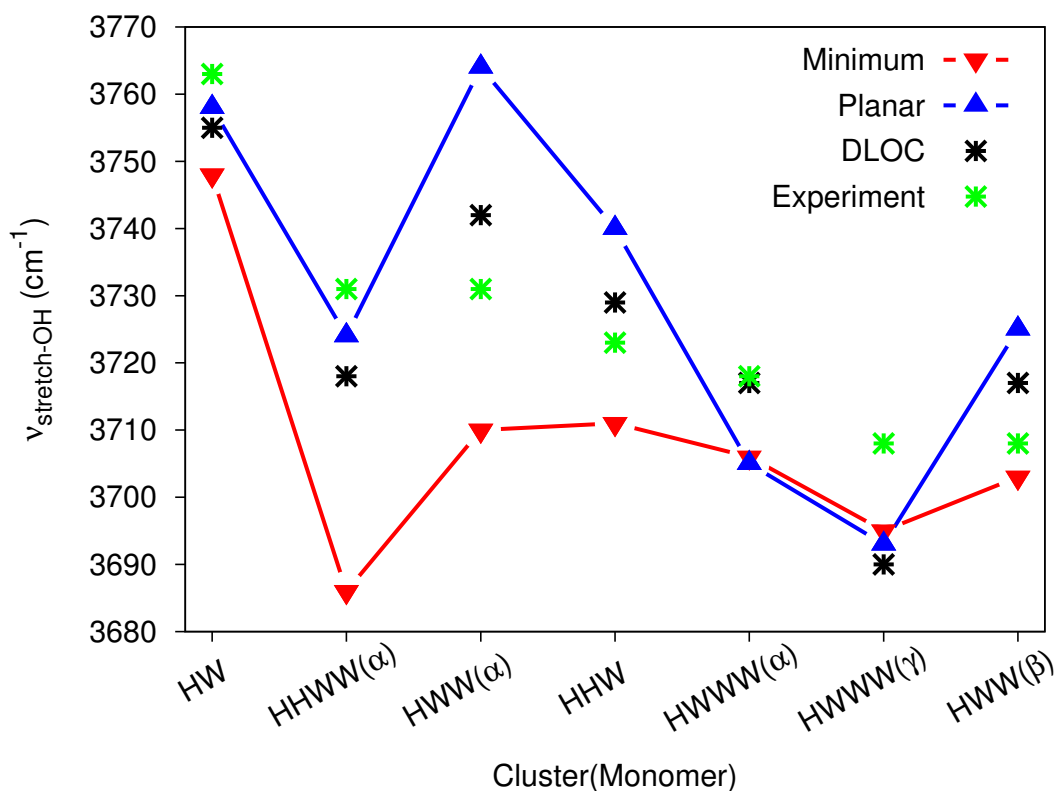


Figure 4.13: Plot of anharmonic vibrational frequencies for the OH stretch in the $(\text{HCl})_n(\text{H}_2\text{O})_m$ clusters that have reported experimentally in Reference¹⁴⁵. The monomer labeling used in the text is applied here for cases where multiple H_2O monomers are present. The vibrational frequencies were computed at the global minimum configurations (Minimum) and the DMC most probably configurations (Planar), and using the DLOC calculations.

It is useful to comment on the vibrational spectroscopy of these systems in terms of their harmonic frequencies. The large anharmonic coupled frequency shifts between

the three calculations, especially for each cluster's lowest frequency HCl stretch, are present in the harmonic results as well. An example of the harmonic behavior is shown for HWW in Table 4.4, which are now consider in some detail. While the delocalization is an anharmonic effect, the stationary point dependence of the frequencies is not. The HCl stretch harmonic frequency computed at the minimum shifts up by 133 cm^{-1} at the most probably planar reference configuration. This can be compared to the 170 cm^{-1} shift from the anharmonic coupled calculations. Nevertheless, both sets of harmonic results are much higher than experiment, as expected. The lower harmonic frequency is closer to experiment than the higher frequency result but this apparent "better" agreement is actually a misleading indicator of the most probable configuration. So clearly, a standard harmonic analyses (with perhaps a standard scale factor) at the global minimum would be a misrepresentation of the cluster dynamics. A DMC calculation of the zero-point wavefunction is not typically accessible to most theoretical studies, so investigating delocalization using approximate methods will often be necessary. This can be done by locating stationary points that are "near" the global minimum both in energy and configuration space. Standard harmonic analyses at these stationary points may be revealing of which configuration is the most likely.

4.3.6 SUMMARY AND CONCLUSIONS

In summary, large amplitude motions can have a significant effect on the vibrational frequencies of molecular clusters. Using a full dimensional potential energy surface diffusion Monte Carlo zero-point wavefunctions were obtained. The mixed HCl and H_2O dimer, trimer and tetramer clusters are delocalized in their respective ground states. Anharmonic coupled calculations of the first excited states of the HCl and OH stretch that were computed at the most probable DMC configuration are in good

agreement with experiment, whereas calculations that were performed at the conventional global minimum were not. The largest effects on these reported stretches involved HCl's donating a H-bond to ground state delocalized H_2O monomers. The observed ground state delocalization behavior and its effect on fundamental frequencies is likely not limited to just these mixed clusters as certainly other systems with large amplitude motions will encounter similar frequency shifts due to the delocalization. When studying these types of clusters, even at the harmonic level, it is prudent to consider the effects of ground state delocalization in order to achieve the best possible physical description of the vibrational dynamics and even the (zero-point averaged) structure.

5

$\text{H}_3\text{O}^+(\text{H}_2\text{O})_3 \text{Cl}^-$ Solvent Ion Pair Cluster

5.1 OVERVIEW

The proton transfer reaction is ubiquitous in pure and heterogenous liquid water. This is why the answer to the question, “How many waters are required for a single HCl monomer to auto-dissociation into H^+ and Cl^- ?” is of fundamental interest. The question has recently be a hotly debated one due to the complexities it presents both from an experimental and theoretical perspective. This section is dedicated to this question. In it a local-monomer based many-body potential energy surface is constructed comprising of five separate interactions to study the embedded H_3O^+ . The anharmonic 12-mode spectra for the embedded H_3O^+ is computed using this

embedded PES.

5.2 ISOLATING THE SPECTRAL SIGNATURE OF H_3O^+ IN THE SMALLEST DROPLET OF DISSOCIATED HCl ACID

5.2.1 CONTEXT

Fundamental studies of acids in biological and chemical contexts are obviously of great and intense interest.^{171,172,173,174,175} Recent research has focused on basic questions, such as how many water molecules are required for acid formation, i.e., dissociation, to be favored over undissociated states.^{176,177,178,179,180,181,182} The answer is typically sought by the detecting the presence or absence of signature spectral features of the hydrated proton in the infra-red. These signatures are a matter of current high interest not only in acids but in closely related contexts, such as the purely hydrated H^+ with no negative counter ion. In the latter, the fundamental question is whether the hydration state is of the Eigen form, H_3O^+ , or the Zundel form, $H_5O_2^+$, where the proton is bridged between two water molecules. In both areas of research, IR spectroscopy has been the dominant experimental tool; however, the interpretation of the measured spectra are a major challenge. This has been highlighted for the vibrations of H^+ ions embedded in molecular clusters^{176,183,184,185,186,187,188,189} and most recently for the $H^+(H_2O)_{21}$ cluster.¹⁹⁰

Acid clusters, such as hydrated HCl, arguably present even greater challenges for the interpretation of the IR spectrum than hydrated H^+ clusters, while still sharing aspects in common. The majority of experimental studies of hydrated HCl have focused on small $(HCl)_m(H_2O)_n$ clusters, in which HCl is not dissociated to an ion pair. Many of these cluster were discussed in the previous chapter.^{130,55,134,137,135,131,136,109,132,153,170}

From a number of independent theoretical studies, consensus has been reached that for $HCl(H_2O)_4$, among the several minima, the dissociated configuration, $H_3O^+(H_2O)_3 Cl^-$, is the most stable one.^{156,123,139,128,127,124} This configuration, shown in the inset

of Figure 5.1, is denoted as a solvent-ion-pair (SIP) conformation with C_3 symmetry. Numerous path integral and classical dynamical studies of this and larger ionized clusters have been reported.^{114,116,36,117,191} Experimental IR spectroscopy studies of the $HCl(H_2O)_4$ cluster in superfluid He nanodroplets at below 1 K reported evidence of the SIP, based on two spectral features at around 2670 cm^{-1} and theoretical support^{129,153} The peaks were assigned using scaled harmonic frequencies to the symmetric stretch of the H_3O^+ in two nearly isoenergetic SIP conformations.¹²⁹ However, the peak location and spectral line shape are nearly identical to those of the HCl stretch of the undissociated $(HCl)_2(H_2O)_2$ cluster.^{41,153} In addition, Møller-Plesset perturbation theory (MP2) harmonic calculations, the most sophisticated level of theory applied to the SIP to-date, obtain the symmetric stretch at $\sim 2900\text{ cm}^{-1}$, clearly in disagreement with the previous calculations.^{153,41} The theoretical reports of the SIP are summarized in Table 5.1. Furthermore, it is unclear whether the kinetic energy needed to surmount the barriers to transition from undissociated configurations to the SIP configuration are accessible in the helium droplets where experiments took place.¹⁹² Motivated by both the central importance of the $HCl(H_2O)_4$ cluster and the uncertainty in the experimental evidence for its dissociation, a calculation of the IR spectrum of the signature H_3O^+ ion in the SIP configuration was performed.

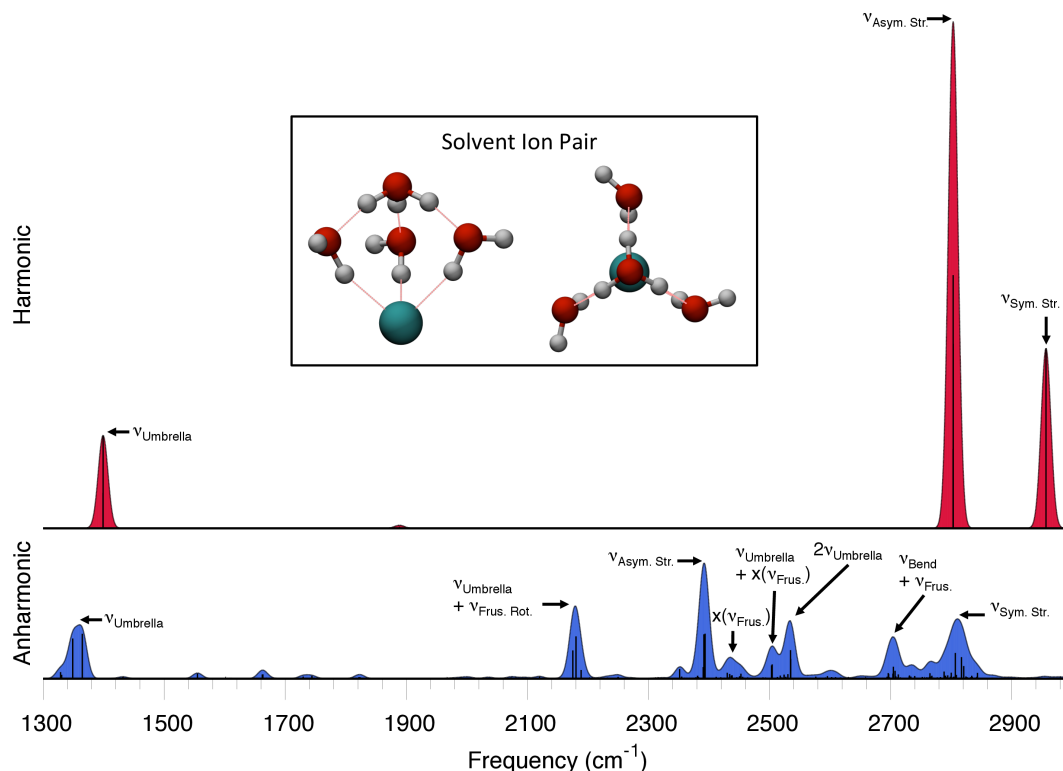


Figure 5.1: Global minimum SIP configuration from two perspectives and its embedded H_3O^+ harmonic and coupled anharmonic spectrum. Each stick represents an individual state with the band shapes produced from the convolution of a Gaussians. The intensities of the two spectra are unscaled.

Table 5.1: Summary of the SIP H_3O^+ harmonic stretch frequencies (cm^{-1}).

Theory	$\nu_{\text{Asym. Str.}}$	$\nu_{\text{Asym. Str.}}$	$\nu_{\text{Sym. Str.}}$
B3LYP/D9511(p,d) ¹²⁴	2600	2608	2786
MP2/6-311+G* ¹²³	2747	2747	2987
BLYP/aVTZ ¹²⁹	-	-	2708
MP2/6-311+(3df,3pd) ⁴¹	-	-	2921
RI-MP2/aVTZ ¹²⁹	-	-	2903
MP2/aVDZ	2649	2649	2880

5.2.2 THEORETICAL METHODS FOR THE STUDY OF $\text{H}_3\text{O}^+(\text{H}_2\text{O})_3\text{Cl}^-$

The SIP cluster, which has thirty-six vibrational degrees-of-freedom, is far too large for rigorous quantum calculations and so the Local Monomer approach (LMon) was used.^{48,87} This is the same approach that was applied successfully to the undissociated HCl clusters mentioned above.¹⁷⁰ In the application to $\text{HCl}(\text{H}_2\text{O})_4$, the LMon

approach is expanded to consider coupling among the twelve vibrational degrees-of-freedom (six intramolecular and six intermolecular) of H_3O^+ embedded in the $\text{H}_3\text{O}^+(\text{H}_2\text{O})_3 \text{Cl}^-$ cluster shown in Fig. 5.2. The calculations make use of an *ab initio*-based potential energy surface, built from the highest quality electronic structure methods feasible and coupled-anharmonic vibrational calculations.

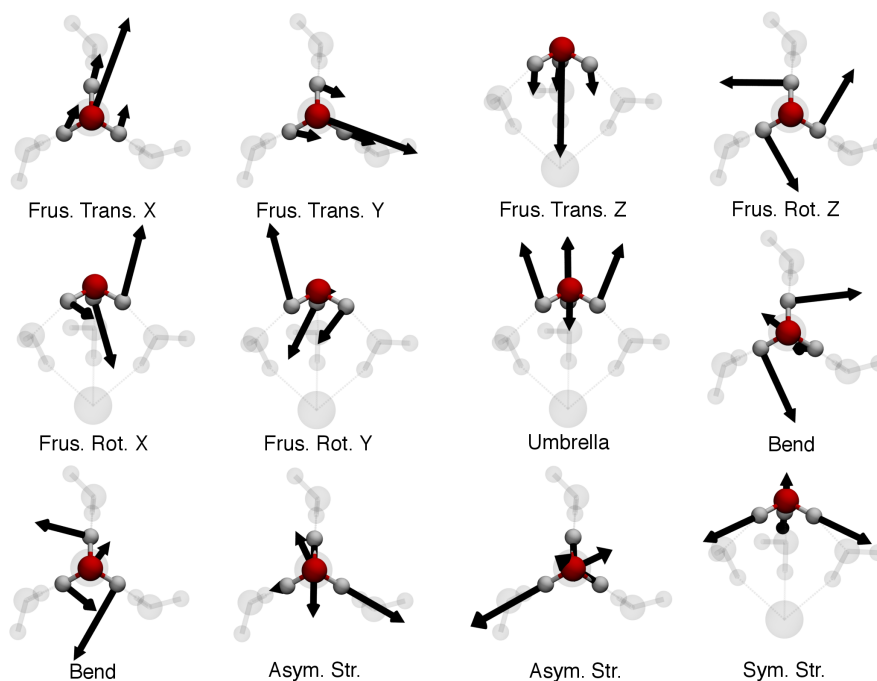


Figure 5.2: Representations of the 12 LMon eigenvectors for the H_3O^+ embedded in the SIP cluster. The first six modes refer to intermolecular motions and the last six intramolecular motions. The abbreviations used are Frus. = Frustrated, Trans. = Translation, Rot. = Rotation, Sym = Symmetric, Asym = Asymmetric, Str. = Stretch. The labels, X, Y, Z are used to refer to the relative axis of the mode, where the Z-axis passes through the Cl^- and the O of the H_3O^+ .

More specifically, the LMon potential energy surface (PES) describes the motion of H_3O^+ embedded in the SIP cluster, with fixed positions for the three H_2O monomers and the Cl^- . The equilibrium configuration of this cluster was determined by a full-dimensional geometry optimization, using Coupled Cluster Singles Doubles and Perturbative Triples excitations (CCSD(T)), explicit correlation (-F12)¹² and the augmented correlation consistent double zeta basis (aVDZ).¹³ At this configuration

the LMon PES is given by

$$V = V_{H_3O^+} + V_{H_3O^+Cl^-} + \sum_{i=1}^3 V_{H_3O^+H_2O(i)} + \sum_{i<j}^3 V_{H_2O(i)(H_3O^+)H_2O(j)} + \sum_{i=1}^3 V_{H_3O^+(Cl^-)H_2O(i)}, \quad (5.1)$$

where the terms are as follows. $V_{H_3O^+}$ is the potential of the isolated H_3O^+ monomer, which describes the six intramolecular vibrational degrees-of-freedom. $V_{H_3O^+Cl^-}$ is the twelve degree-of-freedom intrinsic two-body potential of H_3O^+ interacting with the fixed-position Cl^- , where the additional six degrees-of-freedom describe the H_3O^+ intermolecular modes. The meaning of the remaining terms in Eq. 5.1 follow the description of the $V_{H_3O^+Cl^-}$ and should be obvious. Each potential is a full-dimensional permutationally invariant linear-least squares fit to tens of thousands of electronic energies.^{3,193} The one- and two-body interaction energies used for the fits were computed using CCSD(T) with the augmented correlations consistent triple zeta (aVTZ) basis or higher. These levels of theory are not computationally feasible for the three-body interactions and so CCSD(T)-F12/aVDZ energies were used. The higher-body interactions are neglected in the LMon PES, as they contribute less than 1% of the total cluster interaction energy.¹²⁸

The newly developed LMon PES considered all one- two- and three-body H_3O^+ interactions. The contribution of each of interaction terms in the SIP are given in Table 5.2. The details of each of the interaction potentials included in the LMon PES are shown in Table 5.3. The $H_3O^+H_2O$ interaction energy and dipole moment were taken as the intrinsic interaction energy and dipole moments of a previously reported PES and DMS.⁹ All other interactions were taken from fits to a 5th order permutationally invariant polynomial with a basis of Morse like variables, $exp(-r_{ij}/\lambda)$, where r_{ij} are the intermolecular distances and the range parameter, λ , equals 2 bohr.³ For a given interaction, the same level of theory was used to compute all of the required monomer,

dimer and trimer energies. The points for the new potentials were taken from sections of the geometries which are sampled in the Multimode calculations. More specifically, the points are the displacements of one-, two-, three- and four-mode grids of the LMon modes of the CCSD(T)-F12a/aVDZ configuration. The fitting was done in an iterative fashion whereby addition points were added to the fitting data base until no significant changes were observed in the harmonic and anharmonic frequencies with respect to the addition of more points. The potentials were also tested using classical molecular dynamics and diffusion Monte Carlo simulations of the embedded H_3O^+ . The LMon DMS was formulated in a similar manner and contains all one- and two-body H_3O^+ dipole interactions computed using MP2/aVTZ. The details of each of the LMon DMS parts are shown in Table 5.4 These and all other reported *ab initio* calculations were performed using the electronic structure package MOLPRO 2010.⁷⁷

Table 5.2: Details of the SIP many-body interactions from CCSD(T)-F12/aVDZ.

Interaction	kcal	Percentage
$(H_3O)Cl$	-111.0	43.0
$H_3O(H_2O)$	-80.8	31.3
$(H_2O)Cl$	-39.6	15.4
$H_3O(H_2O)_2$	15.6	6.0
$(H_2O)_2Cl$	4.7	1.8
$(H_2O)_2$	2.7	1.1
$H_3O(H_2O)Cl$	1.7	0.7
4-body + 5-body	-1.5	0.6
$(H_2O)_3$	-0.4	0.1

Table 5.3: Details of the components of the PES surface's total number of points, fitting root-mean-squared-deviation (RMSD) and energy span.

Interaction	Method	Total Points	RMSD	Energy Span
H_3O^+	CCSD(T)-F12b/aVQZ	1601	9	19500
$H_3O^+Cl^-$	CCSD(T)-F12b/aVTZ	11307	10	13500
$H_3O^+H_2O$ ^[9]	CCSD(T)/aVTZ	48189	35	-
$H_3O^+(H_2O)Cl^-$	CCSD(T)-F12b/aVDZ	28073	9	9800
$H_3O^+(H_2O)_2$	CCSD(T)-F12b/aVTZ	21740	6	4200

Table 5.4: Details of the components of the DMS surface's total number of points and fitting root-mean-squared-deviation (RMSD).

Interaction	H_3O^+	$H_3O^+Cl^-$	$H_3O^+H_2O$ ^[9]
Total Points	1601	11307	48189
RMSD _x (a.u.)	0.0011	0.0061	0.0159
RMSD _y (a.u.)	0.0024	0.0017	0.0106
RMSD _z (a.u.)	0.0017	0.0014	0.0100

The code Multimode was used to obtain the embedded, 0 K, H_3O^+ IR spectrum employing the LMon PES and DMS.^{19,20} The Multimode basis was limited to those states having a total number of quantum less than or equal to eight with a maximum of eight quanta allowed in each modes.

The twelve-mode calculation reported here included a 4-mode representation of the potential. Changes in peak positions and intensities were progressively smaller moving from two- to three- and then four-mode representations, indicating the calculations had converged or were close to convergence. Due to the exponential increase in computation time, calculations involving five-mode or greater coupling could not be performed in a reasonable amount of time to further verify that twelve mode calculation was converged. Additional support for the convergence is provided by the results of a reduced dimensional calculations involving only the six highest frequency modes where five-mode coupled calculations were performed. The peak positions in these reduced dimensional calculations changed by less than 1 cm^{-1} when increased from four- to five-mode coupling.

Before discussing the IR spectrum, the numerical validation of the approach taken is presented. This is done by examining harmonic frequencies and double harmonic intensities computed for the SIP cluster using various methodologies; these are given in Table 5.5. First, to test the accuracy of the LMon approach, results from a full harmonic normal-mode analysis (thirty-six degrees-of-freedom) and a LMon harmonic normal-mode analysis, both performed using MP2/aVDZ, are given in columns one and two of Table 5.5. As seen, they are in good agreement with each other for the 12

LMon modes. The average percent difference between the full and LMon approach is 9%, with the six highest frequencies differing by no-more than a 1% on average. Similar agreement is observed for the intensities in the two approaches. While the values in this test were computed with MP2/aVDZ, similar differences between full and LMon results are to be expected for subsequent higher level calculations. A full dimensional normal-mode analysis using CCSD(T) was not feasible for this system, due to the huge computation time required. However, a LMon normal-mode analysis using CCSD(T)-F12/aVDZ was performed and the results are reported in column three of Table 5.5. Comparison of the *ab initio* to the LMon PES frequencies, shown in column four of Table 5.5, provide a semi-quantitative measure of the LMon PES quality. The comparison is not exact because of differences in the potentials and the configuration with which the analyses were applied. The LMon PES uses higher quality basis sets for the one- and two-body interactions, which constitute 90% of the total energy. Furthermore, the LMon PES lacks the unphysical effects of basis set superposition error, which are present in the direct calculation.¹⁹⁴ The differences in the direct *ab initio* and LMon PES energetics result in small (~ 0.01 Å) geometric differences in the minimum energy structure of the embedded H_3O^+ . The optimized structure parameters of H_3O^+ from the *ab initio* and LMon PES are reported in Table 5.6. The frequencies from the LMon PES values differ by less than 7% from the direct LMon CCSD(T)-F12/aVDZ calculations. While some of these differences may be the result of fitting errors or the lack of higher-body effects, they are more likely the results of a more accurate description of one and two-body interactions in the LMon PE. As a result, the LMon values can be considered the benchmark for this system.

Table 5.5: Harmonic frequencies (cm^{-1}) and normalized double harmonic intensities of the embedded H_3O^+ in the SIP configuration computed using the different approaches.

Modes	Full		Local		Local		Local	
	MP2/aVDZ Freq.	Inten.	MP2/aVDZ Freq.	Inten.	CCSD(T)-F12/aVDZ Freq.	Inten.	LMon PES Freq.	Inten.
Frust. Trans. X	328	14	238	3	236	3	228	0
Frust. Trans. Y	329	14	239	3	236	3	228	0
Frust. Trans. Z	392	1	306	1	305	1	303	0
Frust. Rot. Z	840	0	804	0	797	0	794	0
Frust. Rot. Y	979	6	873	0	890	0	913	0
Frust. Rot. X	979	6	874	0	891	0	913	0
Umbrella	1489	36	1469	23	1475	26	1399	37
Bend	1758	2	1748	2	1781	2	1889	1
Bend	1758	2	1749	2	1781	2	1889	1
Asym. Str.	2649	100	2665	100	2713	100	2803	100
Asym. Str.	2650	100	2667	100	2713	100	2803	100
Sym. Str.	2880	76	2881	50	2960	48	2957	71

Table 5.6: Properties of the embedded H_3O^+ in the SIP configuration. Distances are reported in Ångstroms and angles in degrees.

Coordinate	LMon PES	CCSD(T)-F12/aVDZ
OH-Bonds	1.018	1.020
Hydrogen-Bonds	1.550	1.538
Umbrella Angle	105.0	104.1
$O \cdots Cl$	3.541	3.535

5.2.3 IR SPECTRUM OF $H_3O^+(H_2O)_3CL^-$

The harmonic and coupled anharmonic IR spectra are shown in Fig. 5.1. In both spectra, the individual vibrational states are represented by sticks. Each stick was broadened with a Gaussian function of width 8 cm^{-1} to generate vibrational band shapes. Before discussing the greatly contrasting results, it is worth mentioning that the harmonic spectrum was computed nearly instantaneously, requiring less than 300 evaluations of the LMon PES and the set-up and diagonalization of a 12×12 Hessian matrix. The calculation of the anharmonic spectrum required over a week of CPU time running serial on a workstation, with over five-million evaluations of the LMon PES and the set-up and diagonalization of the 26496×26496 VCI Hamiltonian matrix. This dichotomy in computational cost is mirrored in the resulting spectra. The harmonic spectrum is very simple, with only four harmonic states contributing to three significant features. In the anharmonic spectrum there are 206 IR active states from which eight individual Gaussian peaks were assigned. The eight peaks

all have intensity greater than at least 10% of the largest Gaussian feature. Clearly the harmonic approximation is not suitable for characterizing the complexity of the embedded H_3O^+ . The harmonic results in addition to failing to account for most of the H_3O^+ vibrational states, significantly overestimates the IR intensities of the features. The most intense anharmonic peak (891 km/mol) is less than a quarter of the harmonic spectrum's (3898 km/mol) most intense peak. Another interpretation of this "overestimation" of the intensities is that coupling "splinters" these large single peaks into many smaller dispersed ones. This is a common feature of complex spectra.¹⁹⁵

In the anharmonic-coupled spectrum, each of the VCI state wavefunctions is heavily mixed, that is to say no single stick corresponds to "pure" fundamental or overtone. In vibrational calculations with a small level of mode mixing VCI states are characterized by predominately one VSCF state with the square of the its respective coefficient equaling between 0.8 and 0.9 (where 1.0 would indicate completely pure state). The highly mixed VCI states are, however, characterized by dominate squared coefficients equaling less 0.5. Due to the heavy state mixing and the large (206) number of observed IR active states, the convoluted Gaussian bands of the spectra were assigned based on the contribution of virtual VSCF states in the band. In this approach, the ranges of each Gaussian peak whose intensities were greater than 10% of the most intense Gaussian peak were first identified. The coefficients of each VCI state in the Gaussian peak were squared, scaled by the VCI state's intensity and then summed over all VCI states. The analysis gives a qualitative picture of the contribution of each independent VSCF virtual state over the range of several VCI states that form the Gaussian peaks. The results of this analysis for VSCF virtual states, which contribute at least 50% of the largest virtual state coefficients are shown in Table 5.7 for the eight reported peaks. It is of note that in the case of the asymmetric stretch peak the sum of the two degenerate VCI states has the largest contribution in the associated band.

This analysis is complemented by comparing the peak positions to those computed by a separate, reduced-dimensional, calculation that involved only the six-highest frequency modes of the H_3O^+ . The result of the analysis of the eight spectral features is provided in Table 5.8, where the labels used in the Fig. 5.1 have been expanded upon.

Table 5.7: Results of weighted virtual state analysis for the twelve-mode H_3O^+ in the SIP configuration four-mode coupled spectra. Each band is labeled along with the number of IR active VCI states in the band. All states whose weighted coefficients are within 50% of the largest state's coefficient are shown for each respective bands. The percent of the largest virtual VSCF state are given, followed by the respective state. The twelve integers listed in each virtual VSCF state are the excitations from the ground state where each sequential number refers to respective harmonic mode.

5 States in 1300.0 - 1400.0
100.0 < 0 0 0 0 0 0 1 0 0 0 0 0 >

13 States in 2150.0 - 2220.0
100.0 < 0 0 0 0 1 0 1 0 0 0 0 0 >
55.87 < 0 0 0 0 0 1 1 0 0 0 0 0 >

21 States in 2370.0 - 2415.0
100.0 < 4 0 0 0 0 0 1 0 0 0 0 0 >
82.36 < 0 0 0 0 0 0 0 0 0 1 0 0 >
71.03 < 0 0 0 0 0 0 0 0 0 0 1 0 >

19 States in 2415.0 - 2473.0
100.0 < 0 0 0 2 1 0 0 0 0 0 0 0 >
97.70 < 0 0 0 2 0 1 0 0 0 0 0 0 >
64.67 < 1 0 1 0 2 0 0 0 0 0 0 0 >
64.13 < 1 1 0 0 1 1 0 0 0 0 0 0 >
62.69 < 1 1 3 0 0 1 0 0 0 0 0 0 >
60.63 < 1 0 1 0 0 2 0 0 0 0 0 0 >
58.91 < 0 1 1 0 0 2 0 0 0 0 0 0 >
51.52 < 0 1 1 0 2 0 0 0 0 0 0 0 >
50.66 < 1 1 3 0 1 0 0 0 0 0 0 0 >

15 States in 2480.0 - 2515.0
100.0 < 0 1 0 0 0 1 1 0 0 0 0 0 >
99.68 < 0 1 0 0 1 0 1 0 0 0 0 0 >
93.88 < 1 0 0 0 1 0 1 0 0 0 0 0 >
87.29 < 1 0 0 0 0 1 1 0 0 0 0 0 >
67.88 < 0 1 0 1 0 0 1 0 0 0 0 0 >
58.06 < 1 0 0 1 0 0 1 0 0 0 0 0 >
52.19 < 0 0 0 1 0 0 0 0 1 0 0 0 >

24 States in 2515.0 - 2560.0
100.0 < 0 0 0 0 0 0 2 0 0 0 0 0 >
84.20 < 0 0 0 0 0 0 0 0 0 0 0 1 >

50 States in 2680.0 - 2750.0
100.0 < 0 0 0 0 0 1 0 1 0 0 0 0 >
94.71 < 0 0 0 1 0 0 0 1 0 0 0 0 >
92.52 < 0 0 0 0 1 0 0 0 1 0 0 0 >
81.71 < 1 2 0 0 1 1 0 0 0 0 0 0 >
77.29 < 0 1 2 0 0 0 0 1 0 0 0 0 >
70.26 < 4 0 2 0 0 1 0 0 0 0 0 0 >
51.14 < 0 0 0 0 1 0 0 1 0 0 0 0 >

76 States in 2750.0 - 2860.0
100.0 < 0 0 0 0 0 0 0 0 0 0 0 1 >
70.05 < 1 0 0 2 1 0 0 0 0 0 0 0 >
53.89 < 0 4 0 0 0 0 0 1 0 0 0 0 >
53.73 < 0 1 0 2 0 1 0 0 0 0 0 0 >
50.18 < 0 0 0 0 0 0 2 0 0 0 0 0 >

Table 5.8: Quantum deconstruction of the IR spectrum of the SIP embedded H_3O^+ . The sections *Reduced* and *Complete* refer to the results of the reduced-dimensional six-highest-frequency-mode coupled calculation and the full twelve-mode coupled calculation, respectively. The frequencies are reported in cm^{-1} and the intensities in normalized units. The column “# of States” indicates the number of VCI states in the band range

Vibration	<i>Reduced</i>		<i>Complete</i>		
	Peak	Peak	Band Range	Intensity	# of States
Umbrella	1367	1357	1300 - 1400	46	5
Umbrella + Frus. Rot. X/Y	-	2179	2150 - 2220	63	13
Asym. Str.	2458	2391	2370 - 2415	100	21
2 · Frus. Rot. Z + Frus. Rot. X/Y	-	2435	2415 - 2473	18	19
Umbrella + Frus. Tran. X/Y + Frus. Rot. X/Y	-	2500	2480 - 2515	25	15
2 · Umbrella	2569	2531	2515 - 2560	50	24
Bend + Frus. Rot.	-	2704	2680 - 2750	36	50
Sym. Str.	2778	2811	2750 - 2860	52	76

Numerous features in the VCI spectrum correspond to overtones and combination bands of the frustrated modes and umbrella motion which cannot be described using the standard double-harmonic approach. Many of these features, notably the band spanning $2415 - 2473$ cm^{-1} , are characterized by several states that individually have small IR intensity. When the Gaussian convolution of these states with their neighbors is considered, bands with appreciable intensity are observed. The features, predominately in the range $2370 - 2860$ cm^{-1} result from interactions among the stretching modes which lead to significant intensity sharing. The intensity sharing between the symmetric stretch and umbrella overtone is of particular note. In the VCI state analysis a Fermi resonance is observed between the symmetric stretch and umbrella overtone resulting in significant transfer of intensity from the symmetric stretch to the overtone. Outside the heavily mixed $2415 - 2473$ cm^{-1} region there are two well defined peaks associated with the fundamental of the umbrella motion and combination bands of the umbrella + frustrated rotation.

Clearly, the spectral features of the SIP spectrum are complex, even after isolating the H_3O^+ features. Additional spectral features associated with the higher energy conformer of the SIP could also contribute to the observed experimental spectrum.¹²⁹ This alternate configuration is ~ 200 cm^{-1} higher in energy and characterized by the rotation of one of the H_2O monomer’s free OHs into a non-symmetric position. LMon CCSD(T)-F12/aVDZ harmonic stretch frequencies of this conformer shift as much as

47 cm^{-1} from the lower energy SIP conformation. While transitions between the higher energy structure and the ground state are unlikely, as a $\sim 400\text{ cm}^{-1}$ barrier must first be crossed, its formation in experimental studies alongside the lowest energy structure, could be possibility. Fortuitously, these features are outside the bulk of SIP H_3O^+ spectral signature. However, they do coincide with the H_3O^+ combination bands of the umbrella + frustrated rotation. A visualization of this alternate configuration and its harmonic frequencies are reported in the Figure 5.3 and Table 5.9.

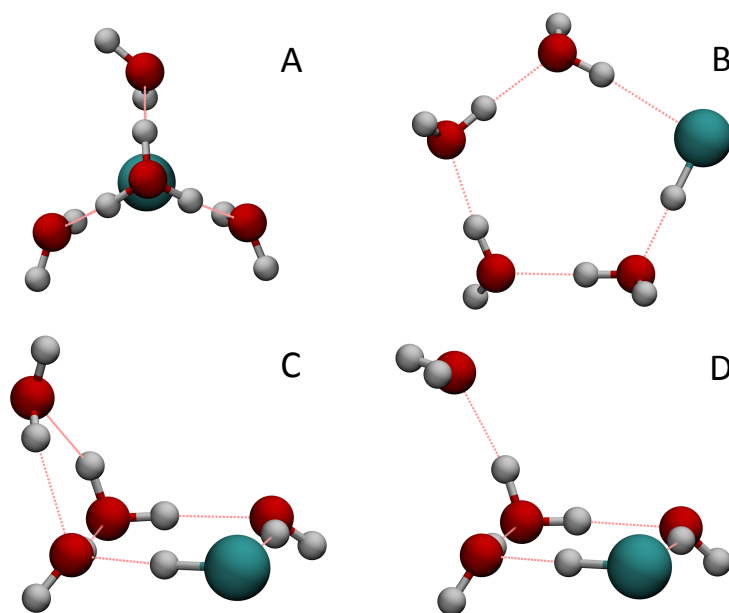


Figure 5.3: Higher energy local minima of the SIP and unionized $HCl(H_2O)_4$ cluster: (A), non-symmetric higher energy SIP cluster; (B), five-membered ring configuration; (C), four-member ring with water monomer accepting and donating a hydrogen bond to the ring; and (D) four-member ring with water monomer accepting a hydrogen bond from the ring.

Table 5.9: CCSD(T)-F12/aVDZ local harmonic frequencies (cm^{-1}) for the SIP cluster in the alternate non-symmetric conformation.

Mode	Frequency
Frust. Trans. X	221
Frust. Trans. Y	243
Frust. Trans. Z	305
Frust. Rot. Z	769
Frust. Rot. Y	873
Frust. Rot. X	922
Umbrella	1470
Bend	1763
Bend	1793
Stretch	2683
Stretch	2757
Stretch	2969

There are three other minima of note for the $HCl(H_2O)_4$ cluster which include undissociated HCl monomers. These three structures include a $HCl(H_2O)_3$ ring with a fourth water monomer accepting a single hydrogen-bond from the ring, a similar structure where the fourth water monomer donates and accepts a hydrogen-bond from the ring and a five-member ring. These structures were studied using the many-body potential described in Chapter 4. Visualizations of these structures are provided in Figure 5.3. The energies of these configurations relative to the SIP configuration (kcal) and their respective LMon HCl anharmonic frequencies (cm^{-1}) are: 6.0, 2093; 4.6, 2220; and 3.0, 2161. These HCl fundamental excitations are quite pure and so do not display the splintering that characterizes the embedded H_3O^+ spectrum. Thus, spectral features associated with these are at down-shifted from the main portion of the IR region of the SIP complex.

The complexity and diffuse nature of the H_3O^+ vibrational spectrum embedded in the SIP is likely not limited to this “smallest droplet of acid” but also occurs for embedded H_3O^+ in other systems. For example, both the $H^+(H_2O)_{21}$ and $H^+(H_2O)_4$ clusters broad spectra peaks were associated with embedded H_3O^+ . The broad nature of these features are of note, considering they were performed at very cold temper-

atures. A possible explanation for this is the same anharmonic effects which cause the broad feature in the SIP cluster also occur for these systems as well. This, combined with delocalization of the free OH of the water monomers in these non-counter ion systems could result in reported line shapes. Further merit for this comparison comes from the report of a umbrella + frustrated rotation combination band in the $H^+(H_2O)_{21}$ similar to that reported here.¹⁸⁶

5.2.4 SUMMARY AND CONCLUSIONS

In summary, a calculation of the IR spectrum for the solvent-ion-pair conformation of $HCl(H_2O)_4$ in a fashion that isolates the contribution from the signature hydronium ion, H_3O^+ . The computed spectrum indicates that the vibrational states of the H_3O^+ are highly mixed, resulting in dispersed spectral features between 1300 and 3000 cm^{-1} , with the region between 2100 and 2900 cm^{-1} being especially rich. These predictions point out the complexity of the SIP spectrum and offer guidelines for experiment.

References

- [1] Atkins, R., Peter; Friedman *Molecular Quantum Mechanics*, 4th ed.; Oxford University Press: New York, 2005.
- [2] Cramer, C. *Essentials of Computational Chemistry*; John Wiley and Sons Ltd: England, 2004.
- [3] Braams, B. J.; Bowman, J. M. *Int. Rev. Phys. Chem.* **2009**, *28*.
- [4] Yang, K. R.; Xu, X.; Truhlar, D. G. *Chem. Phys. Lett.* **2013**, *573*, 84.
- [5] Behler, J. *Phys. Chem. Chem. Phys.* **2011**, *13*, 17930.
- [6] Lee, T. J.; Martin, J. M. L.; Taylor, P. R. *J. Chem. Phys.* **1995**, *102*, 254.
- [7] Babin, V.; Medders, G. R.; Paesani, F. *J. Chem. Theo. Comp.* **2014**, *10*, 1599.
- [8] Wang, Y.; Shepler, B. C.; Braams, B. J.; Bowman, J. M. *J. Chem. Phys.* **2009**, *131*, 054511.
- [9] Huang, X.; Braams, B. J.; Bowman, J. M. *J. Chem. Phys.* **2005**, *122*, 44308.
- [10] Beran, G. J. O. *J. Chem. Phys.* **2009**, *130*, 164115.
- [11] Wang, Y.; Huang, X.; Shepler, B. C.; Braams, B. J.; Bowman, J. M. *J. Chem. Phys.* **2011**, *134*, 094509.
- [12] Knizia, G.; Adler, T. B.; Werner, H.-J. *J. Chem. Phys.* **2009**, *130*.
- [13] Dunning, T. H. *J. Chem. Phys.* **1989**, *90*, 1007.
- [14] William H. Press, W. T. V., Saul A. Teukolsky; Flannery, B. P. *Numerical Recipes Numerical Recipes in Fortran 77*, 2nd ed.; Cambridge University Press, 1986.
- [15] Akima, H. *ACM Trans. Math. Softw.* **1978**, *4*, 148.
- [16] Akima, H. *Rocky Mountain J. Math.* **1984**, *14*.
- [17] Barone, V. *J. Chem. Phys.* **2005**, *122*, 14108.
- [18] Ramírez, R.; López-Ciudad, T.; Kumar P, P.; Marx, D. *J. Chem. Phys.* **2004**, *121*, 3973.

- [19] Stuart Carter, N. C. H., Joel M. Bowman *Theor. Chem. Acc.* **1998**, *100*, 191.
- [20] Joel M. Bowman, S. C.; Huang, X. *Int. Rev. Phys. Chem.* **2003**, *22*, 533.
- [21] Bowman, J. M.; Carrington, T.; Meyer, H.-D. *Mol. Phys.* **2008**, *106*, 2145.
- [22] Carter, S.; Sharma, A. R.; Bowman, J. M.; Rosmus, P.; Tarroni, R. *J. Chem. Phys.* **2009**, *131*, 224106.
- [23] Colbert, D. T.; Miller, W. H. *J. Chem. Phys.* **1992**, *96*, 1982.
- [24] Schroder, M.; Gatti, F.; Meyer, H. D. *J. Chem. Phys.* **2011**, *134*, 234307.
- [25] Hammer, T.; Manthe, U. *J. Chem. Phys.* **2011**, *134*, 224305.
- [26] Wang, Y.; Braams, B. J.; Bowman, J. M.; Carter, S.; Tew, D. P. *J. Chem. Phys.* **2008**, *128*, 224314.
- [27] Bramley, M. J.; Carrington, T. *J. Chem. Phys.* **1993**, *99*, 8519.
- [28] Thomas, M.; Brehm, M.; Fligg, R.; Vohringer, P.; Kirchner, B. *Phys. Chem. Chem. Phys.* **2013**, *15*, 6608.
- [29] Ioan Kosztin, B. F.; Schulten, K. *Am. J. Phys.* **1996**, *64*, 633.
- [30] McCoy, A. B. *Int. Rev. Phys. Chem.* **2006**, *25*, 77.
- [31] Wang, Y.; Babin, V.; Bowman, J. M.; Paesani, F. *J. Am. Chem. Soc.* **2012**, *134*, 11116.
- [32] Czako, G.; Wang, Y.; Bowman, J. M. *J. Chem. Phys.* **2011**, *135*, 151102.
- [33] Hase, W. L. *Classical Trajectory Simulations, in Encyclopedia of Computational Chemistry*; Wiley, 2002; Vol. 5.
- [34] Habershon, S.; Manolopoulos, D.; Markland, T.; Miller III, T. *Annu. Rev. Phys. Chem.* **2013**, *64*, 387.
- [35] Marx, D.; Parrinello, M. *J. Chem. Phys.* **1996**, *104*, 4077.
- [36] Walewski, L.; Forbert, H.; Marx, D. *ChemPhysChem* **2013**, *14*, 817.
- [37] Wang, F.; Deible, M.; Jordan, K. D. *J. Phys. Chem. A* **2013**, *117*, 7606.
- [38] Kazachenko, S.; Bulusu, S.; Thakkar, A. J. *J. Chem. Phys.* **2013**, *138*, 224303.
- [39] Nedic, M.; Wassermann, T. N.; Larsen, R. W.; Suhm, M. A. *Phys. Chem. Chem. Phys.* **2011**, *13*, 14050.
- [40] Morrison, A. M.; Flynn, S. D.; Liang, T.; Douberly, G. E. *J. Phys. Chem. A* **2010**, *114*, 8090.

- [41] Flynn, S. D.; Skvortsov, D.; Morrison, A. M.; Liang, T.; Choi, M. Y.; Doublerly, G. E.; Vilesov, A. F. *J. Phys. Chem. Lett.* **2010**, *1*, 2233.
- [42] Mahadevi, A. S.; Neela, Y. I.; Sastry, G. N. *Phys. Chem. Chem. Phys.* **2011**, *13*, 15211.
- [43] Yang, S.; Ellis, A. M. *Chem. Soc. Rev.* **2013**, *42*, 472.
- [44] Häber, T.; Schmitt, U.; Emmeluth, C.; Suhm, M. A. *Faraday Discuss.* **2001**, *118*, 331.
- [45] Merrick, J. P.; Moran, D.; Radom, L. *J. Phys. Chem. A* **2007**, *111*, 11683.
- [46] Scott, A. P.; Radom, L. *J. Phys. Chem.* **1996**, *100*, 16502.
- [47] Wang, Y.; Bowman, J. M. *J. Chem. Phys. Lett.* **2013**, *4*, 1104.
- [48] Wang, Y.; Bowman, J. M. *J. Chem. Phys.* **2011**, *134*, 154510.
- [49] Liu, H.; Wang, Y.; Bowman, J. M. *J. Phys. Chem. Lett.* **2012**, *3*, 3671.
- [50] Kamarchik, E.; Bowman, J. M. *J. Phys. Chem. A* **2010**, *114*, 12945.
- [51] Kamarchik, E.; Wang, Y.; Bowman, J. M. *J. Chem. Phys.* **2011**, *134*, 114311.
- [52] Kamarchik, E.; Toffoli, D.; Christiansen, O.; Bowman, J. M. *Spectrochim. Acta. A Mol. Biomol. Spectrosc, In Press* **2014**, *119*, 59.
- [53] Wang, Y.; Bowman, J. M. *J. Chem. Phys.* **2012**, *136*, 144113.
- [54] Manzhos, S.; Chan, M.; Carrington, T. *J. Chem. Phys.* **2013**, *139*, 051101.
- [55] Ortlieb, M.; Birer, O.; Letzner, M.; Schwaab, G. W.; Havenith, M. *J. Phys. Chem. A* **2007**, *111*, 12192.
- [56] Skvortsov, D.; Sliter, R.; Choi, M. Y.; Vilesov, A. F. *J. Chem. Phys.* **2008**, *128*, 094308.
- [57] Jiang, H.; Sarsa, A.; Murdachaew, G.; Szalewicz, K.; Bačić, Z. *J. Chem. Phys.* **2005**, *123*, 224313.
- [58] Vissers, G. W.; Oudejans, L.; Miller, R. E.; Groenenboom, G. C.; van der Avoird, A. *J. Chem. Phys.* **2004**, *120*, 9487.
- [59] Fárník, M.; Davis, S.; Nesbitt, D. J. *Faraday Discuss.* **2001**, *118*, 63.
- [60] Schuder, M. D.; Lovejoy, C. M.; Lascola, R.; Nesbitt, D. J. *J. Chem. Phys.* **1993**, *99*, 4346.
- [61] Schuder, M. D.; Lovejoy, C. M.; Nelson, D. D.; Nesbitt, D. J. *J. Chem. Phys.* **1989**, *91*, 4418.

- [62] Furlan, A.; Wülfert, S.; Leutwyler, S. *Chem. Phys. Lett.* **1988**, *153*, 291.
- [63] Qiu, Y.; Zhang, J. Z. H.; Bačić, Z. *J. Chem. Phys.* **1998**, *108*, 4804.
- [64] Qiu, Y.; Bačić, Z. *J. Chem. Phys.* **1997**, *106*, 2158.
- [65] Elrod, M. J.; Saykally, R. J. *J. Chem. Phys.* **1995**, *103*, 921.
- [66] Elrod, M. J.; Saykally, R. J. *J. Chem. Phys.* **1995**, *103*, 933.
- [67] Gomez, P. C.; Bunker, P. R. *J. Mol. Spectrosc.* **1994**, *168*, 507.
- [68] Karpfen, A.; Bunker, P. R.; Jensen, P. *Chem. Phys.* **1991**, *149*, 299–309.
- [69] Althorpe, S. C.; Clary, D. C.; Bunker, P. R. *Chem. Phys. Lett.* **1991**, *187*, 345.
- [70] Skvortsov, D.; Choi, M. Y.; Vilesov, A. F. *J. Phys. Chem. A* **2007**, *111*, 12711.
- [71] Fárník, M.; Nesbitt, D. J. *J. Chem. Phys.* **2004**, *121*, 12386.
- [72] van der Veken, B. J.; De Munck, F. R. *J. Chem. Phys.* **1992**, *97*, 3060.
- [73] Engdahl, A.; Nelander, B. *J. Phys. Chem.* **1990**, *94*, 8777.
- [74] Chalasinski, G.; Cybulski, S. M.; Szczesniak, M. M.; Scheiner, S. *J. Chem. Phys.* **1989**, *91*, 7048.
- [75] Latajka, Z.; Scheiner, S. *Chem. Phys.* **1997**, *216*, 37–52.
- [76] Haber, T.; Schmitt, U.; Suhm, M. A. *Phys. Chem. Chem. Phys.* **1999**, *1*, 5573.
- [77] *H.-J. Werner, P. J. Knowles, G. Knizia et al., MOLPRO, Version 2010.1, a package of ab initio programs, see <http://www.molpro.net> H.-J. Werner, P. J. Knowles, G. Knizia et al., MOLPRO, Version 2010.1, a package of ab initio programs, see <http://www.molpro.net>*
- [78] Coxon, J. A.; Hajigeorgiou, P. G. *J. Mol. Spectrosc.* **2000**, *203*, 49.
- [79] Xiao-Niu, Z.; De-Heng, S.; Jin-Ping, Z.; Zun-Lüe, Z.; Jin-Feng, S. *Chin. Phys. B* **2010**, *19*, 053401.
- [80] Kasha, M. *Radiat. Res.* **1963**, *20*, 55.
- [81] Fárník, M.; Davis, S.; Nesbitt, D. J. *J. Chem. Phys.* **2003**, *118*, 10137.
- [82] Ni, H.; Serafin, J. M.; Valentini, J. J. *J. Chem. Phys.* **2000**, *113*, 3055.
- [83] McCoy, A. B.; Braams, B. J.; Brown, A.; Huang, X.; Jin, Z.; Bowman, J. M. *J. Phys. Chem. A* **2004**, *108*, 4991.
- [84] Jin, Z.; Braams, B. J.; Bowman, J. M. *J. Phys. Chem. A* **2006**, *110*, 1569.

- [85] Rauk, A.; Armstrong, D. A. *EPJ D* **2005**, *35*, 217.
- [86] Han, J.; Wang, Z.; McIntosh, A. L.; Lucchese, R. R.; Bevan, J. W. *J. Chem. Phys.* **1994**, *100*, 7101.
- [87] Mancini, J. S.; Bowman, J. M. *J. Chem. Phys.* **2013**, *139*, 164115.
- [88] Miller, W. H. *J. Chem. Phys.* **2012**, *136*, 210901.
- [89] Skvortsov, D.; Sliter, R.; Choi, M. Y.; Vilesov, A. F. *J. Chem. Phys.* **2008**, *128*, 094308.
- [90] Fárník, M.; Davis, S.; Schuder, M. D.; Nesbitt, D. J. *J. Chem. Phys.* **2002**, *116*, 6132.
- [91] Watson, J.; Crick, F. *Nature* **1953**, *171*, 737.
- [92] Ludwig, R. *Angew. Chem. Int. Ed.* **2001**, *40*, 1808.
- [93] Moore, T. S.; Winmill, T. F. *J. Chem. Soc., Trans.* **1912**, *101*, 1635.
- [94] Pimentel, G. C. *Hydrogen Bond*; W.H.Freeman and Co Ltd, 1960.
- [95] Scheiner, S. *Hydrogen Bonding: A Theoretical Perspective*; Oxford University Press, USA, 1997.
- [96] Zhang, J.; Chen, P.; Yuan, B.; Ji, W.; Cheng, Z.; Qiu, X. *Science* **2013**, *342*, 611.
- [97] Rocher-Casterline, B. E.; Mollner, A. K.; Ch'ng, L. C.; Reisler, H. *J. Phys. Chem. A* **2011**, *115*, 6903.
- [98] Casterline, B. E.; Mollner, A. K.; Ch'ng, L. C.; Reisler, H. *J. Phys. Chem. A* **2010**, *114*, 9774.
- [99] Mollner, A. K.; Casterline, B. E.; Ch'ng, L. C.; Reisler, H. *J. Phys. Chem. A* **2009**, *113*, 10174.
- [100] Reisler, H. *Annu. Rev. Phys. Chem.* **2009**, *60*, 39.
- [101] Rocher-Casterline, B. E.; Ch'ng, L. C.; Mollner, A. K.; Reisler, H. *J. Chem. Phys.* **2011**, *134*, 211101.
- [102] Ch'ng, L. C.; Samanta, A. K.; Czako, G.; Bowman, J. M.; Reisler, H. *J. Am. Chem. Soc.* **2012**, *134*, 15430.
- [103] Samanta, A. K.; Ch'ng, L. C.; Reisler, H. *Chem. Phys. Lett.* **2013**, *575*, 1.
- [104] Pine, A. S. *J. Chem. Phys.* **1983**, *78*, 2154.
- [105] Michael, D. W.; Lisy, J. M. *J. Chem. Phys.* **1986**, *85*, 2528.

- [106] Case, A. S.; Heid, C. G.; Western, C. M.; Crim, F. F. *J. Chem. Phys.* **2012**, *136*, 124310.
- [107] Keutsch, F. N.; Cruzan, J. D.; Saykally, R. J. *Chem. Rev.* **2003**, *103*, 2533.
- [108] Quack, M.; Stohner, J.; Suhm, M. A. *J. Mol. Struct.* **2001**, *599*, 381.
- [109] Fárník, M.; Weimann, M.; Suhm, M. A. *J. Chem. Phys.* **2003**, *118*, 10120.
- [110] Ch'ng, L. C.; Samanta, A. K.; Wang, Y.; Bowman, J. M.; Reisler, H. *J. Phys. Chem. A* **2013**, *117*, 7207.
- [111] Ayotte, P.; Marchand, P.; Daschbach, J. L.; Smith, R. S.; Kay, B. D. *J. Phys. Chem. A* **2011**, *115*, 6002.
- [112] Brastad, S. M.; Nathanson, G. M. *Phys. Chem. Chem. Phys.* **2011**, *13*, 8284.
- [113] Boese, A. D.; Forbert, H.; Masia, M.; Tekin, A.; Marx, D.; Jansen, G. *Phys. Chem. Chem. Phys.* **2011**, *13*, 14550.
- [114] Forbert, H.; Masia, M.; Kaczmarek-Kedziera, A.; Nair, N. N.; Marx, D. *J. Am. Chem. Soc.* **2011**, *133*, 4062.
- [115] Oncak, M.; Slavicek, P.; Farnik, M.; Buck, U. *J. Phys. Chem. A* **2011**, *115*, 6155.
- [116] Sugawara, S.; Yoshikawa, T.; Takayanagi, T.; Tachikawa, M. *Chem. Phys. Lett.* **2011**, *501*, 238.
- [117] Walewski, Ł.; Forbert, H.; Marx, D. *J. Phys. Chem. Lett.* **2011**, *2*, 3069.
- [118] Talukdar, R. K.; Burkholder, J. B.; Roberts, J. M.; Portmann, R. W.; Ravishankara, A. R. *J. Phys. Chem. A* **2012**, *116*, 6003.
- [119] Bianco, R.; Hynes, J. T. *Acc. Chem. Res.* **2006**, *39*, 159.
- [120] Tolbert, M.; Rossi, M.; Golden, D. *Science* **1988**, *240*, 1018.
- [121] Molina, M. J.; Tso, T. L.; Molina, L. T.; Wang, F. C. *Science* **1987**, *238*, 1253.
- [122] Lee, C. T.; Sosa, C.; Planas, M.; Novoa, J. J. *J. Chem. Phys.* **1996**, *104*, 7081.
- [123] Bacelo, D. E.; Binning, R. C.; Ishikawa, Y. *J. Phys. Chem. A* **1999**, *103*, 4631.
- [124] Re, S.; Osamura, Y.; Suzuki, Y.; Schaefer, H. F. *J. Chem. Phys.* **1998**, *109*, 973.
- [125] Chaban, G. M.; Gerber, R. B.; Janda, K. C. *J. Phys. Chem. A* **2001**, *105*, 8323.
- [126] Masia, M.; Forbert, H.; Marx, D. *J. Phys. Chem. A* **2007**, *111*, 12181.

- [127] Odde, S.; Mhin, B. J.; Lee, S.; Lee, H. M.; Kim, K. S. *J. Chem. Phys.* **2004**, *120*, 9524.
- [128] Milet, A.; Struniewicz, C.; Moszynski, R.; Wormer, P. E. S. *J. Chem. Phys.* **2001**, *115*, 349.
- [129] Gutberlet, A.; Schwaab, G.; Birer, O.; Masia, M.; Kaczmarek, A.; Forbert, H.; Havenith, M.; Marx, D. *Science* **2009**, *324*, 1545.
- [130] Kisiel, Z.; Pietrewicz, B. A.; Fowler, P. W.; Legon, A. C.; Steiner, E. *J. Phys. Chem. A* **2000**, *104*, 6970.
- [131] Legon, A. C.; Willoughby, L. C. *Chem. Phys. Lett.* **1983**, *95*, 449.
- [132] Weimann, M.; Fárník, M.; Suhm, M. A. *Phys. Chem. Chem. Phys.* **2002**, *4*, 3933.
- [133] Huneycutt, A. J.; Stickland, R. J.; Hellberg, F.; Saykally, R. J. *J. Chem. Phys.* **2003**, *118*, 1221.
- [134] Ault, B. S.; Pimentel, G. C. *J. Phys. Chem.* **1973**, *77*, 57.
- [135] Barnes, A. J. *J. Mol. Str.* **1980**, *60*, 343.
- [136] Amirand, C.; Maillard, D. *J. Mol. Str.* **1988**, *176*, 181.
- [137] Schriver, A.; Silvi, B.; Maillard, D.; Perchard, J. P. *J. Phys. Chem.* **1977**, *81*, 2095.
- [138] Ayers, G. P.; Pullin, A. D. E. *Spectrochim. Acta. A* **1976**, *32*, 1641.
- [139] Cabaleiro-Lago, E. M.; Hermida-Ramón, J. M.; Rodriguez-Otero, J. *J. Chem. Phys.* **2002**, *117*, 3160.
- [140] Packer, M. J.; Clary, D. C. *J. Phys. Chem.* **1995**, *99*, 14323.
- [141] Alikhani, M. E.; Silvi, B. *Phys. Chem. Chem. Phys.* **2003**, *5*, 2494.
- [142] de Tudela, R. P.; Barragan, P.; Prosmi, R.; Villarreal, P.; Delgado-Barrio, G. *J. Phys. Chem. A* **2011**, *115*, 2483.
- [143] Acioli, P. H.; Xie, Z.; Braams, B. J.; Bowman, J. M. *J. Chem. Phys.* **2008**, *128*, 104318.
- [144] Tuckerman, M. E. *Science* **1997**, *275*, 817.
- [145] Skvortsov, D.; Lee, S. J.; Choi, M. Y.; Vilesov, A. F. *J. Phys. Chem. A* **2009**, *113*, 7360.
- [146] Boys, S. F.; Bernardi, F. *Mol. Phys.* **1970**, *19*, 553.

- [147] Feller, D. *J. Chem. Phys.* **1993**, *98*, 7059.
- [148] Partridge, H.; Schwenke, D. W. *J. Chem. Phys.* **1997**, *106*, 4618.
- [149] Wang, X.; Bowman, J. M. *J. Phys. Chem. A* **2014**, *118*, 684.
- [150] Wang, Y.; Bowman, J. M. *J. Chem. Phys.* **2013**, *139*, 154303.
- [151] Wang, Y.; Bowman, J. M. *J. Chem. Phys.* **2008**, *129*, 121103.
- [152] Mancini, J. S.; Bowman, J. M. *J. Chem. Phys.* **2013**, *138*, 121102.
- [153] Letzner, M.; Gruen, S.; Habig, D.; Hanke, K.; Endres, T.; Nieto, P.; Schwaab, G.; Walewski, L.; Wollenhaupt, M.; Forbert, H.; Marx, D.; Havenith, M. *J. Chem. Phys.* **2013**, *139*, 154304.
- [154] Hassanali, A. A.; Cuny, J.; Ceriotti, M.; Pickard, C. J.; Parrinello, M. *J. Am. Chem. Soc.* **2012**, *134*, 8557.
- [155] Kisiel, Z.; Lesarri, A.; Neill, J. L.; Muckle, M. T.; Pate, B. H. *Phys. Chem. Chem. Phys.* **2011**, *13*, 13912.
- [156] Andot, K.; Hynes, J. T. *J. Mol. Liq.* **1995**, *64*, 25.
- [157] Walewski, Ł.; Forbert, H.; Marx, D. *J. Chem. Phys.* **2014**, *140*, 144305.
- [158] Schröder, T.; Schinke, R.; Liu, S.; Bačić, Z.; Moskowitz, J. W. *J. Chem. Phys.* **1995**, *103*, 9228.
- [159] Liu, S.; Bačić, Z.; Moskowitz, J. W.; Schmidt, K. E. *J. Chem. Phys.* **1994**, *100*, 7166.
- [160] Huang, X.; McCoy, A. B.; Bowman, J. M.; Johnson, L. M.; Savage, C.; Dong, F.; Nesbitt, D. J. *Science* **2006**, *311*, 60.
- [161] Valdes, A.; Prosimiti, R. *Phys. Chem. Chem. Phys.* **2014**, *16*, 6217.
- [162] Xie, Z.; Braams, B. J.; Bowman, J. M. *J. Chem. Phys.* **2005**, *122*, 224307.
- [163] McCoy, A. B.; Huang, X.; Carter, S.; Bowman, J. M. *J. Chem. Phys.* **2005**, *123*, 064317.
- [164] Mancini, J. S.; Bowman, J. M. *J. Phys. Chem. A* **2014**,
- [165] Mancini, J. S.; Samanta, A. K.; Bowman, J. M.; Reisler, H. *J. Phys. Chem. A* **2014**,
- [166] Liu, H.; Wang, Y.; Bowman, J. M. *J. Am. Chem. Soc.* **2014**, *136*, 5888.
- [167] Liu, H.; Wang, Y.; Bowman, J. M. *J. Phys. Chem. Lett.* **2012**, *3*, 3671.

- [168] Steven G. Johnson, *The NLOpt Nonlinear-Optimization Package*, <http://ab-initio.mit.edu/nlopt>
- [169] Wang, Y.; Bowman, J. M. *J. Chem. Phys.* **2011**, *135*, 131101.
- [170] Mancini, J. S.; Bowman, J. M. *J. Phys. Chem. Lett.* **2014**, *5*, 2247.
- [171] Heberle, J.; Riesle, J.; Thiedemann, G.; Oesterhelt, D.; Dencher, N. A. *Nature* **1994**, *370*, 379.
- [172] Stowell, M. H. B.; McPhillips, T. M.; Rees, D. C.; Soltis, S. M.; Abresch, E.; Feher, G. *Science* **1997**, *276*, 812.
- [173] Borgis, D.; Hynes, J. T. *J. Phys. Chem.* **1996**, *100*, 1118.
- [174] Omta, A. W.; Kropman, M. F.; Woutersen, S.; Bakker, H. J. *Science* **2003**, *301*, 347.
- [175] Kreuer, K.-D. *Chem. Mater.* **1996**, *8*, 610.
- [176] Leopold, K. R. *Annu. Rev. Phys. Chem.* **2011**, *62*, 327.
- [177] Balci, F. M.; Uras-Aytemiz, N.; Gomez, P. C.; Escribano, R. *Phys. Chem. Chem. Phys.* **2011**, *13*, 18145.
- [178] Maity, D. K. *J. Phys. Chem. A* **2013**, *117*, 8660.
- [179] Temelso, B.; Morrell, T. E.; Shields, R. M.; Allodi, M. A.; Wood, E. K.; Kirschner, K. N.; Castonguay, T. C.; Archer, K. A.; Shields, G. C. *J. Phys. Chem. A* **2012**, *116*, 2209.
- [180] Krishnakumar, P.; Maity, D. K. *J. Phys. Chem. A* **2014**, *118*, 5443.
- [181] Mizuse, K.; Mikami, N.; Fujii, A. *Angew. Chem. Int. Ed.* **2010**, *49*, 10119.
- [182] Park, M.; Shin, I.; Singh, N. J.; Kim, K. S. *J. Phys. Chem. A* **2007**, *111*, 10692.
- [183] Lin, C.-K.; Wu, C.-C.; Wang, Y.-S.; Lee, Y. T.; Chang, H.-C.; KuoPresent address: School of Physi, J.-L.; Klein, M. L. *Phys. Chem. Chem. Phys.* **2005**, *7*, 938.
- [184] Okumura, M.; Yeh, L. I.; Myers, J. D.; Lee, Y. T. *J. Chem. Phys.* **1986**, *85*, 2328.
- [185] Douberly, G. E.; Walters, R. S.; Cui, J.; Jordan, K. D.; Duncan, M. A. *J. Phys. Chem. A* **2010**, *114*, 4570.
- [186] Headrick, J. M.; Diken, E. G.; Walters, R. S.; Hammer, N. I.; Christie, R. A.; Cui, J.; Myshakin, E. M.; Duncan, M. A.; Johnson, M. A.; Jordan, K. D. *Science* **2005**, *308*, 1765.

- [187] McCoy, A. B.; Guasco, T. L.; Leavitt, C. M.; Olesen, S. G.; Johnson, M. A. *Phys. Chem. Chem. Phys.* **2012**, *14*, 7205.
- [188] Cheng, T. C.; Bandyopadhyay, B.; Mosley, J. D.; Duncan, M. A. *J. Am. Chem. Soc.* **2012**, *134*, 13046.
- [189] Servage, K. A.; Silveira, J. A.; Fort, K. L.; Russell, D. H. *J. Phys. Chem. Lett.* **2014**, *5*, 1825.
- [190] Fournier, J. A.; Johnson, C. J.; Wolke, C. T.; Weddle, G. H.; Wolk, A. B.; Johnson, M. A. *Science* **2014**, *344*, 1009.
- [191] Lin, W.; Paesani, F. *J. Phys. Chem. A* **2013**, *117*, 7131.
- [192] Douberly, G. E.; Miller, R. E. *J. Phys. Chem. B* **2003**, *107*, 4500.
- [193] Brown, A.; McCoy, A. B.; Braams, B. J.; Jin, Z.; Bowman, J. M. *J. Chem. Phys.* **2004**, *121*, 4105.
- [194] Bende, A.; Suhai, S. *Int. J. Quant. Chem.* **2005**, *103*, 841.
- [195] Kamarchik, E.; Bowman, J. M. *J. Phys. Chem. Lett.* **2013**, *4*, 2964.